POLITECNICO DI TORINO

Collegio di Ingegneria Chimica e dei Materiali

Corso di Laurea Magistrale
in Ingegneria dei Materiali

Tesi di Laurea Magistrale

Characterization of powder and its bulk Ti-6Al-V samples produced by Electron Beam Melting process

Relatore

Prof. Sara Biamino

Correlatore

Dr. Abdollah Saboori

Candidato

Seyed Hamidreza Samar

Ottobre 2019

Index

Abbreviations	III
Riassunto della Tesi di Laurea Magistrale	V
1. Introduction	1
2. State of the art	3
2.1 History of titanium	3
2.2 Metallurgy of titanium and its alloys	3
2.2.1 Ti crystal structure and nature of anisotropy	4
2.2.2 β/α transformation	7
2.2.3 Diffusion	9
2.2.4 Effects of alloying elements on phase transformations	9
2.2.5 Classification of Ti alloys	10
2.3 Ti-6Al-4V alloy	12
2.3.1 Properties	12
2.3.2 Applications	14
2.3.3 Metallurgy	15
2.4 Solidification theory	16
2.4.1 Nucleation process	16
2.4.2 Grain growth process	20
2.4.3 Variables determining microstructure in the melt pool	23
2.5 Solid state phase transformations in titanium alloys	25
2.6 Additive manufacturing technologies (AM)	29
2.7 Applications of AM technologies	31
2.7.1 Aerospace and Automotive Industry	31
2.7.2 Architectural Industry	31
2.7.3 Artistic Industry	32
2.7.4 Medical Industry	32
2.8 AM technologies for metallic materials	32
2.8.1 Powder bed systems	33
2.8.2 Powder Feed Systems	33

2.8.3 Wire Feed Systems 34
2.9 Electron Beam Melting (EBM) 35
2.9.1 Equipment and conditions of work 35
2.9.2 Application of EBM 39
2.9.3 Advantages and disadvantages of the technique 39
3. Experimental activity: materials, equipment and methods 41
3.1 Definition of samples 41
3.2 Materials 41
3.3 EBM system 42
3.3.1 Software 42
3.3.2 Hardware 43
3.3.3 Powder recovery system (PRS) 44
3.4 Characterization methods 45
3.4.1 Powder characterization 45
3.4.1.1 Hall flowmeter (Flowability measurement) 45
3.4.1.2. Particle size distribution (PSD) by the sieve analysis (ASTM B214-07) 46
3.4.1.3 Morphology and Elemental analysis 46
3.4.1.4 Cross-Section 47
3.4.2 Bulk characterization 50
3.4.2.1 Metallography 50
3.4.2.2 Microscopy analysis of samples 51
3.4.2.2.1 Optical microscopy 51
3.4.2.2.1 Scanning Electron Microscopy (SEM) 52
3.5 X-ray diffractometer 52
4. Results and discussion 55
4.1 Powder monitoring 55
4.1.1 First cycle of the production process 55
4.1.2 Second cycle of production process 64
4.1.3 n cycle of the production process 72
4.2 Microstructural analysis of Ti-6Al-4V bars produced by EBM 81
5. Conclusions 99
6. References 101
Acknowledgements 105

Abbreviations

AM = Additive manufacturing

SLS = Selective laser sintering

SLM = Selective laser melting

EBM = Electron beam melting

SEM = Scanning electron microscopy

TEM = Transmission electron microscopy

HIP = Hot Isostatic Pressing

HRTEM = High resolution transmission electron microscopy

EBSD = Electron back scattered diffraction

EDP = Electron diffraction pattern

SS = Stainless steel

DSS = Duplex stainless steel

CP = Cross section polished

EDS = Energy dispersive X-ray spectroscopy

ODS = Oxide dispersion strengthened steel

PREP = Plasma Rotating Electrode Process

REP = Rotating Electrode Process

GSD = Granulation-Sintering-Deoxygenation

Riassunto della Tesi di Laurea Magistrale (Sessione Otobre 2019)

"Characterization of Ti-6Al-4V powder and its bulk samples produced by Electron Beam Melting process"

Candidato: Seyed Hamidreza Samar

Relatore: prof. Sara Biamino

Correlatore: Dott. Abdollah Saboori

I processi di additive manufacturing sono riconosciuti come tecniche recenti caratterizzate da un certo numero di vantaggi aventi l'obiettivo di migliorare e semplificare la sequenza di fabbricazione di componenti leggeri e con forme complicate, a costi competitivi e con un numero contenuto di difetti. Dunque, essi rappresentano delle interessanti alternative ai metodi di produzione adottati in settori particolarmente critici; ad esempio le tecnologie di additive manufacturing sono considerate estremamente promettenti in ambito aerospaziale. Inoltre, i processi di additive manufacturing, in generale, non necessitano di utensili da taglio e di stampi; di conseguenza, si possono ottenere un'ampia libertà di progettazione di componenti.

Le tecniche AM possono essere classificate in sei categorie principali:

1) Modellazione a Deposizione Fusa (FDM);
2) 3D Fiber Deposition (3DF);
3) Stampa 3D;
4) Stereolitografia (STL);
5) Sinterizzazione Selettiva a Laser (SLS);
6) Electron Beam Melting (EBM).

Le principali tecniche AM impiegate per i materiali metallici sono del tipo a letto di polvere (powder bed systems), ad alimentazione da polvere (powder feed systems) e ad alimentazione da filo (wire feed systems). Nel primo caso uno strato, o letto, di polvere viene distribuito tramite un apposito sistema e un programma comunicante con la macchina controlla il movimento della sorgente termica caratterizzato da sufficiente energia. Di conseguenza, la sorgente termica trasforma il letto di polvere nella forma desiderata. Successivamente, un altro strato viene deposto, distribuito e trasformato nella forma desiderata dalla sorgente termica. Queste operazioni vengono ripetute fino al completamento del componente. Invece, i sistemi ad alimentazione da polvere prevedono che la polvere viene trasferita attraverso un ugello sulla superficie di costruzione; un laser, comandato da un sistema di guida del fascio, viene applicato per fondere il singolo strato di polvere che viene successivamente trasformato nella forma progettata del componente. Queste operazioni vengono ripetute più volte per arrivare al componente tridimensionale finale. Infine, nel caso di sistemi ad alimentazione da filo, la materia prima di questi sistemi è appunto un materiale a forma di filo e la loro sorgente di energia termica può essere o il fascio di elettroni o il fascio laser o l'arco plasmatico. Le operazioni di questi sistemi iniziano con la deposizione del materiale sotto forma di perline e le successive passate sopra questi strati formano i componenti tridimensionali.

Tra le tecniche di additive manufacturing più interessanti è incluso il processo di Electron Beam Melting (EBM). Esso viene maggiormente impiegato in ambiti di applicazione

particolarmente critici, come quello aerospaziale e biomedico, per la fabbricazione di componenti metallici con forme complicate da riprodurre e aventi resistenza meccanica elevata. Il vantaggio principale della tecnologia EBM consiste nell'utilizzo di una camera in vuoto che consente di ridurre notevolmente il rischio di contaminazioni quando si lavorano metalli che reagiscono facilmente all'ambiente circostante, come il titanio e le sue leghe, e nella possibilità di preriscaldare molto le polveri di partenza. Queste sono le due caratteristiche che differenziano l'EBM dall'altra tecnologia di additive manufacturing sempre a letto di polvere che però sfrutta una sorgente laser per la fusione selettiva.

Le leghe di titanio sono caratterizzate dalla combinazione di densità relativamente bassa e di buone proprietà meccaniche. Pertanto, esse sono annoverate tra le leghe maggiormente utilizzate in ambito aerospaziale. La lega Ti-6Al-4V è del tipo $\alpha + \beta$, cioè a di sotto della temperatura di trasformazione allotropica titanio $\alpha \rightarrow$ titanio β (882°C nel titanio puro) le due fasi coesistono. Questa lega presenta bassa densità, buona resistenza meccanica e buona tenacità a frattura, eccellente resistenza alla corrosione e proprietà di biocompatibilità interessanti. Queste caratteristiche la rendono la lega di titanio più comunemente utilizzata. È stata inizialmente impiegata per la produzione di componenti aerospaziali negli anni 50 del secolo scorso, ad esempio motori a reazione e turbine a gas. Inoltre, essendo biocompatibile, le sue applicazioni sono state estese anche in ambito biomedico.

Durante lo svolgimento del lavoro qui descritto è stata condotta un'analisi su polveri di lega Ti-6Al-4V per ottenere informazioni sulla scorrevolezza, sulla distribuzione delle dimensioni delle particelle, sulla presenza o meno di elementi di contaminazione, sulla porosità residua in modo da valutare la qualità delle stesse polveri e come queste influenzino il processo di EBM per la realizzazione di provini massivi. Parallelamente valutare come si modificano queste proprietà riciclando le polveri per lavorazioni successive. I provini prodotti sono stati caratterizzati in termini di microstruttura (tipologia e morfologia delle fasi presenti, tipologia di grani presenti, presenza di difetti residui). L'osservazione è stata condotta su varie sezioni a diverse altezze e posizioni delle barre prodotte tramite processo EBM. Poiché la piattaforma di costruzione dei componenti prodotti tramite processo EBM è normalmente costituito d'acciaio, si è quantificata l'entità della diffusione di elementi di contaminazione, come il ferro, che potrebbero compromettere le proprietà del componente prodotto.

La polvere di lega Ti-6Al-4V analizzata è stata prodotta dalla compagnia Arcam AB con una distribuzione delle dimensioni delle particelle da 45 a 105 μm. La composizione chimica espressa in percentuale in peso è riportata in tabella I.

Tabella I. Composizione chimica della lega Ti-6Al-4V utilizzata negli esperimenti.

	ArcamTi6Al4V, Typical	**Ti6Al4V, Required standard***	**Ti6Al4V, Required standard****
Aluminium,Al	6%	5.5-6.75%	5.5-6.75%
Vanadium,V	4%	3.5-4.5%	3.5-4.5%
Carbon,C	0.03%	<0.1%	<0.08%
Iron,Fe	0.1%	<0.3%	<0.3%
Oxygen,O	0.15%	<0.2%	<0.2%
Nitrogen,N	0.01%	<0.05%	<0.05%
Hydrogen,H	0.003%	<0.015%	<0.015%
Titanium,Ti	Balance	Balance	Balance

*ASTMF1108 (cast material) **ASTMF1472 (wrought material)

Prima di introdurre le polveri di Ti-6Al-4V nella macchina EBM e produrre, di conseguenza, i campioni massivi, esse sono state sottoposte a test di scorrevolezza e, successivamente, è stata determinata la distribuzione delle loro dimensioni. Il test di scorrevolezza è stato eseguito col test di scorrimento Hall secondo lo standard ASTM B21317. 50 g di polvere sono versate in un contenitore ad imbuto avente un orifizio situato nella sua parte inferiore; la scorrevolezza di tipi diversi di polveri viene valutata in base al loro tempo di fuoriuscita. Invece, la distribuzione delle dimensioni delle polveri è stata ricavata attraverso la procedura descritta nello standard ASTM B214-07, il quale prevede l'uso di una serie di setacci con apertura delle maglie di dimensione decrescente man mano che ci si sposta dalla parte superiore alla parte inferiore dello strumento. In questo modo, lo strumento si scuote e le polveri caratterizzate da una granulometria maggiore dell'apertura del setaccio rimangono intrappolate su di esso, mentre quelle caratterizzate da una granulometria minore dell'apertura del setaccio scenderanno nei setacci inferiori. I setacci, inizialmente pesati senza polveri, vengono pesati con il materiale residuo.

Una volta effettuate queste analisi preliminari sulle polveri vergini, esse sono state successivamente introdotte nella macchina EBM per la produzione di barre. Una volta preparato il modello CAD del componente desiderato, il file corrispondente viene elaborato dal computer che si interfaccia con la macchina EBM e suddivide idealmente il disegno in diversi strati sottili che saranno riprodotti nel componente finale. Un catodo a filamento, raggiunta una certa temperatura, emette elettroni che vengono accelerati dal sistema catodo-anodo. Il fascio così prodotto viene convogliato verso la camera di costruzione tramite un insieme di lenti magnetiche. La camera di costruzione viene mantenuta a un livello di vuoto tale da limitare fenomeni di scattering tra elettroni e l'aria intrappolata residua. Una determinata quantità del materiale di partenza, inizialmente introdotto in due tramogge, viene scaricato sulla piattaforma di costruzione e appiattita successivamente con un sistema di distribuzione. Tale quantità costituisce il primo strato di materiale da lavorare. Prima della

fusione vera e propria, lo strato di polvere distribuito sul piatto di costruzione viene sottoposto a uno stadio di preriscaldamento che permette di mantenere la camera a una temperatura sufficientemente alta e provoca una sinterizzazione iniziale leggera del materiale. Nella fase vera e propria di fusione, il fascio di elettroni interagisce col materiale su punti prestabiliti dello strato di polvere precedentemente riscaldata. Il fascio di elettroni è caratterizzato da un'energia sufficientemente elevata e porta a fusione localizzata nei punti in cui è avvenuta l'interazione con lo stesso fascio. La piattaforma di costruzione si abbassa e inizia un nuovo ciclo, applicando un nuovo strato di polvere sopra a quello precedentemente trattato che viene anch'esso preriscaldato e fuso in maniera localizzata. Alla fine del processo produttivo, il componente finale si trova immerso in polvere parzialmente sinterizzata dal preriscaldamento, detta cake, che viene rimossa dal componente, recuperata e riutilizzata in processi di produzione successivi tramite il sistema di recupero delle polveri (PRS). La rimozione del cake è effettuata per mezzo di un getto di aria compressa, successivamente le polveri vengono setacciate e in questo modo recuperate.

In questo lavoro sono stati analizzati i seguenti materiali:

- le polveri nuove;
- le polveri derivanti dal cake che si dividono in: polveri prelevate da sopra e da sotto il piatto di costruzione (in questo lavoro sono denominate rispettivamente "top sintered powders" e "bottom sintered powders");
- le polveri che sono state recuperate dopo il processo di PRS effettuato dopo il primo, il secondo e il terzo ciclo di lavorazione EBM;
- i provini massivi costruiti nel primo, secondo e terzo ciclo di lavorazione.

Sia sulle polveri che sui provini massivi sono state ottenute immagini al microscopio ottico (MO) e al microscopio a scansione elettronica (SEM). Per valutare la porosità interna sia delle polveri che dei componenti massivi si è proceduto con l'inglobamento dei campioni in resina e lucidatura a specchio; per il raggiungimento di questo scopo non è stato necessario attaccare metallograficamente i materiali. Invece, l'attacco metallografico (con reagente Kroll) è stato effettuato per evidenziare la microstruttura osservabile nelle sezioni trasversali delle polveri e dei provini. Il SEM è stato utilizzato anche su polveri non inglobate per cercare di rilevare eventuali irregolarità superficiali, come la presenza di elementi di contaminazione, e per valutare la presenza o meno di satelliti. Impiegando la Energy Dispersive Spectroscopy (EDS accoppiata al SEM, è stata analizzata la composizione chimica di ogni fase microstrutturale (fase α e fase β) e la profondità di diffusione all'interno dei componenti massivi degli elementi di contaminazione provenienti dal piatto di costruzione (come ad esempio il ferro). La stessa tecnica EDS è stata inoltre adottata anche per le polveri non inglobate per ottenere la composizione chimica di alcune irregolarità presenti sulla loro superficie.

La tecnica di diffrazione ai raggi X (XRD) è stata utilizzata per avere informazioni sulla struttura cristallina delle fasi presenti nelle polveri (fase α o fase β).

In figura I si riportano i valori di scorrevolezza e di granulometria delle polveri vergini e di quelle prelevate dal PRS dopo il primo ciclo di lavorazione EBM. L'aumento di scorrevolezza (che si può notare dalla diminuzione del tempo di scorrimento da circa 24 s a circa 21 s per 50 g di polvere) dopo il primo ciclo di lavorazione EBM è dovuto all'eliminazione delle polveri più fini e alla riduzione della quantità di satelliti.

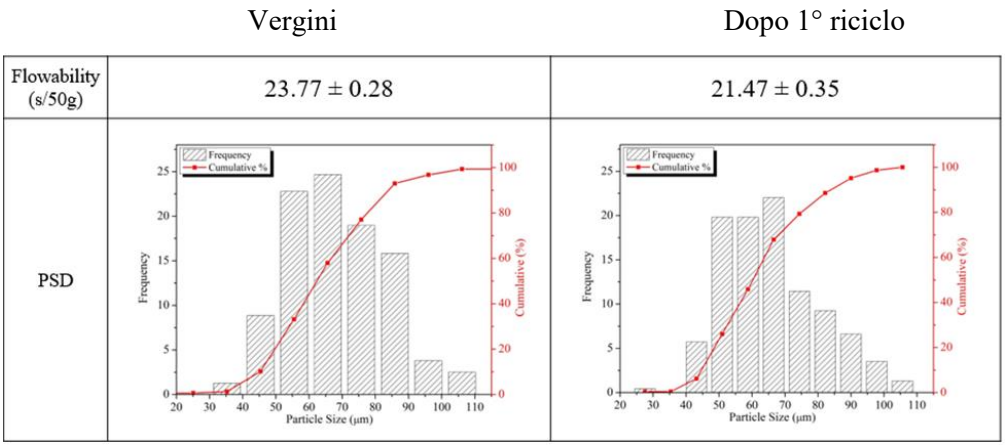

Figura I: Confronto tra la scorrevolezza e la distribuzione granulometrica delle polveri vergini e delle polveri prelevate PRS dopo il primo ciclo di lavorazione di EBM.

In figura II si riportano i valori di scorrevolezza e distribuzione granulometrica delle polveri prelevate dal PRS dopo il secondo ciclo di lavorazione EBM e dopo l'n-esimo ciclo di lavorazione EBM; Il tempo di scorrimento dopo il secondo riciclo è aumentato e, di conseguenza, è diminuita la scorrevolezza. Il numero delle particelle più fini è diminuito e le particelle rimaste hanno assunto una forma più irregolare, probabilmente perché, durante il processo di PRS, alcuni colli di sinterizzazione che si sono formati durante il preriscaldamento nel ciclo di lavorazione EBM si sono rotti. Infine, dopo il riciclo eseguito dopo l'n-esimo ciclo di lavorazione EBM il tempo di scorrimento è aumentato ulteriormente (da 24,87 ± 0,7 s/50 g di polvere a 25,78 ± 1,23 s/50 g di polvere); infatti, nonostante si è continuato a registrare un aumento delle particelle più grossolane, le polveri hanno subito un cambiamento di forma che è diventata più irregolare. La dimensione media delle polveri è passata dall'essere inizialmente di 62 μm nel caso delle polveri vergini a 70 μm nel caso delle polveri prelevate dopo l'n-esimo riciclo.

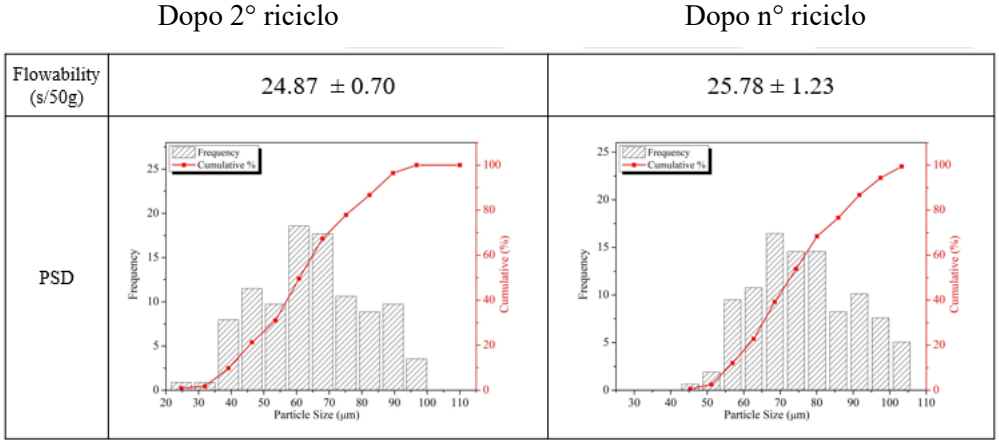

Figura II: Confronto tra la scorrevolezza e la distribuzione granulometrica delle polveri prelevate dopo il PRS eseguito dopo il secondo e l'n-esimo ciclo di lavorazione di EBM.

A titolo di esempio, si riportano da figura III-a a figura III-d immagini ottenute al microscopio ottico delle polveri di Ti-6Al-4V vergini, “top sintered”, “bottom sintered” e dopo il processo di PRS eseguito dopo il primo ciclo di lavorazione EBM. Le immagini nella prima riga si riferiscono a polveri non attaccate metallograficamente con il reagente di Kroll, poiché sono state acquisite per osservare la porosità presente in alcune particelle; quelle nella seconda riga, invece, sono state attaccate metallograficamente col reagente di Kroll al fine di esaminare la microstruttura. Come si vede dalle immagini nella prima riga, i pori visibili presentano tutti una forma pressoché sferica; da ciò si deduce che tali pori hanno origine dal processo di produzione delle polveri mediante “gas atomization”, cioè parte del gas pressurizzato utilizzato per ridurre il fuso metallico in numerose particelle microscopiche è rimasto intrappolato mentre si verificava il processo di solidificazione. Andando avanti con i cicli di EBM e con i processi seguenti di PRS tale porosità non sembra essere influenzata. Per quanto riguarda la microstruttura, invece, dalle immagini nella seconda riga delle figure III-a-d si può notare che solo nelle polveri vergini si rileva la presenza della struttura α’ martensitica aghiforme circondata dalla preesistente fase β. Tale struttura martensitica α’ si è trasformata nella fase α lamellare durante il ciclo di lavorazione EBM. I primi grani di fase α si nucleano e crescono in corrispondenza dei bordi di grano della fase β preesistente; invece, le lamelle di fase α si dispongono o a colonie (con lo stesso orientamento) o secondo la struttura Widmanstätten basket-weave (un gruppo di lamelle con lo stesso orientamento si incrociano con un altro gruppo avente orientamento diverso) all’interno dei grani della fase β preesistente. Nel secondo e nel terzo ciclo EBM e nei processi PRS seguenti le fasi α e β diventano più grossolane a causa dei ripetuti cicli di riscaldamento oltre la temperatura di trasformazione $\alpha \rightarrow \beta$ e successivo raffreddamento a cui sono sottoposte le polveri di Ti-6Al-4V.

Le immagini al SEM riportate da figura III-a a figura III-d si riferiscono a polveri di Ti-6Al-4V vergini, “top sintered”, “bottom sintered” e prelevate dopo il processo di PRS eseguito dopo il primo ciclo di lavorazione EBM, attaccate metallograficamente col reagente di Kroll.. Nelle immagini della quarta riga si individua la presenza di un alone visibile al SEM con una tonalità più scura di grigio (indicata con una freccia rossa in figura III-b_4) che circonda le particelle sottoposte al ciclo di lavorazione EBM e al processo PRS seguente. Probabilmente, questo strato di ossido si è iniziato a formare sulle polveri di Ti-6Al-4V a seguito dell’apertura della camera interna alla macchina EBM una volta terminato il processo ma con le polveri ancora relativamente calde e non viene rimosso nemmeno se sottoposto al processo PRS. Solo intorno alle polveri vergini non si riesce ad individuare uno strato di ossido. Nel secondo ciclo di lavorazione EBM lo strato di ossido diventa più spesso e, a partire dal terzo ciclo di lavorazione EBM, circonda completamente e in maniera uniforme la maggior parte delle particelle di Ti-6Al-4V.

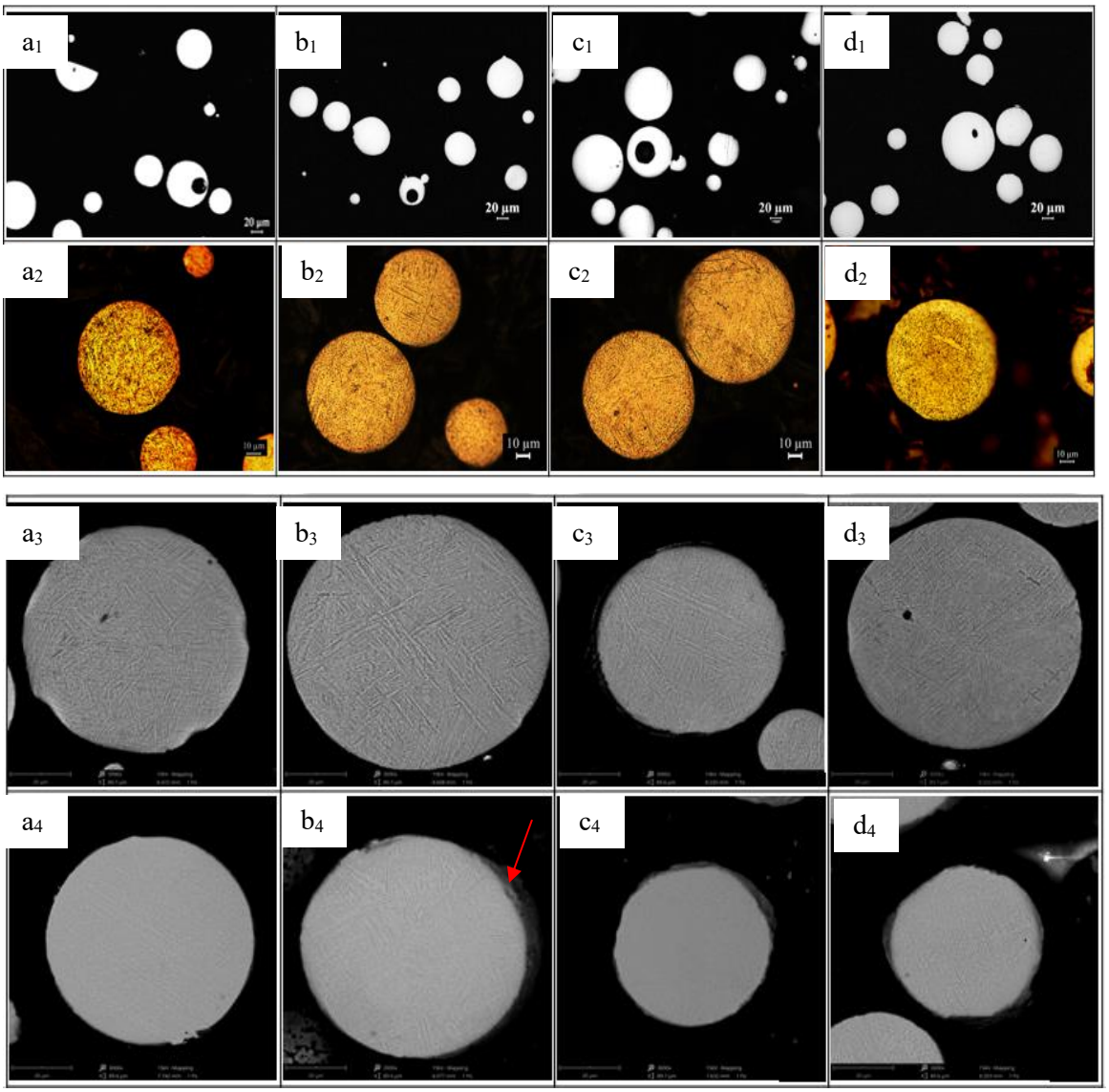

Figura III: Immagini al microscopio ottico e al SEM di (a) polveri di Ti-6Al-4V vergini, (b) "top sintered", (c) "bottom sintered" e (d) dopo il processo di PRS eseguito dopo il primo ciclo di lavorazione EBM. 1, 2, 3 e 4 si riferiscono, rispettivamente, alle sezioni trasversali osservate al microscopio ottico senza attacco metallografico, alla microstruttura osservata al microscopio ottico, alla microstruttura osservata al SEM e alle sezioni trasversali osservate al SEM per rilevare lo strato di ossido

In figura IV-a si riportano i risultati relativi alla diffrattometria ai raggi X effettuata su polveri di Ti-6Al-4V vergini, dopo il primo ciclo di lavorazione EBM prelevandole dal cake e prelevandole dopo il PRS. In figura IV-b si riportano le dimensioni dei cristalliti. Tali valori si ottengono prendendo in considerazione il picco principale della fase α in ciascun diffrattogramma ($2\theta \approx 40°$) e utilizzando la formula di Scherrer di seguito riportata:

$$\tau = \frac{K\lambda}{\beta \cos\theta} \qquad \text{(I)}$$

in cui τ corrisponde alla dimensione media dei cristalliti, K è un fattore di forma approssimabile all'unità (il valore più usato è 0,9), λ è la lunghezza d'onda del fascio di raggi X incidenti sul campione, β è la larghezza a metà altezza (FWHM), θ è l'angolo di Bragg. Dopo il primo ciclo di lavorazione EBM il picco principale è diventato più alto e stretto rispetto a quello relativo alle polveri vergini. Infine, si osserva una leggera diminuzione delle dimensioni medie dei cristalliti di α nelle polveri prelevate dopo il processo PRS eseguito dopo il primo ciclo di lavorazione EBM, in ogni caso sono sempre maggiori di quelli delle polveri vergini. Bisogna notare il fatto che in ogni diffrattogramma i picchi sono tutti associati alla fase α; ciò non significa che la fase β non esiste, ma è presente con dimensioni talmente piccole che corrisponderebbero a picchi non rilevabili dallo strumento e risultano assimilati al rumore di fondo. α' nelle polveri vergini dovrebbe presentare dei cristalli di dimensioni minori e, quindi, anche in questo caso i picchi non risultano distinguibili dal rumore di fondo.

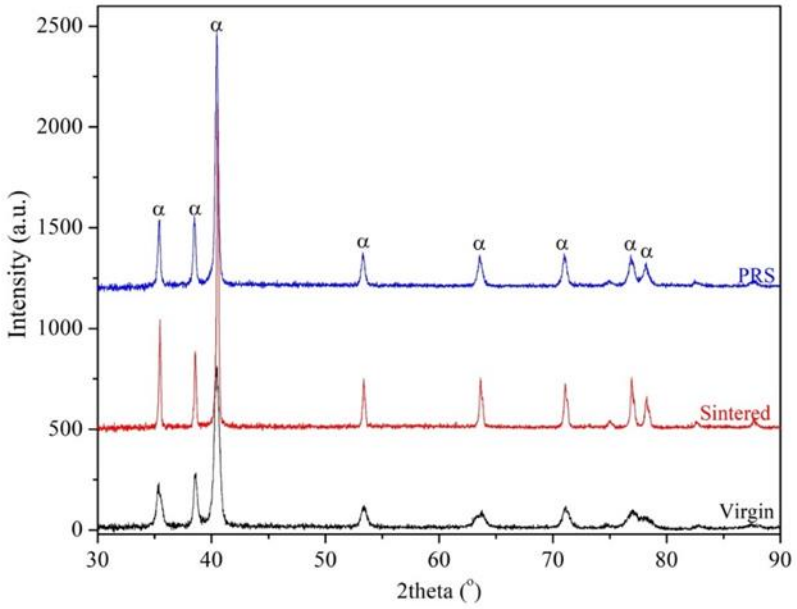

(a)

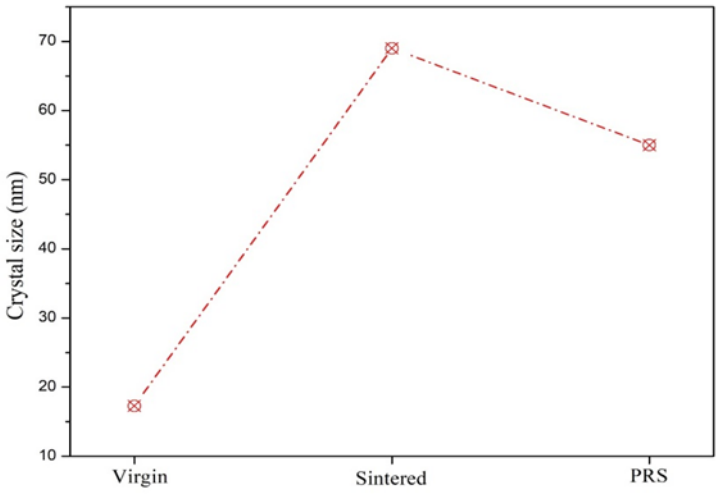

(b)

Figura IV: (a) Risultati di diffrattometria a raggi X (XRD) eseguita su polveri di Ti-6Al-4V vergini, sottoposte al primo ciclo di lavorazione EBM prelevate dal cake e prelevate dal processo PRS eseguito dopo il primo ciclo di lavorazione EBM e (b) conseguente diagramma relativo alle dimensioni medie dei cristalliti di α.

In figura V si riportano immagini al SEM di particelle di Ti-6Al-4V prelevate dal PRS dopo il primo ciclo di lavorazione EBM. Sulle superfici di due particelle diverse sono state effettuate delle analisi chimiche mediante la tecnica SEM-EDS. Su di esse non è stata rilevata solamente la presenza di titanio, alluminio e vanadio come ci si aspetterebbe, ma sono state trovate anche delle zone particolarmente ricche di ferro. Questo elemento viene classificato come impurezza, poiché normalmente nella composizione tipica della lega Ti-6Al-4V esso dovrebbe essere presente fino a un tenore massimo di 0,3% in peso. Probabilmente alcune "metallizzazioni" sono cadute dall'involucro di costruzione (building envelope), cioè l'insieme degli schermi che delimitano la camera di costruzione. In questo modo le polveri recuperate mediante PRS possono risultare essere contaminate dal ferro.

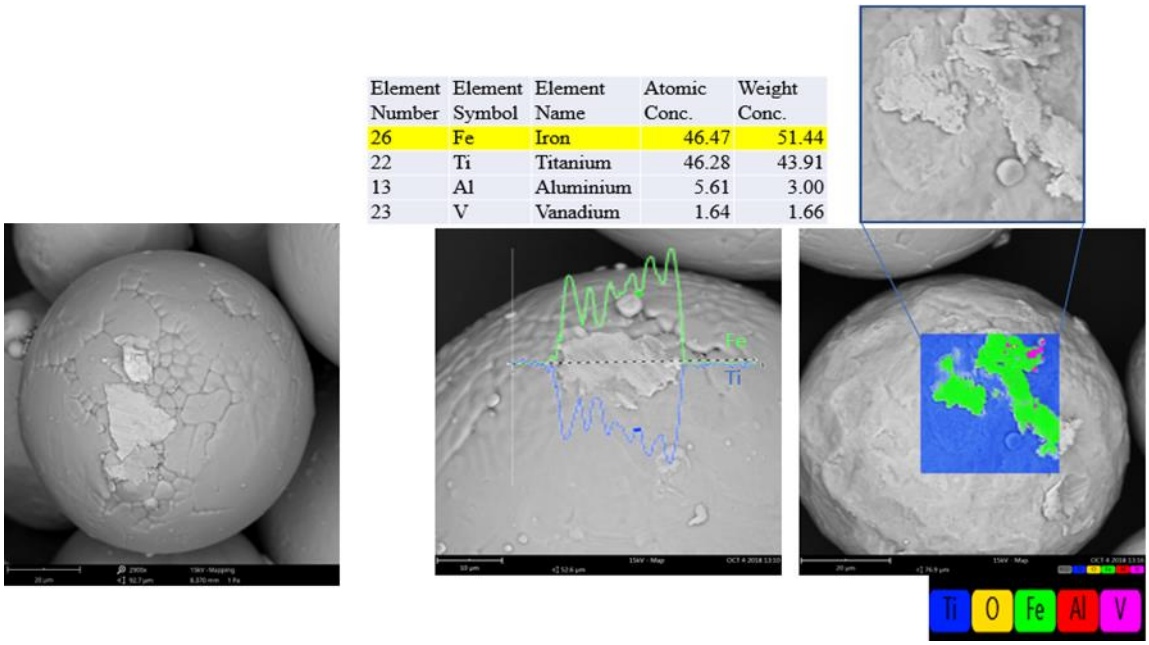

Figura V: Immagini al SEM delle particelle di Ti-6Al-4V prelevate dopo il processo PRS eseguito dopo il primo ciclo di lavorazione EBM contenenti alcune impurezze di ferro sulla superficie. Inoltre, viene illustrata la modalità con cui è stata effettuata l'analisi chimica mediante la tecnica SEM-EDS.

Inoltre, si riporta in figura VI un'analisi chimica mediante tecnica SEM-EDS effettuata su particelle di Ti-6Al-4V prelevate dal processo PRS eseguito dopo il terzo ciclo di lavorazione EBM. Queste particelle sono legate tra di loro mediante "colli di giunzione" che si sono formate durante il ciclo di lavorazione EBM. Si può notare come la le contaminazioni con ferro vadano a contribuire alla formazione dei "colli di giunzione". Probabilmente tali particelle, inizialmente separate, erano presenti nella zona preriscaldata e si sono "saldate" mediante le impurezze di ferro presenti in quel momento.

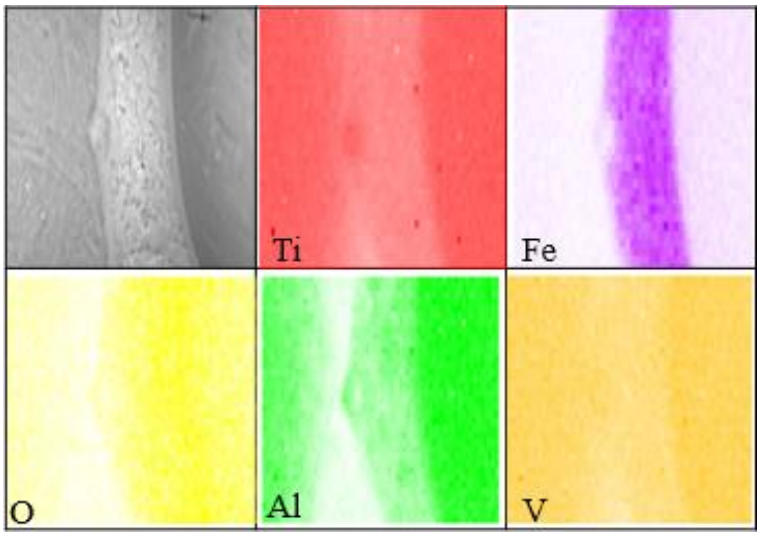

(a)

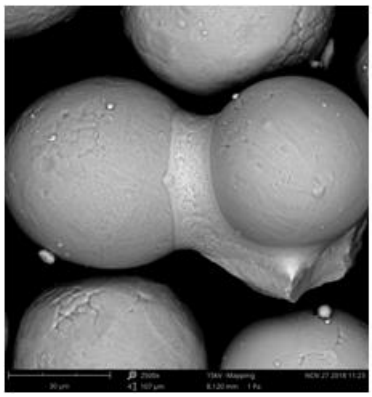

(b)

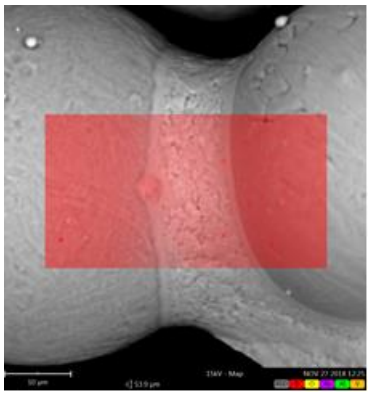

(c)

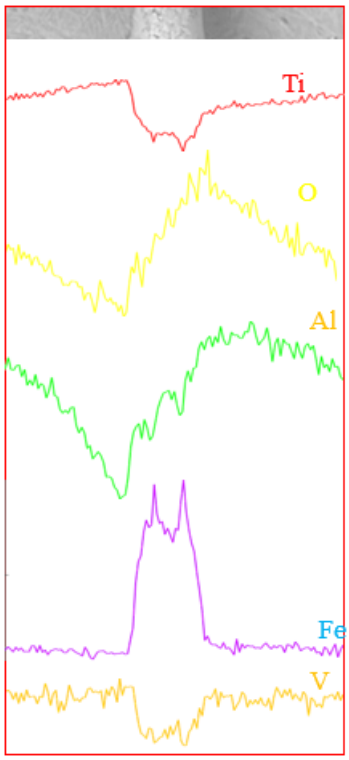

(d)

Figura VI: (a) Analisi chimica mediante tecnica SEM-EDS di un collo di sinterizzazione che si è formato tra due particelle di Ti-6Al-4V prelevate dopo il processo PRS eseguito dopo il terzo ciclo di lavorazione EBM. (b) Immagine al SEM di particelle di Ti-6Al-4V prelevate dopo il processo PRS eseguito dopo il terzo ciclo di lavorazione EBM, con (c) l'indicazione dell'area di riferimento per l'analisi di composizione chimica EDS. (d) Andamento delle composizioni chimiche degli elementi ossigeno, titanio, alluminio, ferro e vanadio lungo la direzione radiale della stessa particella.

Per quanto riguarda la caratterizzazione bulk, sono state prodotte mediante EBM quattro barre cilindriche posizionate sul piatto di costruzione nella maniera indicata in figura VII-c. In figura VII-a si riportano, per ognuno dei quattro campioni, alcune immagini acquisite in vari punti col microscopio ottico. Tali immagini sono state ottenute senza attaccare metallograficamente i campioni, poiché in questo caso si è voluto esaminare la porosità.

Mediante tecniche di analisi d'immagine utilizzando il software integrato al microscopio ottico si sono discriminate le aree appartenenti ai pori (zone nere) rispetto a quelle appartenenti al metallo "denso" (zone chiare). Per mezzo del software utilizzato è stato calcolato il rapporto tra l'area totale appartenente ai pori e l'area totale dell'immagine, ricavando in questo modo la porosità. I risultati sono stati riportati, sotto forma di media aritmetica ± deviazione standard, nella tabella in figura VII-b. Si può osservare come le quattro barre prodotte in posizioni diverse sulla piattaforma di costruzione presentano porosità medie confrontabili.

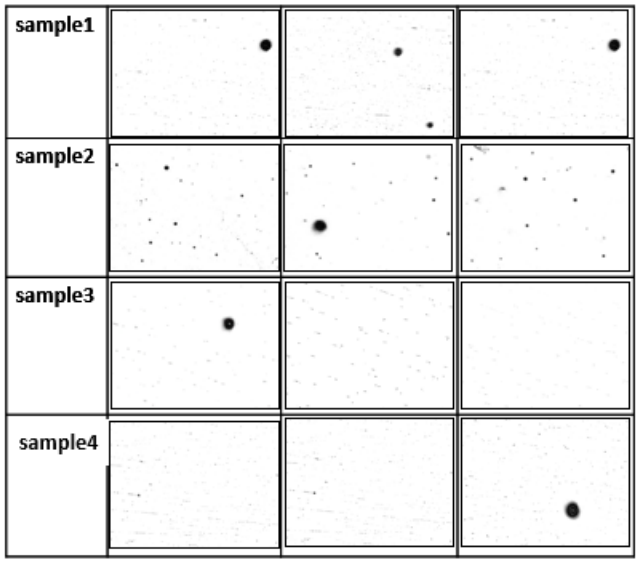

(a)

	Average porosity ± standard deviation (%)
Sample 1	0.55 ± 0.46
Sample 2	0.51 ± 0.57
Sample 3	0.74 ± 0.30
Sample 4	0.44 ± 0.23
Overall	0.56 ± 0.13

(b)

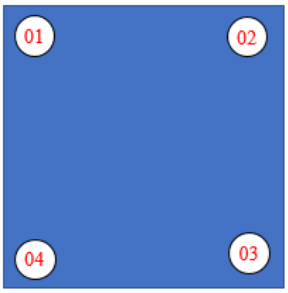

(c)

Figura VII: (a) Immagini al microscopio ottico riguardanti la distribuzione dei pori all'interno di quattro barre prodotte mediante tecnica EBM. (b) Risultati delle misure di porosità. (c) Disposizione delle quattro barre sulla piattaforma di costruzione.

In figura VIII si riportano immagini al microscopio ottico di una delle quattro barre cilindriche (20 mm di diametro e 60 mm di altezza) prodotte mediante EBM, acquisite da diverse posizioni e a diverse altezze (chiamate in questo lavoro "top", "middle" e "near bottom"). Anche in questo caso i valori di porosità sono stati ricavati mediante le stesse tecniche di analisi di immagine. Dalle immagini si possono individuare sia pori di forma pressoché sferica, dovuti a intrappolamento della fase gas già precedentemente intrappolato nelle particelle di polvere, che pori indotti dal processo EBM, di forma più irregolare; questi ultimi, nella maggior parte dei casi, sono causati da una "mancanza" di fusione in alcuni punti dello strato in fase di lavorazione che non si congiungono bene con lo strato deposto successivamente e sono dette "lacks of fusion".

I "lacks of fusion" si concentrano il particolare nella zona bottom. Le zone middle e top si attestano su livelli di porosità inferiore e sono pressoché prive di "lacks of fusion".

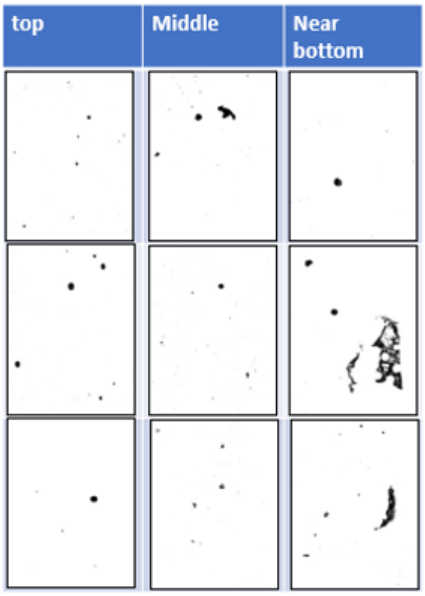

(a)

	Average porosity ± standard deviation (%)
Near Bottom	0.68 ± 0.42
Middle	0.27 ± 0.17
Top	0.27 ± 0.18
Overall	0.41 ± 0.24

(b)

Figura VIII: (a) Immagini al microscopio ottico delle parti "top", "middle" e "near bottom" di una delle barre cilindriche di Ti-6Al-4V prodotte mediante EBM, acquisite al fine di valutarne la porosità. (b) Risultati dei valori medi delle porosità ottenuti nelle tre regioni.

Oltre a barre di forma cilindrica, sono state prodotte due barre di Ti-6Al-4V di forma a parallelepipedo sempre mediante tecnica EBM. Le due barre, aventi altezza differente, in questo lavoro sono chiamate “long bar” e “short bar”. In figura IX si riportano immagini al microscopio ottico di diverse parti a cinque altezze differenti del “long bar” e di diverse parti a tre altezze differenti dello “short bar”. Anche in questi casi non è stato necessario procedere con l’attacco metallografico. I risultati delle porosità ad altezze differenti sono riportate nelle rispettive tabelle in forma di valore medio ± deviazione standard.

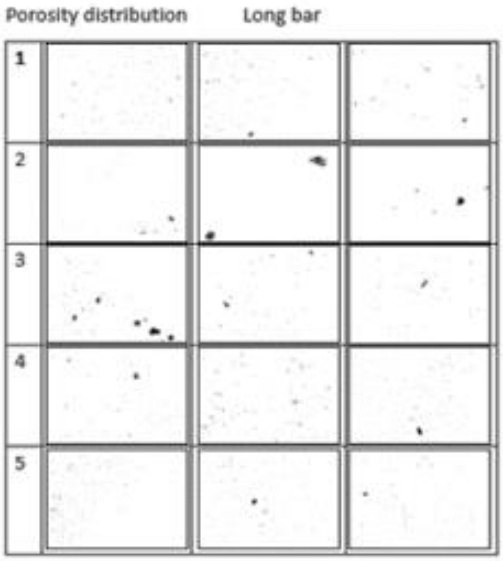

	Average porosity ± standard deviation (%)
Row 1	0.18 ± 0.50
Row 2	0.14 ± 0.17
Row 3	0.10 ± 0.30
Row 4	0.10 ± 0.09
Row 5	0.02 ± 0.03
Overall	0.11 ± 0.06

Long bar

(a)

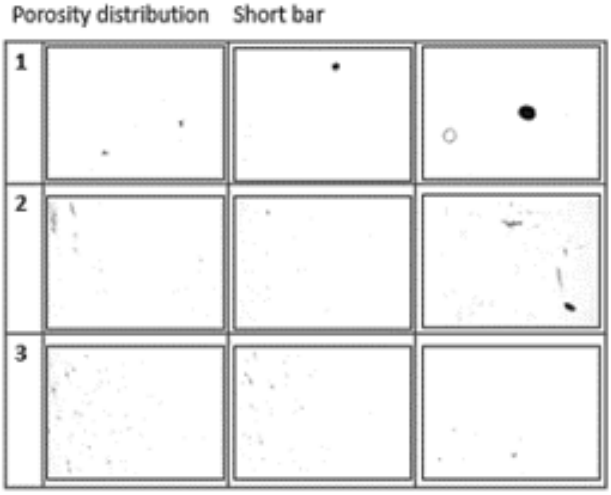

	Average porosity ± standard deviation (%)
Row 1	0.14 ± 0.31
Row 2	0.045 ± 0.10
Row 3	0.004 ± 0.00
Overall	0.06 ± 0.07

Short bar

(b)

Figura IX: (a) Immagini al microscopio ottico di tre zone differenti a cinque altezze diverse del "long bar" ottenute per finalità di valutazione della porosità e risultati relativi riportati in tabella. (b) Immagini al microscopio ottico di tre zone differenti a tre altezze diverse dello "short bar" ottenute per finalità di valutazione della porosità e risultati relativi riportati in tabella.

Si riportano in figura X delle immagini al microscopio ottico riguardanti la microstruttura osservata a diverse altezze di una delle quattro barre cilindriche di Ti-6Al-4V, sezionata longitudinalmente, con diametro 10 mm e altezza 15 mm. Per evidenziare la microstruttura, il provino è stato attaccato metallograficamente col reagente di Kroll. Dalle immagini si nota in alcune zone la presenza di colonie di fase α e, in altre zone, di fase α con struttura Widmanstätten basket-weave. Le zone vicine all'estremità superiore della barra presentavano una struttura più fine rispetto alle zone centrali..

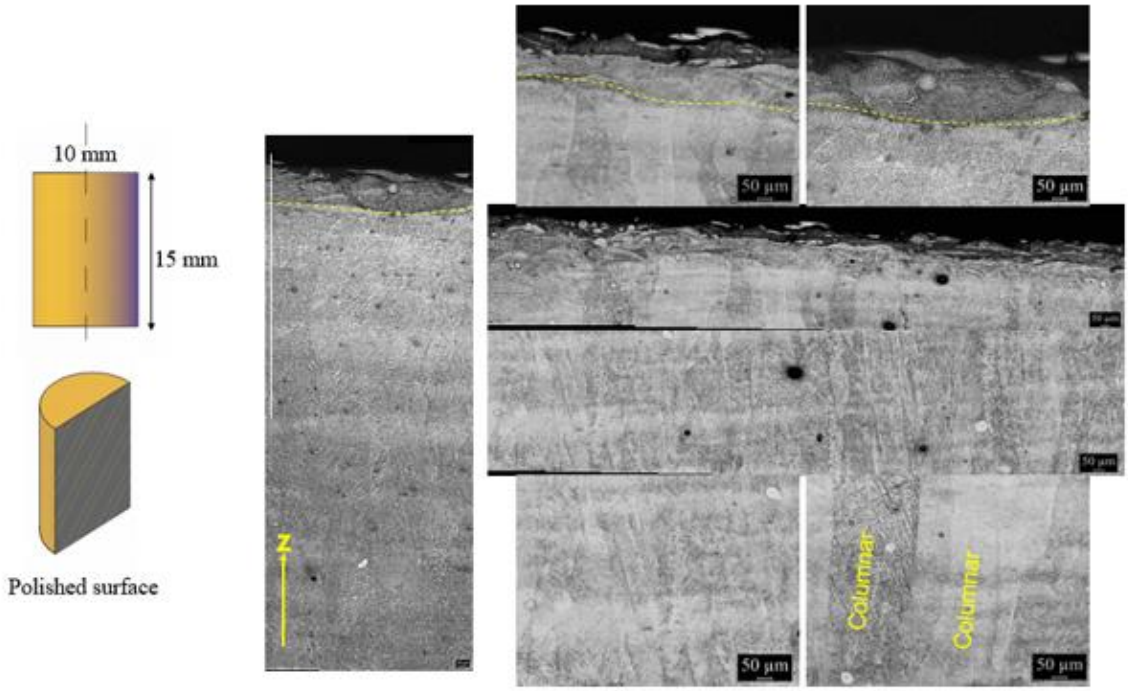

(a) (b)

Figura X: (a) Dimensioni delle quattro barre cilindriche di Ti-6Al-4V prodotte mediante EBM con indicazione del piano di sezione. (b) Immagini al microscopio ottico di una delle quattro barre cilindriche.

In conseguenza delle possibili differenze di velocità di raffreddamento parte della fase β bcc si trasforma nelle diverse morfologie α: struttura martensitica di tipo α' o α'' con morfologia a pacchetti o a lamelle in base alla trasformazione non diffusiva che sta avvenendo, α_m (massivo) o α' a seconda delle trasformazioni competitive diffusionali e non diffusionali, coesistenza della fase α allotriomorfa, che si genera ai bordi di grano della fase β preesistente, con la struttura α o a colonie o di tipo Widmanstätten a seconda che la velocità di raffreddamento sia più o meno elevata, coinvolgendo ad ogni modo trasformazioni di tipo diffusivo in entrambe le situazioni. Pertanto, si riportano in figura XI delle immagini al microscopio ottico e al SEM riguardanti la microstruttura osservata in diversi punti (parte sinistra, centrale e destra) di una sezione trasversale all'incirca a metà altezza della barra cilindrica di Ti-6Al-4V precedente. Anche in questo caso il campione è stato attaccato metallograficamente col reagente di Kroll per evidenziarne la microstruttura.

Considerando che il processo EBM è caratterizzato da relativamente basse velocità di raffreddamento, perché l'involucro di costruzione (building envelope) viene mantenuto normalmente a temperature di 650-700°C, la microstruttura che si ottiene nelle barre di Ti-6Al-4V deriva da trasformazioni diffusive. Dunque, nelle figure X e XI si osserva la struttura α a colonie o di tipo Widmanstätten all'interno dei grani della fase β preesistente. Invece, non si rileva nessuna struttura α' nelle immagini poiché durante gli stadi di preriscaldamento e

fusione che avvengono durante la fusione selettiva di ogni strato di polvere la struttura martensitica α' inizialmente presente nelle polveri vergini si trasforma in α. Le fasi α e β localizzate nelle parti in alto dei campioni presentano dimensioni diverse da quelle localizzate nella parte centrale e nelle parti inferiori; gli strati più in alto presentano grani più piccoli perché non subiscono più l'effetto di un ulteriore ciclo di riscaldamento e raffreddamento che provoca la crescita dei grani. In figura XIII si nota anche come lo spessore delle lamelle di fase α al centro della sezione è maggiore di quello che si osserva nella parte sinistra e destra, probabilmente a causa dell'effetto del bordo che si raffredda più velocemente del centro. La microstruttura così descritta si ottiene allo stesso modo sia nelle barre di Ti-6Al-4V cilindriche che nella "long bar" e "short bar" a forma di parallelepipedo e presenta gli stessi andamenti ad altezze differenti.

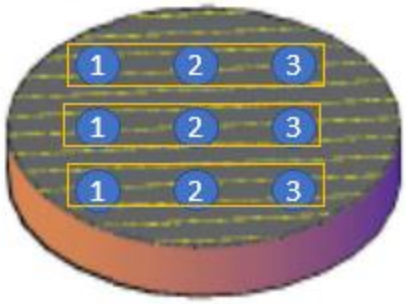

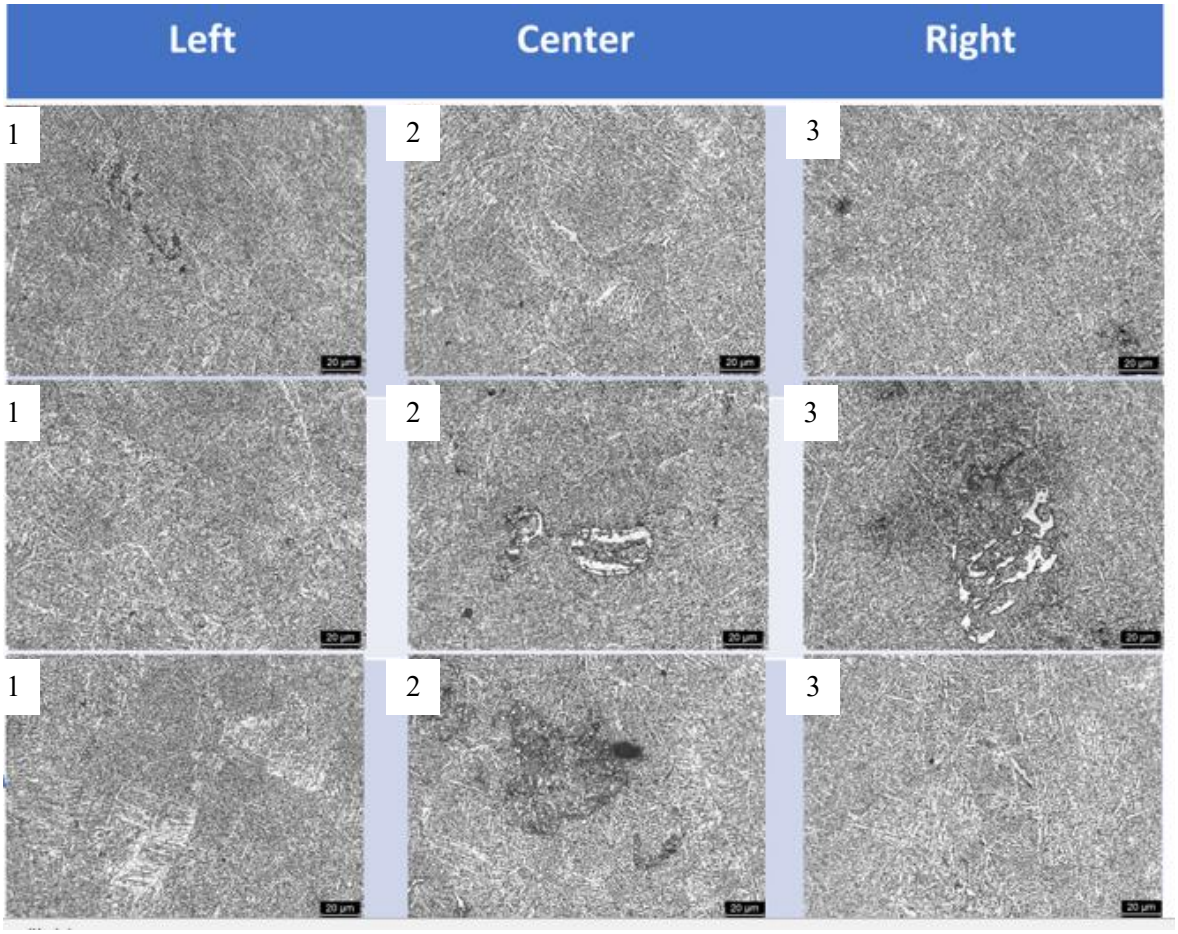

(a)

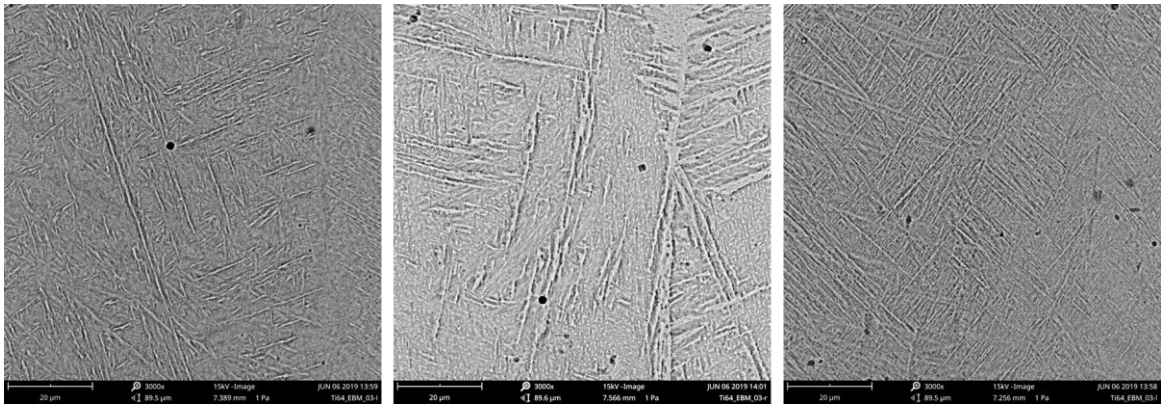

(b)

Figura XI: (a) Immagini al microscopio ottico acquisite in tre posizioni diverse della parte sinistra, centrale e destra di una regione posizionata circa a metà altezza di una delle quattro barre cilindriche di Ti-6Al-4V prodotte mediante EBM. (b) Immagini al SEM ottenute rispettivamente nella parte sinistra, centrale e destra di una delle quattro barre prodotte mediante EBM.

La figura XII-a rappresenta la mappa di composizione chimica, ottenuta mediante analisi SEM-EDS, ricavata all'interfaccia tra il piatto di costruzione e il componente realizzato mediante EBM. In figura XII-b, invece, vengono riportati i profili di composizione degli elementi ferro, cromo, nichel e vanadio. Attraverso le informazioni che provengono dalle immagini si può affermare che la diffusione del ferro, del nichel e del cromo dal piatto di costruzione all'interno del campione di Ti-6Al-4V raggiunge una profondità minore di 200 μm.

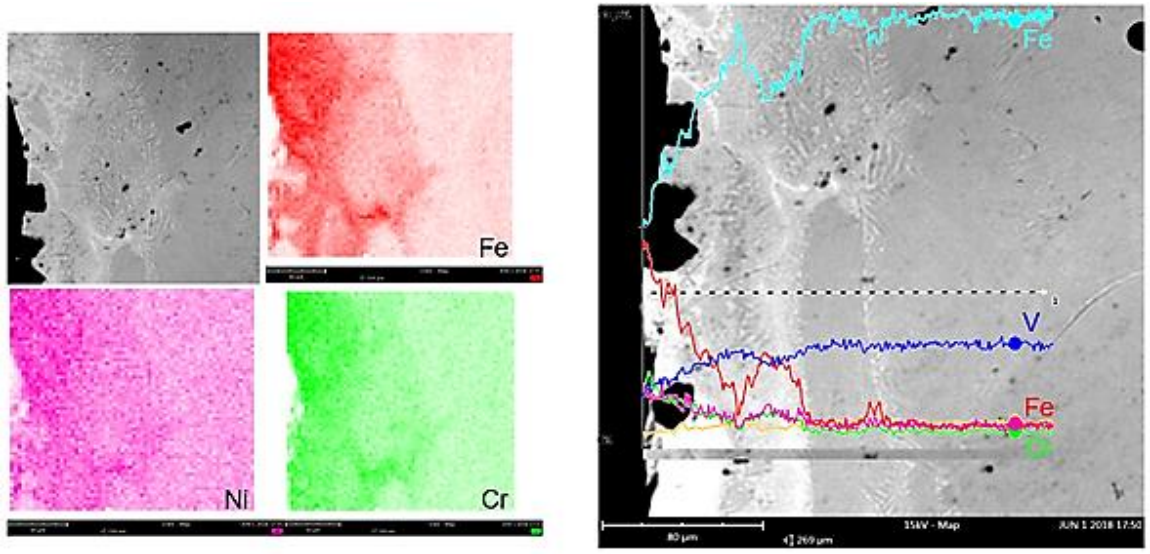

(a) (b)

Figura XII: (a) Mappa di composizione chimica ottenuta mediante SEM-EDS in corrispondenza della superficie del campione a contatto col piatto di costruzione. (b) Analisi SEM-EDS di composizione chimica eseguita sulla linea tracciata.

Secondo i risultati di questa tesi, le conclusioni principali possono essere tratte come segue:

- Dopo il primo ciclo di lavorazione EBM, la scorrevolezza delle polveri è aumentata rispetto alle polveri vergini, principalmente a causa della riduzione del numero di satelliti, e quindi è diminuita a partire dal secondo ciclo di produzione di EBM, poiché le polveri sono diventate meno arrotondate;
- Aumentando i cicli di lavorazione EBM, la dimensione media delle particelle è variata da 62 μm nel caso delle polveri vergini a 70 μm nel caso delle polveri riciclate dopo l'n-esimo ciclo di lavorazione EBM. Infatti, le polveri più grossolane tendono ad aumentare e il volume delle particelle fini diminuisce principalmente sia a causa dei fenomeni di sinterizzazione che si verificano nello stadio di preriscaldamento durante il processo EBM sia nella fase di recupero;
- L'analisi della porosità interna delle particelle di Ti-6Al-4V sottoposte al processo di produzione EBM ha messo in evidenza il fatto che la porosità delle polveri durante questo processo non è cambiata e che tali pori sono ottenuti dalla produzione di polveri Ti-6Al-4V mediante processo di gas atomization;

- Si è anche scoperto che, dopo il primo ciclo di lavorazione EBM, si è formato uno strato di ossido spesso e non uniforme e quindi, aumentando il numero dei cicli di lavorazione EBM, è diventato gradualmente più spesso e più uniforme e copre l'intera superficie delle particelle;
- La microstruttura delle polveri era caratterizzata principalmente da una microstruttura a colonie o Widmanstätten basket-weave. Le microstrutture iniziali delle polveri erano caratterizzate da α ’martensite che si è formata durante il processo di gas atomization, che è un processo di solidificazione rapido. Mentre, anche dopo il primo ciclo di lavorazione EBM, la microstruttura delle polveri ha iniziato a trasformarsi nella microstruttura α + β più stabile e, successivamente, aumentando il numero di cicli di lavorazione EBM, la fase α è diventata gradualmente più spessa;
- I picchi rivelati dall’XRD si riferiscono tutti alla fase α e le dimensioni medie dei cristalli di quella fase sono aumentate con il processo di sinterizzazioneLa fase β non è stata rilevata dallo strumento sebbene la sua presenza sia dimostrata dalle analisi SEM-EDS;
- La contaminazione da ferro è stata rivelata su alcune particelle, probabilmente a causa della caduta di alcune metallizzazioni nell'involucro di costruzione (building envelope) durante il processo di costruzione;
- Nelle barre prodotte da EBM si trovano due tipi di pori: porosità indotta da gas e porosità indotta dal processo EBM. L'ultimo è visibile come una mancanza di fusione in alcuni punti. Il valore medio delle porosità misurate risulta essere intorno a 0,29%, comunque un valore molto basso;
- La valutazione della porosità dei campioni compatti prodotti mediante EBM in diverse posizioni sulla piastra di partenza ha mostrato che il contenuto di porosità di questi campioni è uguale e indipendente dalla posizione del campione;
- L'analisi SEM-EDS ha mostrato che la profondità di diffusione degli elementi di lega dalla piastra di partenza, che è una piastra di acciaio inossidabile, all'interno delle barre prodotte da EBM era inferiore a 200 μm. Ciò significa che i principali elementi di lega, che sono Fe, Cr, Ni, sono stati diffusi nei campioni Ti-6Al-4V e la profondità di diffusione è inferiore a 200 μm;
- I materiali compatti erano caratterizzati principalmente da una microstruttura a colonie o Widmanstätten basket-weave e, con la tecnica SEM-EDS, è possibile distinguere la fase α, ricca di alluminio, dalla fase β, ricca di vanadio. I grani β vicino alla piastra di partenza nucleano e crescono in modo quasi equiassiale. Negli strati superiori, invece, i grani crescono in modo colonnare, seguendo il gradiente termico sviluppato lungo la direzione longitudinale dei campioni. I grani α iniziali nucleano preferibilmente ai bordi di grano della fase β precedentemente formata e, successivamente, la fase α si diffonde e cresce anche all'interno dei grani β con una microstruttura a colonie o Widmanstätten basket-weave, a seconda delle velocità di raffreddamento;
- Si è anche scoperto che, poiché il processo EBM è caratterizzato da basse velocità di raffreddamento, poiché l'involucro di costruzione viene normalmente mantenuto a 650-700 ° C, la microstruttura ottenuta in Ti-6Al-4V deriva da trasformazioni controllate da diffusione. Di conseguenza, non è stato possibile rivelare la fase α’ perché, durante il preriscaldamento e la fusione che si verificano dopo la fusione selettiva di ogni strato, questa struttura martensitica si trasforma in α + β;

- Nei campioni compatti, le posizioni vicino al lato esterno sono generalmente caratterizzate da larghezze inferiori di grani α e β rispetto alle posizioni interne poiché localmente aumentavano le velocità di raffreddamento.

1. Introduction

Materials processing consists of different types of processes applied by industrial manufacturing to convert the extracted raw materials (generally from mineral materials for the case of metals) into semi-products or final shapes by different chemical ways.

In recent years, the additive manufacturing processes have been known as young production methods with different advantages, that improve and simplify manufacturing operations and produce light and complex-shape components with low prices and small number of defects according to clients' requirements. They may represent an interesting alternative way to produce components in very critical sectors such as aeronautics, for the production of turbine blades. These methods also shows their characteristic independence from using tools such as dies, moulds and machining. Thus, they represent flexible design processes with decreased manufacturing times compared to other methods and offer an excellent efficiency of 3D printing and rapid prototyping.

The electron beam melting process (EBM) has been known as one of the most important production processes in particularly sensible fields ,such as biomedical and aerospace, to produce metallic parts with high strength and complex geometries. The main reason for the success of EBM consists in the production of metals sensitive to reactive environments, such as titanium and its alloys, and in the possibility of these metals to be offered in form of powders. The last one determined the emergence of this method among other additive manufacturing techniques.

The Ti-6Al-4V alloy, also known as Ti64, is an $\alpha + \beta$ titanium alloy with high strength, low density, high fracture toughness, excellent corrosion resistance and interesting biocompatibility properties. In fact, this alloy is also known as the most popular among titanium alloys in about half of material markets. At first, it found application in the aerospace sector for sensible components of aeroplane structure in the 1950s. In fact, this light and strong alloy can save the weight in structures bearing high loads and is therefore suitable for jet engines, gas turbines and many airframe components. Furthermore, because of the high biocompatibility with human body, it has been conceived for many applications in biomedical fields.

The purpose of the work described here aims to monitor the powder quality such as flowability, particle size distribution, contamination, etc. in three different cycles to have a clear idea to explain some unknown defects such as Fe rich regions and gas porosity in the bulk samples. Moreover, the microstructural evolution of Ti-6Al-4V is analysed in detail through the microstructure analysis of as-built Ti-6Al-4V bars in the building direction at different heights and perpendicular to the building direction. Since the start plate is normally a steel plate and Ti alloys produced by EBM needs a grade of purity to be used in the biomedical applications, the depth of diffusion of elements from the start plate into the Ti-6Al-4V is also analysed and quantified.

2. State of the art

2.1 History of titanium

Titanium is the ninth most abundant element and fourth large in number structural metal in the Earth's crust next to aluminium, iron, and magnesium [1]. It is naturally found in the form of ilmenite ($FeTiO_3$) and rutile (TiO_2), and it has a high affinity towards oxygen. Gregor was the first person that discovered this element as an unknown species in dark magnetic iron sand (ilmenite) in 1791. After that, in 1795, Klaproth, a German chemist, for the first time analysed rutile and determined it as an oxide of an unknown element that he named it as titanium after Titans, "the powerful sons of the earth", from the Greek mythology. Many attempts were frequently made to isolate the metal from oxygen and nitrogen, but producing ductile and pure titanium was difficult. During 1937-1940, the first commercial process by Kroll in Luxembourg reduced titanium tetrachloride with magnesium in an inert gas atmosphere and the resulting titanium is named "titanium sponge" because of its porous and spongy aspect [2].

In the 18^{th}-century industries began their research on titanium alloys but it didn't have important results until the middle of the 20^{th} century for the development of gas turbine engines. After that, aeronautic sectors have developed into big titanium users with both applications in engines and airframe structures [1].

At the same time, the aerospace industry found problems related to enhance operating temperatures and to complete application of polymer-based composites in eventually, including metal matrix composites and titanium aluminides, provide new ways for future growth. Moreover, recovery in extractive metallurgy and processing methods has made titanium-based alloys more available in different industries. In 1984, the DuPont Company was the first one to produce titanium commercially [3], [4].

Today aerospace sector is still the prime consumer of titanium and titanium alloys, but other markets like architecture, chemical processing, medicine, power generation, marine and offshore, sports and hobbies, and transportation have achieved developed admissions [1].

The highly favourable combination of properties which include high corrosion resistance, significant strength to weight ratios, effective resistance to fatigue, has caused to a considerable range of application but with high costs of extraction and processing that limited their performance [2].

2.2 Metallurgy of titanium and its alloys

Titanium alloys interest from industrial fields, such as aerospace, biomedical and chemical ones is due to the contemporary satisfaction of excellent properties and high temperature resistance with respect to other light alloys [2].

2.2.1 Ti crystal structure and nature of anisotropy

Titanium doesn't keep the same structure during temperature changes below melting. Like many other metals (e.g. Fe, Co, Zr, Ca, Ce), it undergoes *allotropic* transformations, i.e. those characterized by complete transformation of a crystalline phase into another one. The crystal structure of pure titanium is Hexagonal Close Packed (HCP) until 882 ± 2°C, the so-called *transus temperature*; at higher temperature, it becomes Body Centred Cubic (BCC) until melting occurs at 1670°C. The HCP structure (with lattice parameters a = 0.295 nm and c = 0.468 nm) is also denoted as α phase, while the BCC structure (with lattice parameter a = 0.332 nm at 900°C) is also denoted as β phase. The close packed planes of the HCP crystal structure (figure 2.1.a) are distinguished in the following way: basal plane (0002), prismatic planes (one of the three (1010) planes) and the prismatic planes (one of the six (1011) planes). a_1, a_2 and a_3, with indices <1120>, are defined as close packed directions. For the BCC unit cell, one of the six close packed planes (110) and two of the close packed directions <111> are represented in figure 2.1.b [1], [2].

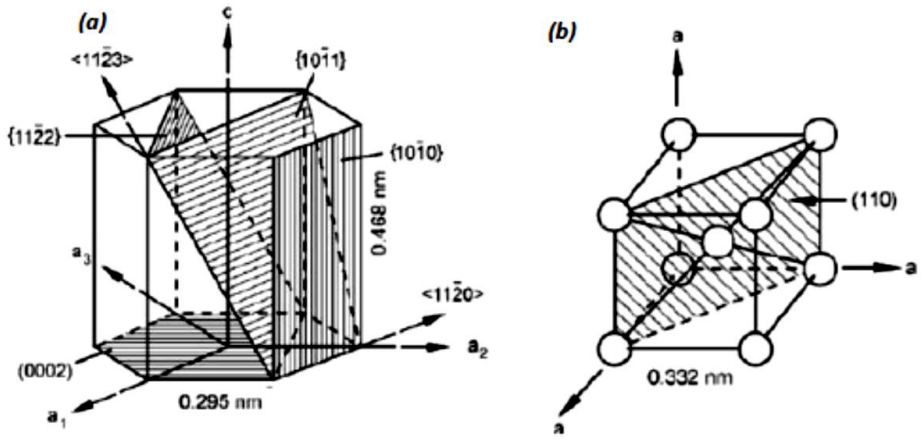

Figure 2.1: The unit cells for the (a) α and (b) β phases in titanium [2].

Hexagonal structure exhibits a considerable anisotropic behaviour that influence the variation of elastic properties evaluated on different directions of loading or deformations. For example, figure 2.2 reports on chart the Young's modulus values (E) of a single crystal of pure α titanium obtained on different load application directions (indicated as γ, the angle between the c-axis and the stress axis). The Young's modulus diminishes from 145 GPa, when it is measured in parallel with the c-axis, to 100 GPa, when it is measured normally to the c-axis. Similar behaviours are observed for the shear modulus. Anyway, anisotropic effects are less evident in polycrystalline α-titanium with weak crystallographic texture, as the degree of anisotropy depends by the level of texture; a stronger texture brings about a more anisotropic behaviour of the material [2]. The bcc crystal structure is characterized by a more isotropic behaviour with respect to hcp; thus, plastic deformations and diffusion rates are differently influenced by the presence of one or the other crystalline phase.

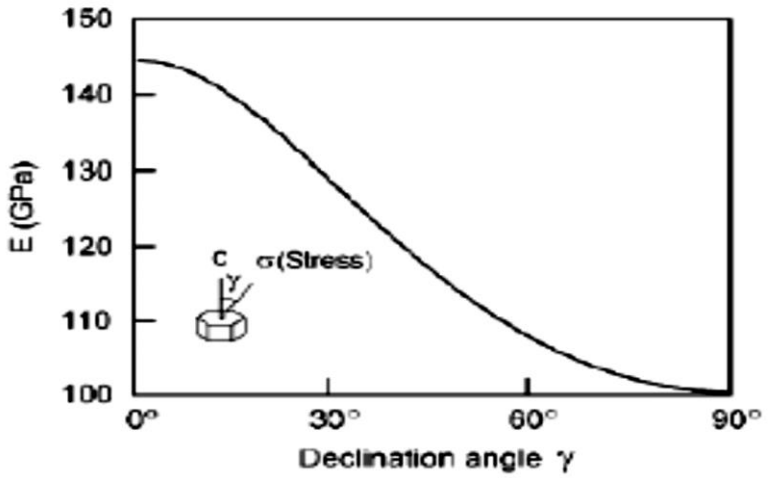

Figure 2.2: Young's modulus (E) of a single α titanium crystal as a function of loading direction [2].

Table 2.1 lists some physical properties related to a polycrystalline α titanium with a high level of purity.

Table 2.1. Physical properties of high-purity polycrystalline α titanium (> 99.9%) at 25°C [1].

Structure prototype	Mg
Pearson symbol	hP2
Space group	$P6_3/mmc$ (194)
β-transus temperature	882 °C
Lattice parameters	a=0.295 nm
	c=0.468 nm
	c/a=1.587
Thermal expansion coefficient [$10^{-6}K^{-1}$]	8.36
Thermal conductivity [W/mK]	14.99
Specific heat capacity [J/kgK]	523
Electrical resistance [10^{-9} Ωm]	564.9
Elastic modulus [GPa]	115
Shear modulus [GPa]	44
Poisson's ratio	0.33

Titanium is classified among the lightest metallic materials, as its density (4.51 $g \cdot cm^{-3}$) is about half of iron and nickel ones, as reported in figure 2.3.

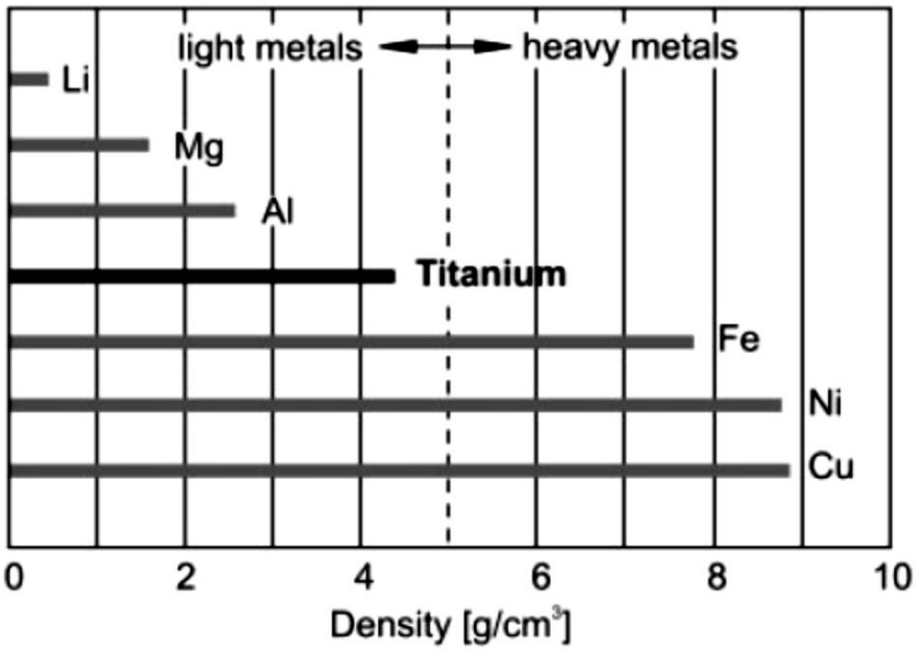

Figure 2.3: Density of selected metals [1].

Table 2.2 reports some characteristics of the crystal structures most encountered in metals.

Table 2.2. Characteristic parameters of the three important types of metallic structures [1].

Structure type	*N*	*CN*	*P*	*Slip planes* / *Slip directions*		*Slip system per unit cell*	*Atom density of slip plane*	b_{min}/a
				indices	*numbers*			
hcp (c/a=1,633)	6	12	74%	{0001}	1	1×3=3	≈ 91%	1
				$\langle 11\bar{2}0 \rangle$	3			
bcc	2	8	68%	{110}	6	6×2=12	≈ 83%	$1/2\sqrt{3}$
				⟨111⟩	2			≈ 0,87
fcc	4	12	74%	{111}	4	4×3=12	≈ 91%	$1/2\sqrt{2}$
				⟨110⟩	3			≈ 0,71

N	Number of atoms per unit cell
CN	Coordination number
P	Packing density
b_{min}/a	Minimal slip component

As the strain capability until failure of any metal depends essentially by the number of slip planes per unit cell, hcp structure is characterized by less deformability than bcc and fcc. Consequently, the hcp α phase in titanium alloys is less ductile than bcc β one. Along with the

number of slip systems, which is proportional to the probability of dislocations to glide, the atomic density of slip planes constitutes another factor influencing the deformation of the different crystalline phases. According to this reasoning, hcp should be more deformable than bcc, but the energy of plastic deformation depends also by the minimum slip length (b_{min}). For hcp crystals, this value corresponds to the lattice parameter a, while b_{min} corresponds to $0.87 \cdot a$ in case of bcc metals. Therefore, bcc metals generally require less strain energy for plastic deformation than hcp ones. By taking a = 0.295 nm and c = 0.468 nm as the lattice parameters of the α titanium, c/a = 1.587, which is less than the ideal value 1.633. With reduction of c/a ratio, the prism planes become denser than the basal ones; both prism and basal planes have got three slip systems and just two of them are independent of each other. So, there are four independent slip systems in total. Pyramidal planes can't increase the number of slip systems, as the glide occurring on such planes is divided in two components (gliding on prism and basal planes). Thus the glide on pyramidal planes is not independent. According to von Mises' criterion, homogeneous plastic deformation is achieved with the presence of five independent slip systems at least. Consequently, the hcp α phase of titanium is hardly deformed. The limited observed ductility of this crystalline phase arises from the activation of secondary slip planes and the possible occurrence of mechanical twinning. Figure 2.4 shows the active slip systems of the hcp α titanium [1].

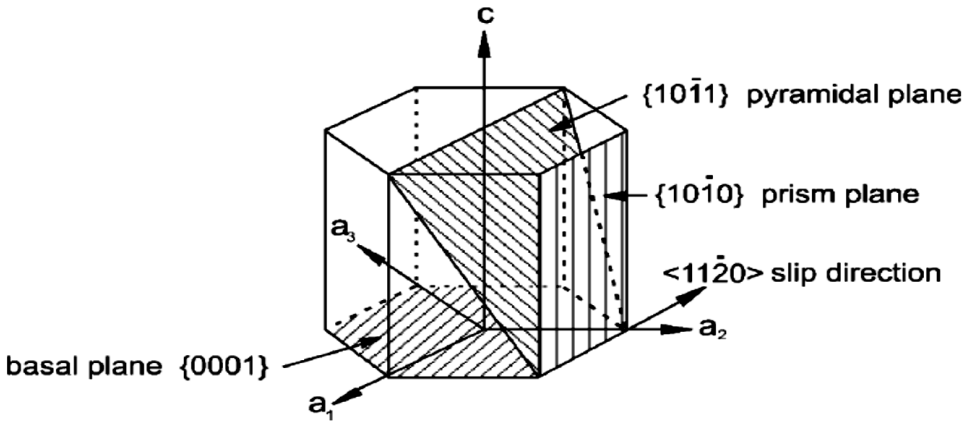

Figure 2.4: Schematic representation of slip systems of hexagonal crystal lattices [1].

2.2.2 β/α transformation

In titanium, the basal planes {0001} of the hexagonal α phase were formed by cooling the β phase regions; the most densely packed planes of the bcc β phase {110} are converted into the basal planes of the β phase. The larger distance between the basal planes in hexagonal α phase with respect to the distance between the planes {110} in β phase (table 2.2) provides a small atomic distortion during β/α transition (figure 2.5). This causes a small contraction of the c-axis with respect to the a-axis in the α phase of hcp hexagonal titanium crystal, which causes a reduction of the c/a ratio compared to the c/a ratio obtained in an ideally packed hexagonal titanium structure. A microscopic reduction of volume during cooling process is observed after the β/α transformation [1].

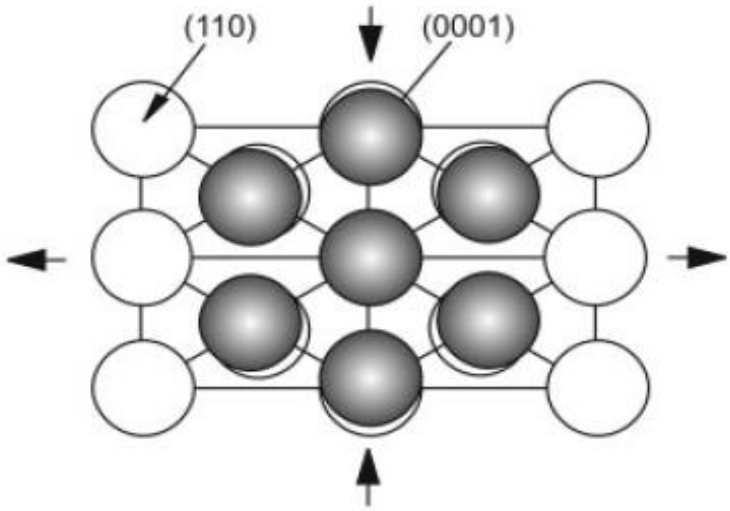

Figure 2.5: β/α transformation according to Burgers relationship [1].

The following relationship between different orientations of planes and directions shows the transformation of the slip plane of the bcc β titanium into the basal plane of the hcp α titanium and the slip directions of orientation:

$\{0001\}_\alpha$ // $\{110\}_\beta$

$<1120>_\alpha$ // $<111>_\beta$

Slip directions and slip planes can be described by Burger vector and this can be used to describe also the above orientation relationship. A maximum of 12 different orientations of the α phase originates from six slip planes and two slip directions of β titanium. The individual α lamellar packets can grow inside the prior β grains from the boundaries of the same grains in one of the 12 possible related orientations (the previously described Burger's relationship), so that they are similarly oriented within one β grain. Other lamellar packets may grow in one of the 12 possible orientations within those previously developed and can form the basket-weave structure that is shown in figure 2.6 [1].

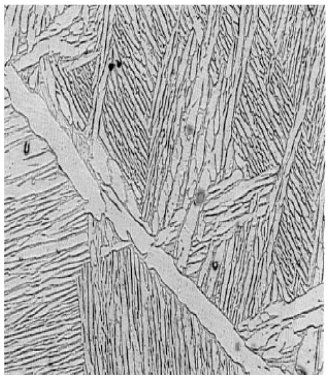

Figure 2.6: Lamellar microstructure of Ti-6Al-4V alloy (basket weave structure) [1].

2.2.3 Diffusion

The significantly slower diffusion happening inside hcp α titanium with respect to that occurring in bcc β phase, because of the high density of packed atoms in α structure compared to that in the bcc β titanium, causes a big influence on some of their properties, such as creep performances, hot workability and super-plasticity. High creep performances of α titanium derives from its small volume diffusion; this determines that α titanium has noticeable creep performances with respect to the β titanium alloy. Diffusion processes depending on time and temperature will be slower under the transus temperature. According to different rates of cooling, different sizes of lamellar structure could be obtained, so that a high rate of cooling forms very fine lamellar structure instead a slow cooling rate causes a coarse lamellar structure. The α lamellar structure can spread radially, namely parallel to the {110} planes of the β phases in titanium alloys. Thus, if the cooling rate for nucleation of the grains is sufficient, the lamellar structures begin to grow both at the grain boundaries and at the front of individual lamellar pockets. Also, the metastable fine platelets or acicular formations could be obtained as martensitic structures through a diffusionless mechanism with a cooling above the martensitic start temperature and this process causes that the bcc β phase completely converts into the hcp α phase. The result of the martensitic formation causes a more strengthened structure without embrittlement with respect to that happening in the normal α titanium. The hexagonal α' martensite and orthorhombic α''martensite are two different structures of the martensitic structure which can be formed. The last one originates by quenching from a temperature under about 900°C, with good final deformability properties. Instead, the hexagonal α' martensite phase has some orientation relationships with β phase as hcp α phase has. The non-diffusional nucleation process of martensite structure provides the formation of a very fine basket-weave structure with needle like structure [1].

2.2.4 Effects of alloying elements on phase transformations

The presence of alloying elements provokes the shift upward or downward of the α ↔ β transus temperature, that is 882°C in case of pure titanium. Figure 2.7 shows the classification of the alloying elements according to their effects on transition temperatures.

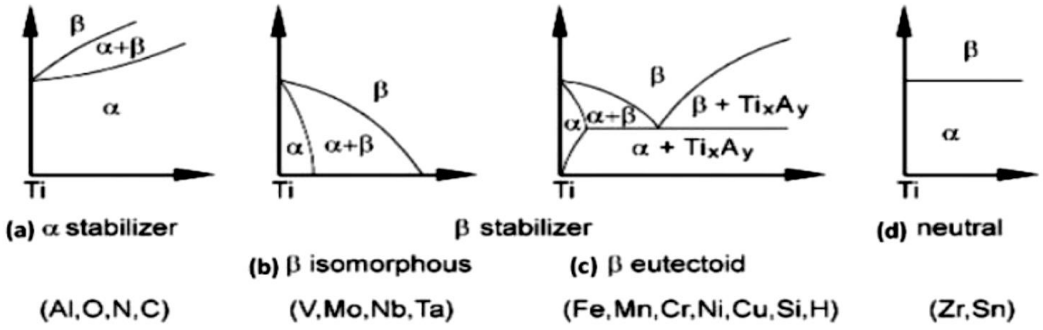

Figure 2.7: Effects of alloying elements on the α ↔ β phase transformation [2].

Some elements lead to an increase of the transition temperature; common examples are Al (substitutional element), O, N and C (interstitial elements). Elements with this property are called "α stabilizers". There are also other α phase stabilizers, like Sn, Zr, B, Ga and rare earth elements, characterized by limited solubility with the matrix. If oxygen addition is controlled accurately, it confers strength levels not attainable with commercially pure (CP) titanium [2]. Oppositely, other elements stabilize the β phase by "moving down" the transition temperature. α stabilizers can expand the biphasic α + β field although β stabilizers should reduce the transus temperature. Natural elements have a marginal influence on the transition temperature change. Some non-metallic elements are present in quantities less than 100 ppm in titanium alloys. β stabilizers can be divided in two categories: β isomorphous and β eutectoid elements. The elements belonging to the first category (such as Mo and Ta) are characterized by high solubility in titanium matrix, while low amounts of elements of the other category (Fe, Mn, Cr, Co, Ni, Cu, Si and H) may lead to intermetallic compound formation. Natural elements like Sn and Zr don't change the phase transition temperature, but may be added to strengthen the α phase [1].

2.2.5 Classification of Ti alloys

Corresponding to the chemical composition and the microstructure achieved at room temperature of different types of Ti alloys, they can be classified into five groups: (*i)* α alloys, *(ii)* near-α alloys, *(iii)* α+β alloys, *(iv)* metastable β alloys and *(v)* β alloys. This is shown in a three dimensional phase diagram which is formed from two binary diagrams that consist of α and β stabilizing elements, respectively (figure 2.8) [1], [2].

According to this diagram, α alloys comprehend either commercially pure (CP) ones or those that possess α stabilizers or natural elements. Besides, low ratios of β stabilizers provide the so-called near α alloys.

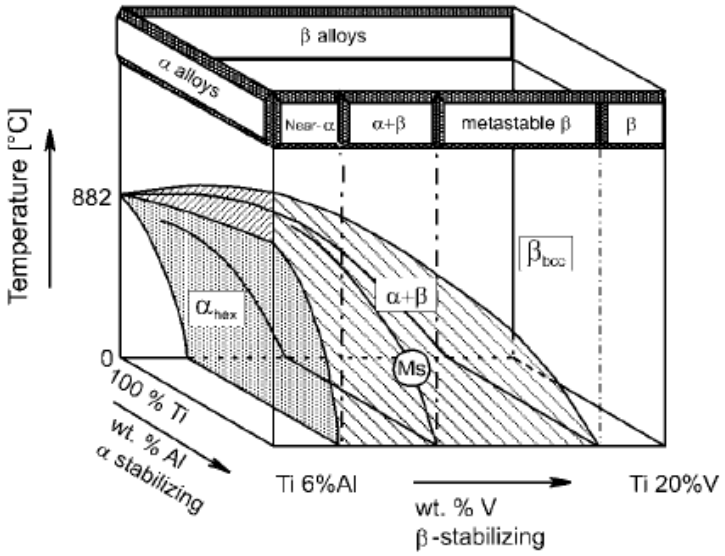

Figure 2.8:A schematical three-dimensional phase diagram of Ti alloys classification [1].

Equivalent amounts of Al and Mo according to the equations 2.1 and 2.2 can express the influence of α and β stabilizers elements in multicomponent alloys such as Ti-6Al-4V alloy:

$$[Al]_{equiv.} = [Al] + 0.17\,[Zr] + 0.33\,[Sn] + 10\,[O] \quad (2.1)$$

$$[Mo]_{equiv.} = [Mo] + 0.67\,[V] + 2.9\,[Fe] + 1.6\,[Cr]\text{-}[Al] \quad (2.2)$$

Also oxygen and nitrogen are known as α stabilizers and this behaviour can be described by the following equation:

$$[O]_{equiv.} = 2\,[N] + 0.67\,[C] + 10\,[O] \quad (2.3)$$

An illustration of α and β stabilizers effects are shown in binary diagrams in the figure 2.9. The upper part of this illustration shows the range of each class of Ti alloys according to the growing amounts of either α stabilizers and β stabilizers. Whereas, in the bottom part of that illustration, it is shown the martensitic start and finish ($M_s/M_{f)}$ transformation temperature change with some selected elements as stabilizers of each phases is shown [2].

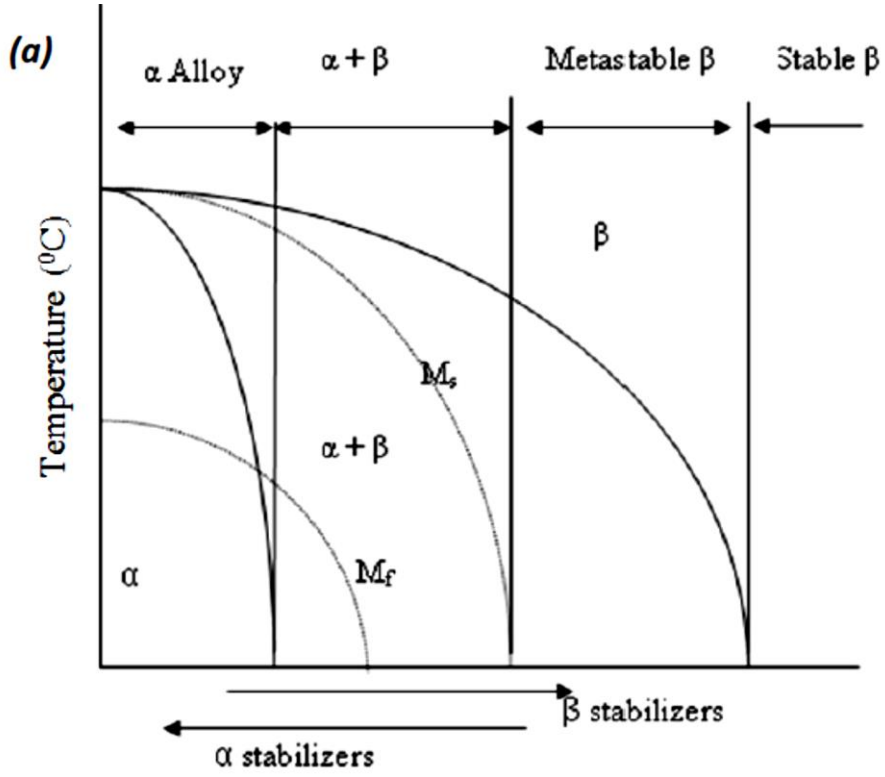

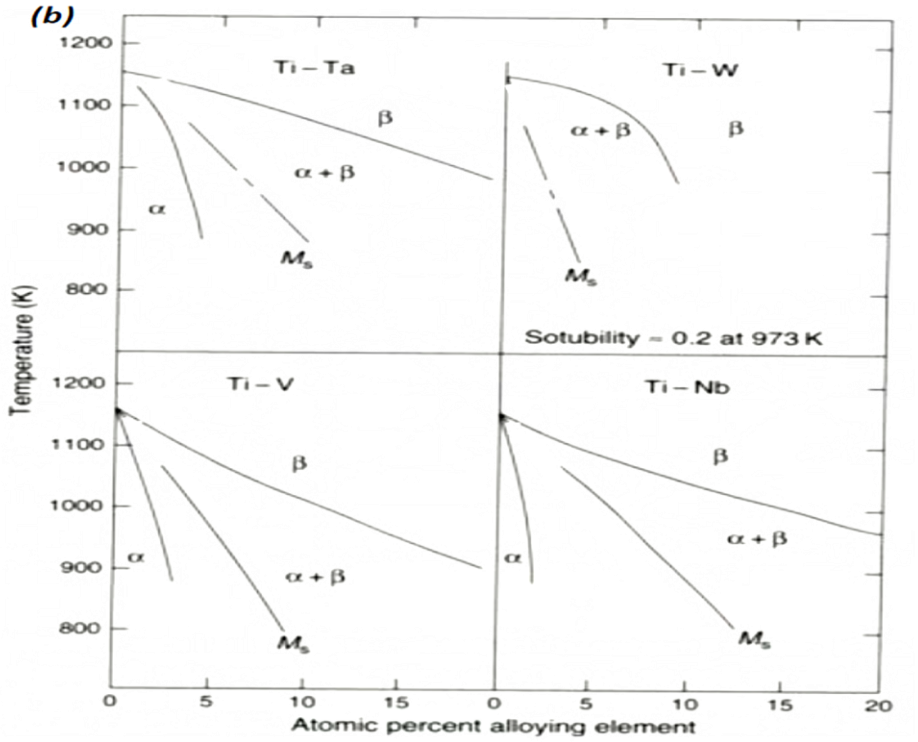

Figure 2.9: Binary phase diagrams indicating different categories of titanium alloys (a) and the effect of some alloying elements on the M_s temperature (b) [2].

2.3 Ti-6Al-4V alloy

The titanium alloys can be divided into three fundamental categories, such as α-alloys, β-alloys, and α+ β alloys. Their properties depend on their microstructure and, consecutively, rely on the chemical composition and thermomechanical processing. Ti-6Al-4V shows good machinability and high mechanical properties; also, because of the best performances among titanium alloys and weight reduction, it has lots of applications in aerospace industries and automotive and marine tools. As a result of its excellent biocompatibility, when it directly contacts with tissue or bone, it is one of the most important alloys in the medical field [4], [5].

2.3.1 Properties

In most applications, Ti-6Al-4V alloy is heat treated either for annealing or solubilisation and subsequent ageing. Some mechanical and thermal properties relative to these two conditions are reported in table 2.3 [4].

Table 2.3. Mechanical and thermal properties of Ti-6Al-4V relative to both main heat treatment conditions [4].

Material	**TS** (MPa)	**YS** (MPa)	**E** (GPa)	**Hardness** (HV)	**K** (W/(m · K))	**β transus** (°C)
Ti-6Al-4V annealed	895	825	110	340	7.3	995
Ti-6Al-4V solution + aged	1035	965	-	360	7.5	995

TS = tensile strength; YS = yield strength; E = elastic modulus; K = thermal conductivity

Temperature affects the mechanical and thermal characteristics of Ti-6Al-4V. Thermal conductivity raises to ≈ 24 W/(m K) at T = 1200°C; instead, hardness varies from 42 HRC to 32.5 HRC within the range of temperature from -200°C to 50°C. Young's modulus starts to reduce at T ≈ 200°C, with higher diminution rate from about 500°C. The ultimate tensile strength at room temperature diminishes more or less linearly by 45% at a temperature corresponding to 450°C.

The presence of α phase should increase yield strength, while the presence of the β phase should enhance elongation. Besides, a reduction of α phase thickness means an enhancement of yield strength and a reduction of β phase thickness brings about an increase of elongation.

Concerning creep tests performed on Ti-6Al-4V specimens, flow stress enhances with the increase of, at least, one of the following factors: strain, strain rate, hydrogen amount. In particular, the first two causes of flow stress increase are related to strain hardening phenomenon. Instead, flow stress decrease when the temperature is enhanced. The way hydrogen acts differently on tensile and compressive properties is particularly impressive. Tensile characteristics become undesirable as hydrogen content increases; this can be explained by formation either of solid solution of hydrogen in titanium and hydrides at phase or grain boundaries. Thus reciprocal grain flow becomes relevant because cohesive energy is reduced. Instead, compressive characteristics first improve at low hydrogen contents and, then, become undesirable at higher amounts. When hydrogen content (either in solid solution or in hydrides) is negligible, effects at grain boundary aren't dominant; besides, hydrogen stabilizes the more plastic β phase, enhancing compressive strength of the material. Anyway, a further increase of hydrogen amount leads to the same effects related to tensile characteristics, i.e. both solid solutions and hydrides reduce cohesive energy and produce reciprocal grain flow [6]. Ti-6Al-4V alloys that have been previously heat-treated and, consequently, are characterized by martensitic α'' + β microstructure manifest higher cold deformability than as-produced materials. Deformation twins are present more in α'' phase and contribute mainly to the deformation of materials containing 0.45 wt% of H. With the further enhancement of hydrogen content, the transformation β → α'' is favoured and

produce a strain increase due to the synergistic effect between deformation twins and martensitic transformation strain.

Addressing to the effects of other elements on mechanical properties of Ti-6Al-4V, deoxidized alloys show a decrease of hardness by about 10% [6], while materials subjected on nitrogen ion implantation prove to be harder than untreated ones because of hard TiN layer formation.

Ti-6Al-4V alloys are usually indicated as a good alternative of steel components when specific requirements of wear and friction behaviour are desired, such as pistons, connecting rods, valves, etc. Besides, they are characterized by extraordinary corrosion resistance and good fatigue strength, but not so relevant sliding properties; indeed, these alloys are very susceptible to galling and instability of friction coefficient. It is possible to improve such characteristics or by diffusion treatment (carburization, nitrurization) or hard coating (especially CrN and TiN) or shot peening.

In consideration of the fact that Ti-6Al-4V is a material of election for biomedical applications, some critical aspects arise by metal ions release, which may alter its intrinsic biocompatibility and irritate tissues locally around implants. A solution to avoid such inconveniences is to implant more biocompatible ions like calcium, silver, potassium [4].

2.3.2 Applications

Ti-6Al-4V is substantially employed for the following characteristics: it has got a high strength-to-density ratio (also called specific strength), corrosion resistance and stability until 400°C. For these reasons, Ti-6Al-4V is mainly used in aerospace, biomedical, automotive and marine sectors.

Concerning aerospace applications, this alloy has been originally developed for compressor blades for gas turbine engines. Later, by taking advantage of both Ti-6Al-4V superplasticity and its diffusion bonding feasibility, this material has been selected to produce parts with a high degree of complexity (blades, disks, airframes). Aerospace applications do not include just wrought Ti-6Al-4V; the same material has also been employed in cast form. Examples of cast parts are turbine engine housings with complex shapes, flow diverters, helicopter rotor hubs, missile wings and bodies, etc. Furthermore, this alloy has been chosen to link Space Shuttle with its fuel tanks and boosters.

In the automobile industry, Ti-6Al-4V is used for rotating and reciprocating parts (such as valves, connecting rods, valve springs) assembled in racing cars, where light alloys, in general, contribute mostly to their performances. Low density permits this material to be also applied for marine purposes, for example, to produce parts of hydrofoils and sonar equipment.

Biomedical applications of Ti-6Al-4V alloys include bone screws and hip, knee, elbow, jaw, finger and shoulder replacement joints, thanks to its low elastic modulus, sufficient tensile strength, good fatigue strength and biocompatibility.

As last but not the least, powder metallurgy technologies have attained remarkable interests; for example, BE technology permits the manufacture of parts with less than maximum density and the quite same strength of wrought alloys, but with lower ductility, fatigue

strength and toughness. Therefore, some applications of BE method are the production of a cost-effective preform for forging and other successive technological operations, connecting rods, missile fins, turbine blade preforms, hex stock preforms, lens housing [7].

2.3.3 Metallurgy

Ti-6Al-4V is an α + β alloy, containing in particular 6 wt % of aluminium, that stabilizes the α phase, and the 4 wt % of vanadium, that stabilizes the β phase. At room temperature the α phase (hcp) prevails, while the β one (bcc) occupies the remaining part. With different cooling rates and conditions of heat treatment (if it has been carried out), it is possible to obtain different types of microstructures: grain boundary allotriomorphic α, globular or primary α, Widmanstätten, basketweave and martensitic. When Widmanstätten platelets are found around globular α phases, this particular microstructure is denoted also as "bi-modal". Instead, it is generally recognized as "bi-lamellar" the structure that comprehends some of not yet transformed β phase regions within α Widmanstätten platelets and the same β regions themselves includes other thinner α platelets. If the alloy is initially heated up to a temperature within β (995 ± 20°C) or α + β fields of the phase diagram, then it is slowly cooled down, the dominant obtained microstructure is globular α. As the cooling rate increases, more α phase nuclei forms in correspondence of β phase grain boundaries and they grow into the original β grain with platelet shapes. With high cooling rates, the sizes of platelets become smaller because of contemporary effects of high nucleation rates and slow diffusion processes. With further enhancement of the cooling rate, also the nucleation rate within grains becomes significantly high, thereby obtaining a basketweave structure. After quenching, it is possible to find the presence of one of the martensitic structure: α' or α''. The first one is characterized by an hexagonal structure, while the other has got an orthorhombic structure. The development of one or the other martensitic structure and their amount are determined by the chemical composition of the starting unquenched β phase. As the volume fraction of the β phase diminishes, vanadium content in the same phase increases. When this content overcomes 15 wt %, β phase is stable even at ambient temperature (≈ 20°C). Instead, when the vanadium content inside the β phase is equal to 10 ± 2 wt % and the quenching process starts at temperatures ranging between 750 and 900°C, the resulting microstructure is made up in part with bcc β stabilized phase and the remaining part with a soft orthorhombic α'' martensitic structure. With quenching processes starting at temperatures above 900°C, the vanadium content inside the β phase is lower and, eventually, a martensitic α' structure is formed. Figure 2.10 shows the various microstructures obtained at different quenching temperatures along with a phase diagram of titanium alloys with increasing amounts of vanadium and the 6 wt % of aluminium, which puts in evidence the change of vanadium content in function of the starting quenching temperature. The grain boundary allotriomorphic α phases suddenly form as the temperature is just below the transus temperature, but this kind of structure is not clearly seen with slow cooling rates. It becomes more evident when cooling rates enhance and the platelets are formed [8].

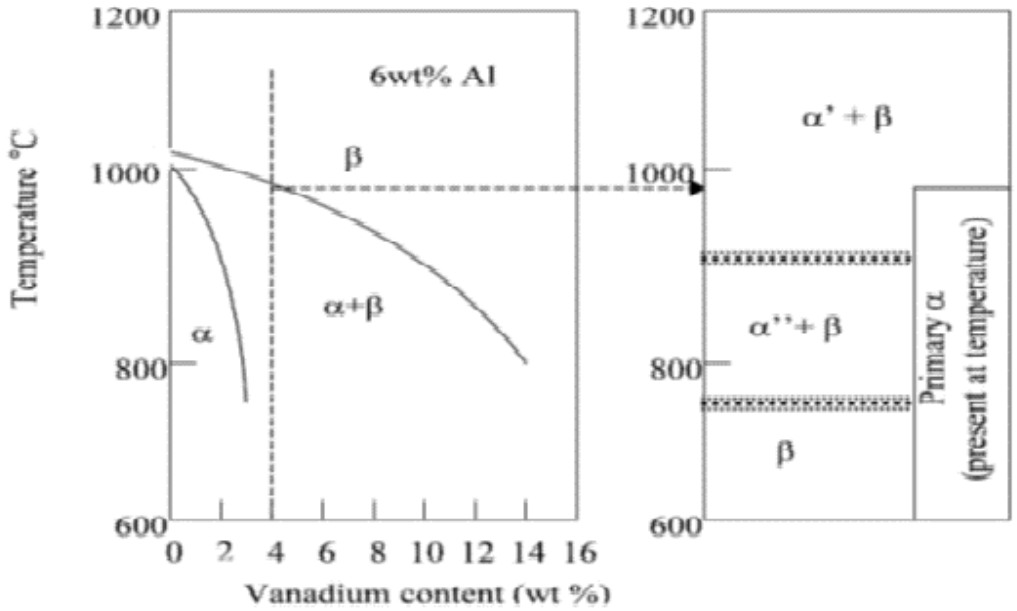

Figure 2.10: Schematic illustration of microstructures occurring in Ti-6Al-4V after quenching from different temperature [8].

2.4 *Solidification theory*

Understanding solidification theory helps to analyse phenomena such as final grain shapes and sizes, degree of segregation, the arrangement of inclusions, the appearance of porosity and other defects like hot cracks, etc. This process takes place through two steps: formation of first nuclei of solid phase and subsequent growth of related grains. In the following paragraphs nucleation stage (both homogeneous and heterogeneous), different ways of grain growth and the most important factors affecting microstructure and morphology of phases obtained after solidification will be discussed more in detail [9].

2.4.1 Nucleation process

In opposition to the case of melting, which occurs at melting temperature (T_m) in thermodynamic equilibrium, solidification requires a certain degree of undercooling, i.e. first nuclei of solid phase form at temperatures below T_m. With the contemporary presence of solid and liquid phases, a difference of Gibbs free energy develops ($G^L - G^S$); it means that the solidification process is energetically driven.

As written before, nucleation occurs either in homogeneous and heterogeneous ways. In the first case the solid phase nucleates directly within the liquid phase; instead, in the latter case, nuclei originate at interfaces between the liquid phase and other bodies, such as container walls and impurities embedded in the liquid. Both homogeneous and heterogeneous nucleation imply different levels of undercooling. In the first case, melt undercooling amounts to some hundreds of Celsius degrees; instead, in the other case, just a few degrees of undercooling are necessary (sometimes even 1 °C).

Although homogeneous nucleation is very seldom encountered in normal procedures of solidification, the explanation of this phenomenon is of fundamental importance to understand its mechanism. As represented in figure 2.11, a certain volume of liquid metal is characterized by an initial Gibbs free energy G_1. After the formation of a solid nucleus, this system evolves towards a final Gibbs free energy G_2. ΔG is defined as the difference between G_2 and G_1. G_2, G_1 and ΔG are expressed as below:

$$G_2 = V_S\, G_v^S + V_L\, G_v^L + A_{SL}\, \gamma_{SL} \tag{2.4}$$

$$G_1 = (V_S + V_L)\, G_v^L \tag{2.5}$$

$$\Delta G = V_S\, (G_v^S - G_v^L) + A_{SL}\, \gamma_{SL} = V_S\, \Delta G_v + A_{SL}\, \gamma_{SL} \tag{2.6}$$

where V_S is the volume of the solid phase, V_L is the volume of the liquid phase; A_{SL} is the interfacial surface area between solid and liquid phases, G_v^S is Gibbs free energy per unit volume of solid, G_v^L is Gibbs free energy per unit volume of liquid, ΔG_v the difference between G_v^S and G_v^L at a specific temperature, γ_{SL} the interfacial energy (or surface tension) between solid and liquid phases. Considering that ΔG_v is a negative quantity when $T < T_m$, it represents the driving force for solidification and, thus, its entity is dependent of undercooling. An idealized representation of the variation of Gibbs free energy per unit volume ΔG_v in function of temperature is displayed in figure 2.12 and it can be expressed as below:

$$\Delta G_v = \Delta H_v - T\, \Delta S_v \tag{2.7}$$

where ΔH_v and ΔS_v are defined as enthalpy and entropy variation between the two phases, respectively.

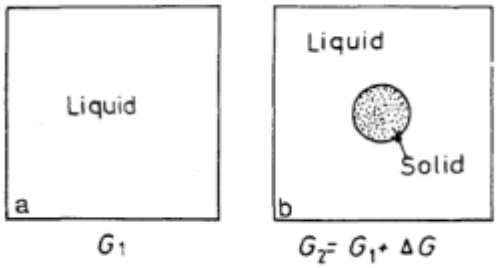

Figure 2.11: Portion of the considered thermodynamic system (a) before and (b) after the formation of a solid nucleus (b) [9].

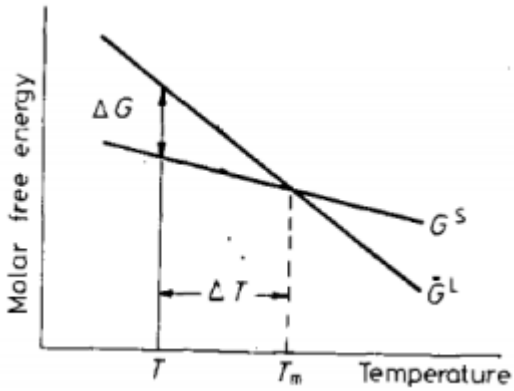

Figure 2.12: Variation of molar Gibbs free energy ΔG_v with respect to temperature. Curvature of both lines are neglected [9].

Considering that exactly at T_m both solid and liquid phases coexist in equilibrium conditions, there's no difference between their respective Gibbs free energies and, thus, equation (2.7) can be re-written as:

$$\Delta S_v = \frac{\Delta H_v}{T_m} = \frac{L}{T_m} \tag{2.8}$$

Where L is the latent heat of melting (or solidification if cooling process is considered) per unit volume. For most metals, it has been discovered by experimental activities that melting entropy is equal to gas constant R (8.314 J mol^{-1} K^{-1}). So, both ΔH_v and ΔS_v can be considered constant. By substituting L to ΔH_v, the following relationship results:

$$\Delta G_v \approx L - T \frac{L}{T_m} = \frac{L \Delta T}{T_m} \tag{2.9}$$

where ΔT is melt undercooling.

Considering a spherical shape for the solid that is forming, ΔG becomes:

$$\Delta G = \frac{4}{3} \pi r^3 \Delta G_v + 4 \pi r^2 \gamma_{SL} \tag{2.10}$$

Equation (2.10) provides a plot like that in figure 2.13. It's interesting to note how ΔG_v is a negative quantity while part of liquid transforms itself into solid, but this term competes with γ_{SL}, which is positive because a new interface is produced. The plot in figure 2.13 shows a maximum at r^*, the critical nucleus size. So, nuclei with $r < r^*$ (also called *embryos* or *clusters*) reduce their own energy by dissolving again into the liquid; oppositely, those with $r > r^*$ survive by further growing.

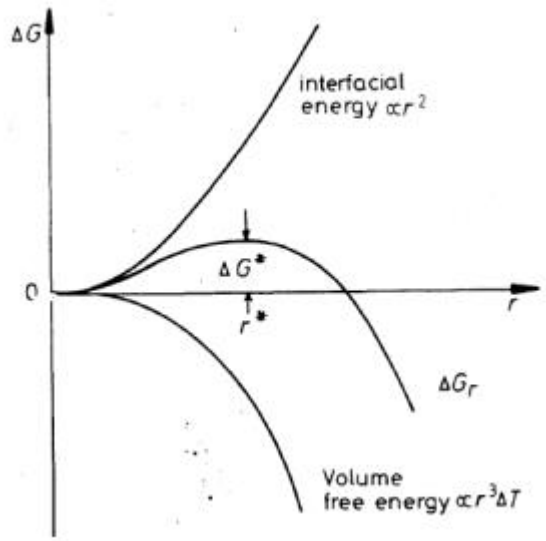

Figure 2.13: Trend of the overall Gibbs free energy versus the radius of a nucleus of spherical shape along with its components [9].

Differentiation of equation (2.10) gives the following results for r^* and ΔG^*, respectively:

$$r^* = \frac{2\,\gamma_{SL}}{\Delta G_v} = \frac{2\,\gamma_{SL}\,T_m}{L\,\Delta T} \tag{2.11}$$

$$\Delta G^*_{hom} = \frac{16\,\pi\,\gamma^3_{SL}}{3\,(\Delta G_v)^2} = \frac{16\,\pi\,\gamma^3_{SL}\,T^2_m}{3\,L^2\,(\Delta T)^2} \tag{2.12}$$

It's easy to note from equation (2.12) that energy barrier ΔG^*_{hom} decreases with undercooling.

Although homogeneous nucleation is easier to study than heterogeneous one, it is very seldom encountered in practice because, as it is shown later, its energetic barrier is higher to overcome than its counterpart is. Thus, heterogeneous nucleation occurs in the presence of a few degrees of undercooling.

Let's imagine a drop of solidifying metal on a substrate, exactly like a drop of water on a partially wettable solid. The critical heterogeneous nucleation energy barrier can be written as follows:

$$\Delta G^*_{het} = \Delta G^*_{hom}\,S(\theta) \tag{2.13}$$

where $S(\theta)$ is the shape factor, defined as:

$$S(\theta) = \frac{(2+\cos\theta)}{4} \cdot (1-\cos\theta)^2 \tag{2.14}$$

According to equation (2.14), $S(\theta)$ always results ≤ 1, thus $\Delta G^*_{het} \leq \Delta G^*_{hom}$. Lowest values of $S(\theta)$ are reached for $\theta = 0°$, that is when solid nucleus fully "wets" the heterogeneous nucleation substrate. This is the case of high coherency between solidifying metal and substrate.

When dealing with rapidity, the nucleation rate represents an important factor to consider. If the liquid is made up of C_0 atoms per unit volume, the number of embryos per unit volume (C^*) that have reached the critical nucleus size can be written in the following way:

$$C^* = C_0 \exp\left(\frac{-\Delta G^*_{hom}}{k\,T}\right) \ \ clusters/m^3 \tag{2.15}$$

These embryos become stable nuclei as one more atom joins one of them. Therefore, the homogeneous nucleation rate can be expressed as:

$$N_{hom} = f_0\, C_0 \exp\left(\frac{-\Delta G^*_{hom}}{k\,T}\right) \ \ nuclei/(m^3 \cdot s) \tag{2.16}$$

Where f_0 is a function of atomic vibration frequencies, the activation energy for diffusion in liquid phase and surface of critical nuclei. As ΔG^*_{hom} is proportional to the second power of $\frac{1}{\Delta T}$, homogeneous nucleation rate suddenly changes from almost 0 to very high values in narrow intervals.

With analogous reasoning, it's possible to get the expression for the concentration of heterogeneous nuclei of critical sizes:

$$n^* = n_1 \exp\left(\frac{-\Delta G^*_{het}}{k\,T}\right) \tag{2.17}$$

Where n_1 is the number of atoms in contact with the substrate per unit volume. Therefore, heterogeneous nucleation rate is expressed as follows:

$$N_{het} = f_1\, C_1 \exp\left(\frac{-\Delta G^*_{het}}{k\,T}\right) \tag{2.18}$$

Where f_1 takes up the same role as f_0 in equation (2.16) and C_1 is the concentration of atoms in contact with the substrate per unit volume. By observing that $\Delta G^*_{het} < \Delta G^*_{hom}$ because of shape factor influence, it can be stated that $N_{het} > N_{hom}$ for the same level of undercooling. Thus, few Kelvins of undercooling are sufficient for heterogeneous nucleation to occur [9].

2.4.2 Grain growth process

After nucleation, nuclei bigger than critical sizes start to grow and, eventually, meet each other, becoming grains. Surfaces that contemporarily belong to two adjacent grains are called *grain boundaries*. Grain growth takes place by continuous addition of atoms coming from the liquid phase. Two kinds of solid/liquid surfaces are commonly observed during the study of solidification processes of materials: atomically rough and atomically flat. The first one is typically encountered for metals. The second one is mainly observed in ceramics. Atomically rough solid/liquid interfaces continuously grow by the addition of other atoms.

Some factors affect interphase boundary shape: heat flow and its relative temperature gradient and chemical composition gradient, which, themselves, determines the microstructure, grain distribution and composition after solidification. In steady state conditions, three different kinds of interface propagation are observable: planar, cellular and dendritic ways. Planar interfaces propagate with the absence of substructure and heat flow is perpendicular to solidification front, according to the development of maximum temperature gradient. In cellular way interface propagation occurs under specific heat flow conditions and its

morphology is characterized by a parallel cellular structure with uniform width. Dendritic growth takes place along specific crystalline directions, called “easy growth directions”, determined by the optimal combination of maximum temperature gradient and growing direction. Dendritic morphology presents two different types: columnar and equiaxed. In the first case, groups of dendrites grow parallel to a general specific direction determined by heat flow, producing columnar grains that follow the same direction. Instead, in case of high levels of undercooling, groups of dendrites grow in many directions and form separate grains.

Also, chemical composition contributes to the morphology obtained after solidification has occurred: this effect is called “constitutional super-cooling” to separate it from “thermal super-cooling” explained before. To illustrate constitutional super-cooling, it’s better to deal with three cases that may take place during solidification processes:

1)equilibrium solidification, when solute diffusion both in liquid and solid phase is completed;

2)no diffusion in the solid phase, uniform solute distribution in the liquid phase, resulting from convection and diffusion;

3)No diffusion in the solid phase and poor solute distribution in the liquid phase because of the absence of convection. This is the most suitable case to explain morphology and microstructural phenomena occurring during EBM processing.

Microstructural characteristics are essentially affected by solute diffusion and thermal gradient within the liquid phase. In consequence of these two phenomena, both solute concentration and equilibrium temperature (T_e) vary in function of distance from interface, as shown in figure 2.14; because the analysed situation is very far from equilibrium conditions, effective profile temperature (T_L) is lower than T_e. Instead, solute concentration along the solid/liquid interface is equal to equilibrium liquid composition, which corresponds to points on the liquidus line in phase diagrams. Therefore, this liquid is said “super cooled”; protuberances emerging from planar interface propagates into liquid phase until, at their tips, $T > T_e$.

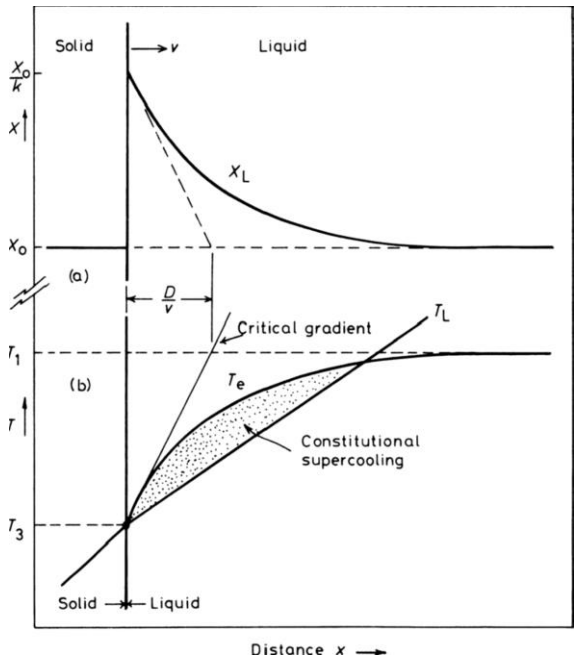

Figure 2.14: Explanation of constitutional super-cooling of alloys: (a) concentration profile and (b) temperature profile in both liquid and solid phases [9].

In opposite cases, i.e. when $T_L > T_e$, anytime that a protuberance tip is generated, it is melted again in liquid phase; thus, solidification takes place by planar growth.

There is a relationship between real gradient temperature within liquid phase G_L and gradient of composition G_C:

$$G_L = m_L\, G_C \tag{2.19}$$

where m_L is the liquidus curve slope.

G_C is expressed as:

$$G_C = - \frac{v\, C_0\, (1-k)}{k\, D} \tag{2.20}$$

where v is the growing rate of planar interface, C_0 the alloy composition, k the partition coefficient, defined as C_S / C_L, that is the ratio of the composition of contemporarily existing solid and liquid in equilibrium conditions, respectively, and D the diffusivity of solute through the liquid phase.

While keeping in mind expressions (2.19) and (2.20), if $\frac{G_L}{v} < \frac{m_L\, C_0\, (1-k)}{k\, D}$ or, in a more comprehensible form, $\frac{G_L}{v} < \frac{\Delta T_0}{D}$, where ΔT_0 is the difference between liquidus and solidus temperatures, planar growth can't take place. With different levels of liquid super-cooling, solidification can occur in cellular, columnar and equiaxed dendritic ways, as shown in figure 2.15; the higher the super-cooling degree, the more unstable the planar front.

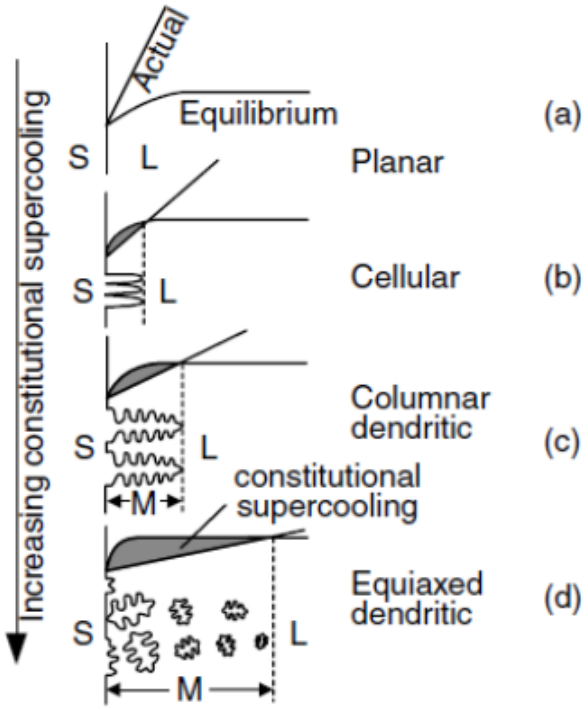

Figure 2.15: Effects of constitutional supercooling on different solidification modes [10].

2.4.3 Variables determining microstructure in the melt pool

Some additive manufacturing characteristics are in common with welding processes: thus, solidification by both these techniques produces very similar microstructures. Therefore, growth rate, thermal gradients, melt pool shape, heat source-travel speed, super-cooling and chemical composition of the alloy affects the microstructure of both welded and additively manufactured components.

The growth rate is defined as the propagation velocity of solid/liquid interface towards liquid and it is directly proportional to the heat source-travel speed. In particular cases where the heat source moves at a constant speed, such as welding and additive manufacturing, the solidification front advances behind it according to the following relationship:

$$R = v \cos\theta \tag{2.21}$$

Where v is the heat source-travel speed and θ is the angle between the front surface normal and the heat source speed. By considering a melt pool shape like that represented in figure 2.16-a and that the solidification front is perpendicular to the surface, it can be easily observed that R varies from 0 to v, these two values obtained when θ is equal to 90° and 0°, respectively. Locally, solidification front propagates normally to the surface and in parallel with maximum temperature gradient direction; anyway, also crystallographic factors determine the solid/liquid interface growth. Indeed, the alloy solidifies along its "easy growth direction", usually corresponding to close-packed ones. This behaviour accounts for the grain selection process, i.e. grains having easier growth directions favourably oriented with maximum thermal gradient develop to the detriment of those unfavourably oriented.

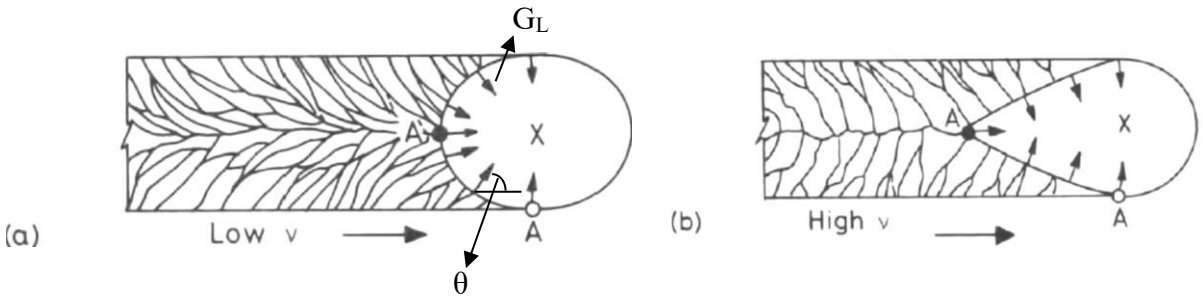

Figure 2.16: Representation of melt pools shapes obtained during low-moderate (a) and high solidification rates (b). Besides, it is also shown the grain growth pattern behind melt pools for each case [9].

Different heat source-travel speeds provide differences in melt pool shapes. This is because solid/liquid interface tries to follow the highest thermal gradient; thus, a change from a more elliptical shape to one drop-like is observed while heat source speed increases. The maximum temperature is found along the ellipse central line, as well as heat input. Rather high temperatures develop at the centreline of the solid just before interface; consequently, the temperature gradient along the same direction gets lower than other points of the solid/liquid interface. Melting latent heat dissipation velocity becomes higher because it is directly dependent on the propagation rate. Therefore, elliptical shape is associated with difficult heat removal, due to reduced thermal gradient along centreline. Limited heat source-travel speeds allow completion of the solidification of the melt pools following them. Instead, with higher heat source travel speeds, the melt pool becomes very similar to a drop. In this case, the pool is always delayed than heat source (because θ never equals 0°, even at the centreline), the thermal gradient is kept quite constant until the centreline and the grains don't deviate from their directions, as it happens in the case represented in figure 2.16-a.

Temperature gradients within solid and liquid phases determine the microstructure related to melt pool; among these, that one present inside the liquid is more indicative of melt pool morphological evolution. G_L is directly proportional to interfacial heat flux and convective phenomena, while its sign gives information on whether undercooling would take place or not. Different heating methods affect melt pool size: lower energy densities produce larger pools while increasing heat amount, in contrast with that occurring in techniques like welding and EBM.

Besides liquid phase thermal gradient at the interface (G) and solidification rate (R), also their product and ratio generate different characteristics of the melt pool microstructure; such an influence is reported in figure 2.17. Generally, cooling rates related to electron beam melting range from 10^3 to 10^6 K/s [2].

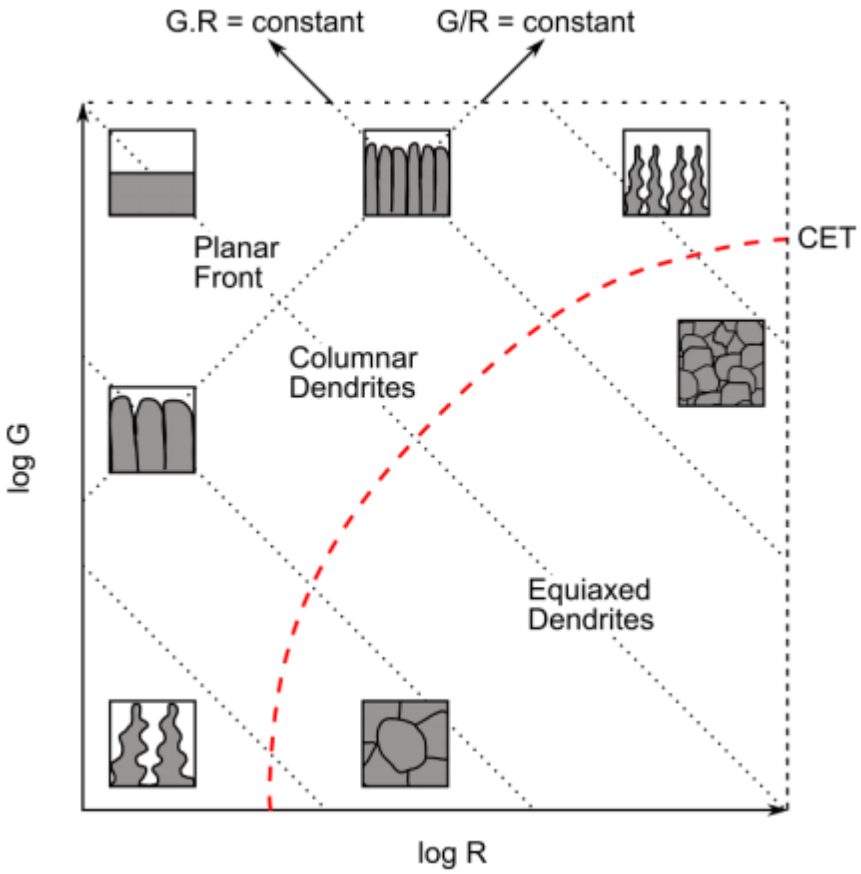

Figure 2.17: Solidification map indicating the microstructure obtained by given values of G, R, $G \cdot R$ and G/R [2].

2.5 Solid state phase transformations in titanium alloys

As the contemporary presence of both α (hcp) and β (bcc) phases determines specific properties in Ti-6Al-4V and other α + β alloys, it is important to understand how the transformation β → α occurs and induce particular microstructures. Based on different cooling rates, if phase changes don't involve diffusive processes, they are also called "martensitic"; otherwise, α phase nucleates and grows assisted by diffusion. α/β grain reciprocal orientation was examined by Burgers for zirconium and, later, confirmed also for the case of titanium alloys. The Burger orientation relationship is reported schematically in figure 2.18 and states that:

$$\{110\}\beta_{bcc} \parallel \{0002\}\alpha_{hcp} \;\&\; \langle 111\rangle\beta_{bcc} \parallel \langle 11\bar{2}0\rangle\alpha_{hcp} \tag{2.22}$$

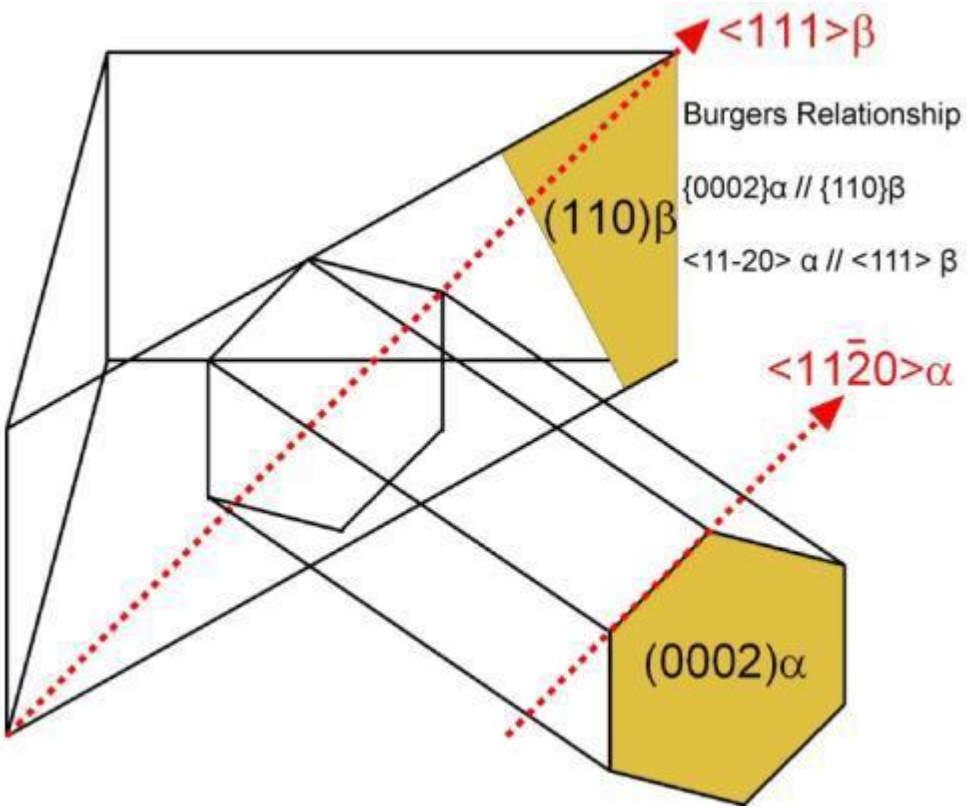

Figure 2.18: Schematic representation of Burgers orientation relationship occurring in materials like zirconium and α + β titanium alloys [2].

From such a relationship it derives that from α phase 12 variants of β orientations are formed, instead just 6 α orientations from β. Thus, it leads to 72 possibilities; anyway, without considering symmetrical arrangements, this number reduces to 57.

bcc β phase converts to various α morphologies in consequence of different cooling rates. Thus, the following transformations occur in α + β Ti alloys:

- *Diffusionless transformations*: β → α' or α'' (martensitic) with packet or lath morphology;
- *Competitive diffusionless and diffusional transformations*: β → α_m (massive) or α';
- *Diffusion-controlled transformations*: allotriomorphic α phase originating at the previous β grain boundary, colony α and Widmanstätten α structure revealed at gradually reduced temperatures, respectively.

Martensitic transformations occur at high cooling rates (oil or water quenching) and, consequently, do not involve any diffusional processes. Instead, diffusion-controlled transformations require slower cooling rates (air or furnace cooling). In titanium alloys, martensitic α' may be present in two different forms: massive packet and acicular morphology. Massive packet α' is made up with irregular structures comprising α' grains packets all oriented towards rather the same direction, while in acicular α' crystals pile up into different Burger's orientation. By increasing β stabilizing elements, hcp α' evolves itself

into α'' orthorhombic phase. For Ti-6Al-4V alloy, martensite-start (M_s) temperature ranges between 625 and 800°C [4].

Instead, transformations resulting in massive α (α_m) phase structure occur at medium cooling rates in competition with lamellar and martensitic α formation; the latter ones requiring low and high cooling rates, respectively. During the phase transformation crystal structure changes (from bcc to hcp), but not the alloy composition. Massive α_m doesn't grow as martensitic α' and α'' do; instead its transformation involves short distance movement of some atoms across the interface. Massive α_m nucleates at previous β phase grain boundaries at high cooling rates; instead, martensitic α plates develop within grain boundaries at lower cooling rates [2].

Diffusion-controlled transformations result into formation of allotriomorphic grain boundary α, colony primary α and Widmanstätten α phases with gradually reduced temperatures. Allotriomorphic grain boundary means that such α phase nucleates preferentially at grain boundaries of previous β phase because these can behave as efficient nucleation sites (figure 2.19-b, c). Such an α phase may develop in a continuous and discontinuous way. Discontinuous layers are associated with elevated cooling rates and high amount of β stabilizers elements. The relative orientation of α and β grains mostly follows Burger's relationship. Instead, by increasing the cooling rate, Widmanstätten α lamellae nucleate at allotriomorphic α phase interface and grow within β grains, at the same time keeping Burger's orientation (figure 2.19-d). One set of high aspect ratio α plates is named "*colony*"; these lamellae continue to grow and, eventually, can meet other ones arising from the other part of the grain and characterized by different orientation variants. Thus, the resulting microstructure (*lamellar*) is composed of α plates spaced by remaining β phase; such phase change requires diffusional processes. By increasing cooling rates, lamellae and colonies reduce their sizes. If cooling rates are sufficiently elevated, α grains also nucleate at colony plates interfaces because of further enhanced driving force (figure 2.19-e).

As a consequence of this, α plates grow randomly, anyway observing one of the 12 Burger's orientation variants. Such morphology is called "*basket-weave Widmanstätten structure*". In table 2.4 are summarized some results for the particular case of Ti-6Al-4V alloy.

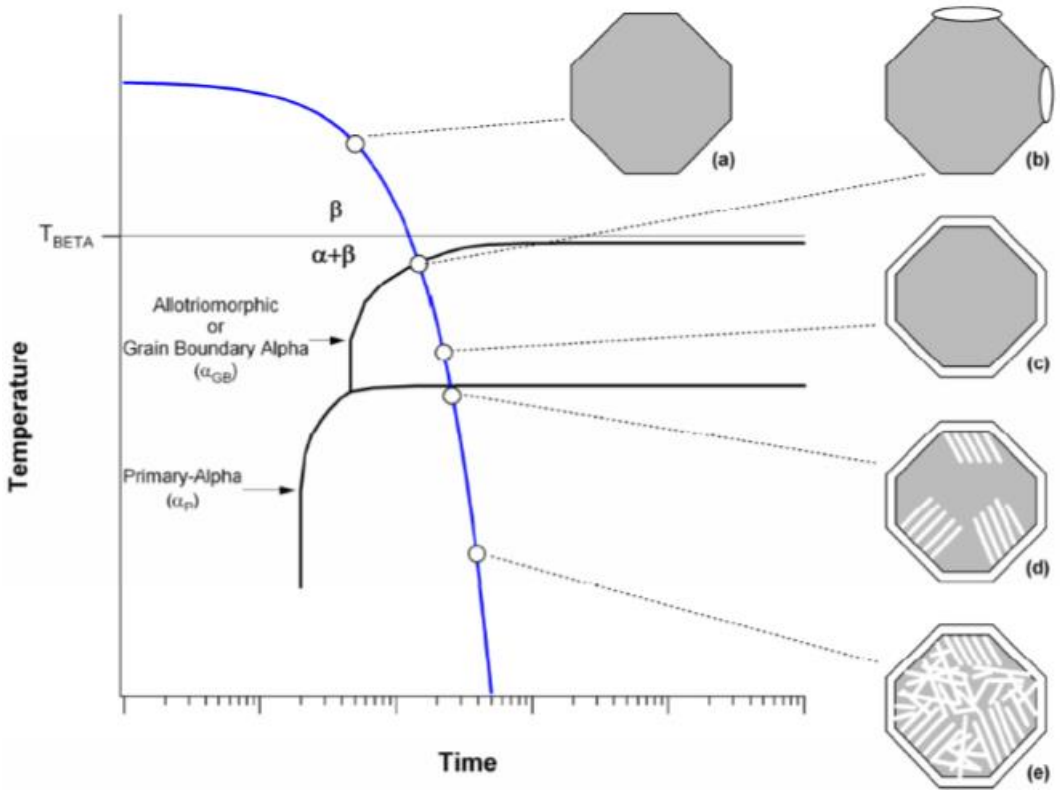

Figure 2.19: Schematic diagram reporting the sequence of diffusion controlled phase changes relative to continuous cooling of Ti-6Al-4V alloy through β transus temperature [2].

Table 2.4. Relationship between achievable morphology and cooling rates [2].

Cooling rate (K/s)	**Start temperature**	**Transformation**	**Notes**
CR > 410	M_S = 848 K	Martensitic (α') packet like or acicular morphology	Diffusionless process (β → α')
20 < CR < 410	1243 – 1273 K	Massive (α_m)	Competitive diffusionless and diffusion controlled process (β → α_m)
CR < 20	≈ 1173 K and 1223 K	Widmanstätten (α)	Diffusion controlled process (β → α with Widmanstätten morphology or at grain boundary)
	1243 – 1273 K	Allotriomorphic (grain boundary α)	

2.6 Additive manufacturing technologies (AM)

These technologies, similarly to other new production technologies, in recent years have found an important place in industrial fields to form physical models from virtual solid model data (CAD) in a very fast process. These technologies are used in different product fields, such as engines of vehicles, aerospace, machinery, electronics and biomedical products. The most important characteristic which presents the AM processes as excellent and advanced production technologies with respect to other old-style methods of production, is the manufacturing of the components by addition of successive layers, which leads to the production of components with complex geometries and shape without using any fixtures, tooling, moulds or other additional complementary equipment.

The AM techniques can be classified in six main category of manufacturing process:

1) Fused Deposition Modelling (FDM);

2) 3D Fiber Deposition (3DF);

3) 3D Printing;

4) Stereolithography (STL);

5) Selective Laser Sintering (SLS);

6) Electron Beam Melting (EBM).

A classification of materials for each type of AM technology is listed in table 2.5 [11].

Table 2.5. List of materials for each type of additive manufacturing technology [11].

AM Technology	Material	Ref.
FDM	Amorphous and semi-crystalline thermopastics Ceramics	Chua et al, 2003 Landers et al, 2002
3DF	Natural and synthetic polymers Ceramics	
AM	Powder bulk polymers Powder ceramics	Landers et al, 2002
STL	Amorphous reactive resin Ceramics Composites Hydrogels	Corbel et al, 2011 Melchels et al, 2010
SLS	Bulk polymers Ceramic Metals Composites	Chua et al, 2011 Melchels et al, 2010
EBM	Metals (powder state)	

In the following lines, some advantages and limitations corresponding to the application of the additive manufacturing technologies are listed:

Benefits:

1) Reduction in production time and low volume of wasted raw materials which, as a result, leads to reduction of production expenses. This saving is about 80% compared to the traditional-way production costs.
2) High quality of components produced with these processes can assist also the improvement of their mechanical and surface properties with respect to those expected with subtractive processes.
3) Producing different parts with complex geometries as represented by their CAD data is possible.
4) There's no need of any tools, moulds or punches that assist the production processes.

Limitations:

Commonly, these technologies are accompanied by some limitation, such as low velocity process production and low accuracy of build parts, part orientation, material properties, final quality of finished surface, pre-processing, post-processing and high costs of the production system. In the following, some restrictions about these technologies are mentioned:

1) "Rapid prototyping", the original name given to these technologies, causes a confused meaning, because additive manufacturing technologies aren't just applied for prototyping; also, they can be used to produce the designed finished products.
2) Non-linear AM produced parts. AM processes can produce components in different directions, which provides higher strength properties.
3) The rectangular cross sections of the produced sliced layers can't match with curved surfaces throughout their thicknesses and this phenomenon has effects on surface quality and roughness of produced parts.
4) One of the important factors for the production process with AM is the selection of adjusted layer thicknesses, because selecting the smaller layer thicknesses leads to higher resolution of the final components and longer data processing (with consequent waste of time) for small layers.
5) Applying support structures for building components can provide some limitations according to the production process; for example, with electron beam melting process, the problem of recycling the materials should be taken in mind when support structures are applied. This problem can have effects on the quality of the produced parts. Therefore, by choosing a most efficient build orientation for the components, this type of limitation can be reduced.
6) One of the most important advantages of AM processes may be that of directly producing the components, which leads to spread out the building metal parts in 3D with a significant strength and accuracy; unfortunately, some AM technologies as indirect methods cannot have the same advantages.

The cost of AM systems also constitutes one of the most considerable challenges concerning the production of components with these technologies. The high cost of AM systems is caused by high production costs or the availability of this method for a small number of users, which can be resolved by the high potential number of users and cost of production reduction

[12].

2.7 Applications of AM technologies

Because of their intrinsic capability of reproducing very complex shapes automatically, AM techniques can effectively decrease design and development time of objects. So, it's possible to summarize AM applications in 5 main sectors, later discussed in a more detailed way: aerospace, automotive, artistic, biomedical and architectural fields.

2.7.1 Aerospace and Automotive Industry

Everybody addressing their efforts to aerospace components design knows that plenty of them are manufactured with light alloys, such as titanium and aluminium. Anyway, the susceptibility to reactions with oxygen and nitrogen limits their large employment; this is especially the case for titanium alloys. Techniques like SLS and EBM make possible the production of titanium and aluminium alloys-made pieces. Some examples of such components are electrical generators, casting patterns of impeller compressor shroud, engine parts and elements certified for flights, thanks to AM techniques ability to fulfil desired mechanical properties.

Instead, other examples related to automotive fields are prototypization of the complicated gearbox housing, engine blocks traditionally obtained by sand casting methods and the production tool of a rear wiper-motor cover. These results are generally accomplished obtaining similar mechanical properties with 40% savings of raw-material [12].

2.7.2 Architectural Industry

It is commonly known that architectural creations generally involve manual work capability, with the considerable waste of time. AM techniques like stereolithography allow modelling of elements with good resolution and care of details with large availability of materials. Few examples of architectural parts reproduced by AM technologies are shown in figure 2.20 [12].

Figure 2.20: Artistic models fabricated by AM technology [12].

2.7.3 Artistic Industry

The application of AM methods in jewellery and arts provides a higher capacity to produce and design most complex shapes and fine jewellery models because of their high printing resolution. SLA methods can produce different types of models; for example, they are used as principle patterns to form the rubber moulds for the manufacturing of wax patterns utilized in investment casting processes to produce final parts. Also, through this technology, it's easy to produce unique shape parts within a short time [12].

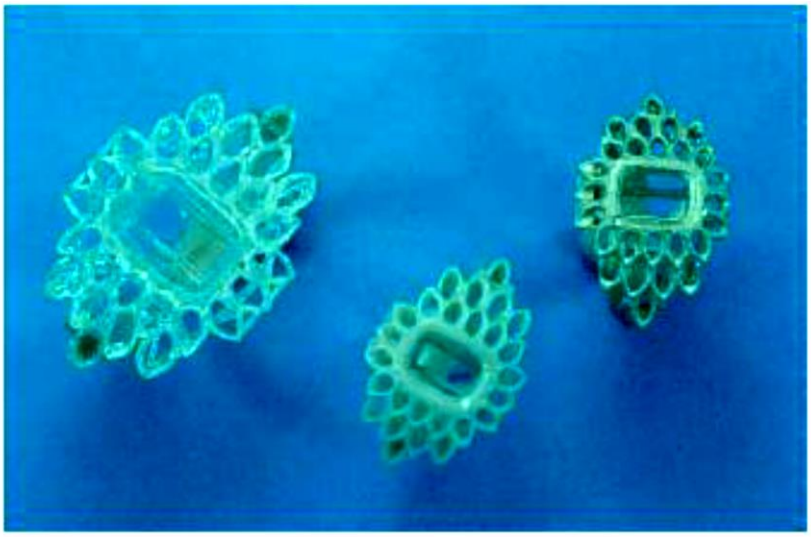

Figure 2.21: An investment cast silver alloy prototype of a broach (right), the wax pattern created from silicon rubber moulding (centre), and the two-time scaled SL built model (left) [12].

2.7.4 Medical Industry

AM technologies also show a high capacity in the medical industry with the different biomedical application, when this method coupled with other technologies such as CT or MRI can produce complex anatomical parts directly across scanned data (CT) images. The models built with AM technologies also provide a better simulation of specific anatomy that can help during pre-surgical planning and education of surgeons and medicine-faculty students to understand realistic surgery process; furthermore, it can have functions such as the better relationship between surgeons and patients. For example, the SLS method can be used for the production of dental implants, bone scaffolds and medical devices. While FDM reveals useful for applications to produce bone models and templates of complicated shapes.

2.8 AM technologies for metallic materials

AM is a group of technologies for the production of near net shape components by densification of layers of powders, wires, ribbons, with that undergo either partial or complete melting. A focused heat source produced by electron beam, laser beam, plasma or electric arc welding, melts the material whenever it is deposited onto a support or the previously processed layer. The final component is the result of a stack of layers locally melted on

selected points [2]. The classification of AM techniques is based on material feedstock, energy source, build bulk, etc. Therefore, these techniques are divided into three main categories: (i) powder bed systems, (ii) powder feed systems and (iii) wire feed systems.

2.8.1 Powder bed systems

After the powder bed is distributed, it is stabilized by the passage of a rake on the working area. A program communicating with the apparatus control the movement of the heat source that must have sufficient energy to sinter and, consequently, transform the starting powder bed into the desired shape (figure 2.22). Subsequently, another powder layer is deposited and raked again throughout the working are; the heat source produces the shape of the other layer and such operation sequence is repeated until the component is completely reproduced. The main advantages of these methods are the production of features with high resolution and of internal passages and the good control of dimensions. The maximum output volume of these systems is less than 0.03 m^3 [13].

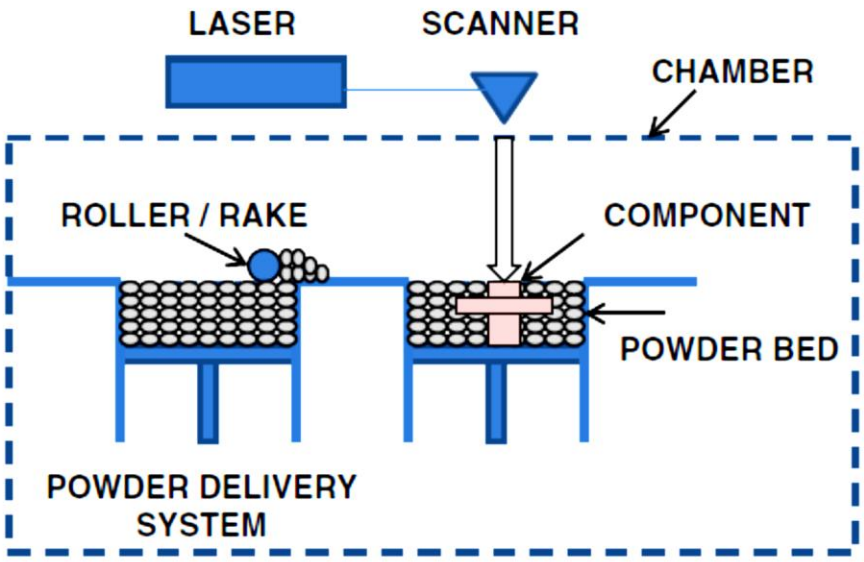

Figure 2.22: A schematic representation of an AM powder bed system [13].

2.8.2 Powder Feed Systems

These systems make possible the production of larger volumes of components compared to the previous ones. By these methods the powder of production is transferred through a nozzle onto the build surface (figure 2.23); a laser, driven by a beam guide system, is applied to melt the powder as monolayer which is subsequently transformed to the designed shape of the components. These operations are repeated several times to arrive to the final three-dimensional components. Nowadays, two types of these systems with different operation processes are distributed in the market:

1)the workpiece is stopped, while deposition head moves;

2)while the deposition head is stopped, the workpiece is in movement.

The two advantages of the last type consist of the ability on big volume creations and capacity to be used for repairing the damaged components [13].

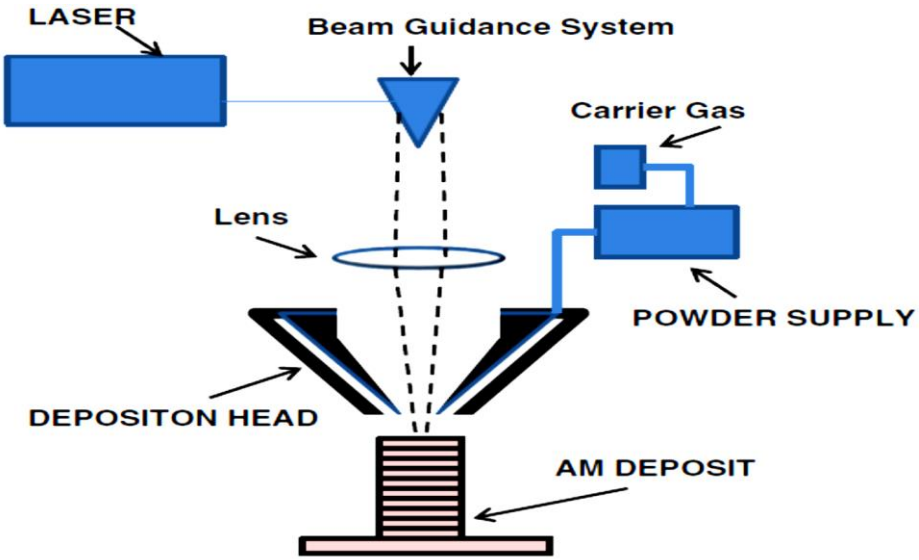

Figure 2.23: An illustration of an AM powder feed system [13].

2.8.3 Wire Feed Systems

The feedstock of these systems is a wire shaped material and their source of energy can be electron beam, laser beam and plasma arc. The operations of these systems begin by deposition of a bead form of material and subsequent passes upon it form the three dimensional components (figure 2.24). These methods are among the best and useful methods to produce components with high rates of deposition and build large volumes; by the way, more machining processes should be carried out with respect to powder bed or powder feed systems [13].

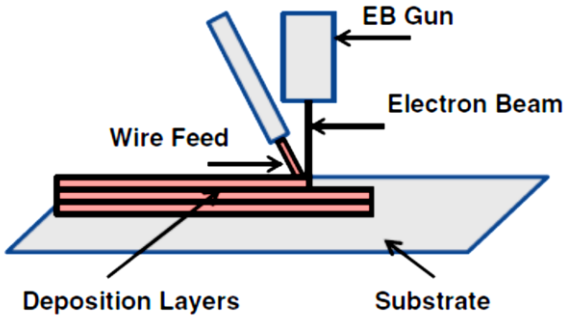

Figure 2.24: An AM wire feed system [13].

2.9 Electron Beam Melting (EBM)

The Electron Beam Melting (EBM) is an Additive Manufacturing (AM) Technology developed by Arcam AB with the contribution of Chalmers University of Technology (Gothenburg, Sweden). The procedure of melting electrically conductive materials was patented in 1993 and was put on the market in 2002. Up to 2015, six types of machine were available in the market [14].

EBM, like other AM techniques, produces components by operating on successive layers of the object, providing much freedom of design and reduction of lead-time. It is very similar to the SLM (Selective Laser Melting) technique; indeed, both methods employ interactions between the workpiece material and electromagnetic radiation of different kinds. In the first case, the interaction of an electron beam with some selected points of the surface leads to the melting of this zone; on the other hand, SLM utilizes a laser beam to melt selectively zones of the topmost layer. In either case, a 3D CAD system describes the beam direction to produce the part. In addition, the environment within the working chamber is different between the two techniques: EBM needs a high vacuum to decrease scattering phenomena between electrons and residual gas molecules, that doesn't represent a matter for SLM. For this reason, EBM reveals itself useful for manufacturing of particularly reactive metals, especially with oxygen and nitrogen. It led to a remarkable increase related to complex design objects produced with titanium alloys both for aerospace (turbine blades, airframe components, etc.) and biomedical applications (hip joints, dental root implants, etc.).

According to previous considerations, it could be inferred that EBM constitutes one of the most attracting study areas of last decades for its large number of advantages with respect to disadvantages (very limited). In the following paragraphs are examined closely the characteristics of EBM techniques, i.e. apparatus, advantages and disadvantages as well as main working parameters [15].

2.9.1 Equipment and conditions of work

In this paragraph the EBM machine is described in detail in order to elucidate the way electron beam is produced, the way metals in powder state are provided to the work plate before the interaction with the electrons and the way parts are obtained layer-by-layer.

A 3D CAD system sends information from each layer of constant thickness to the machine; as will be described later, this causes different deflections of electrons towards selected points of the part. In figure 2.25 is represented as a schematic picture of an EBM apparatus. The EBM machine operates with the action of free electrons expelled by a cathode, accelerated in order to increase their kinetic energy and focused on small spots, targeting the surface of the working part.

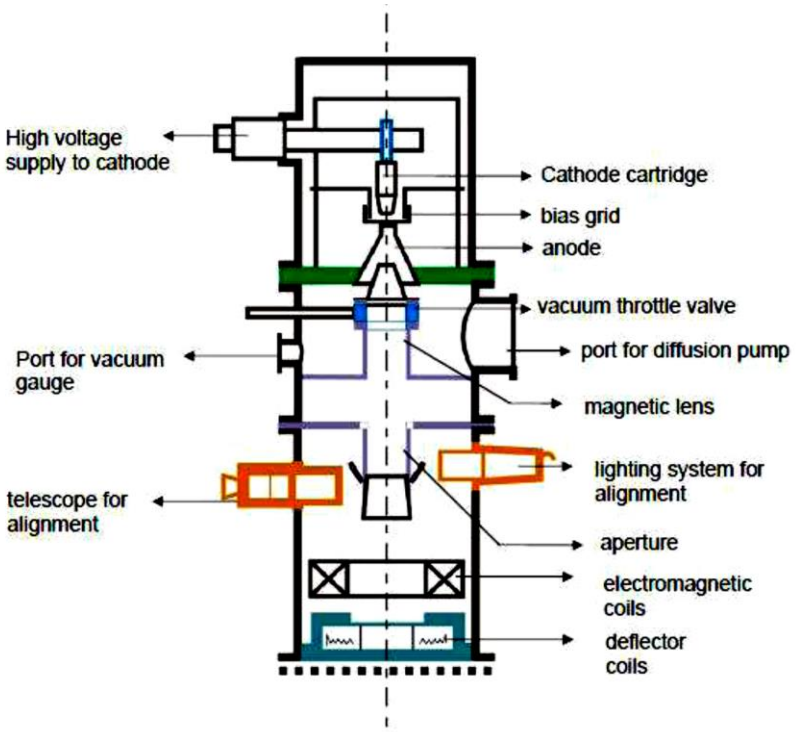

Figure 2.25: Schematic representation of an Electron Beam Melting Apparatus [16].

The cathode (made up with tungsten or tantalum or lanthanum hexaboride, LaB_6) is heated up to about 2500°C. This operation, along with the action of high vacuum produced within the working chamber, allows free electrons to leave the cathodic material by thermionic emission effect. Furthermore, the cathode is submitted to a negative bias that permits the electrons to escape rapidly from it. An annular negative bias grid is located after the cathode and avoids electrons divergence, to produce a beam directed towards the anode. The way of biasing the grid switches alternatively on and off the thermionic emission, allowing the machine to operate in a pulsed manner. As the electrons reach the anode, they further accelerate up to about half the speed of light. Subsequently, they run through magnetic lenses and apertures; the first ones limit the divergence of the electronic beam; instead, the last ones allow the convergent electrons to pass and block the divergent ones. The coordinated action of magnetic lenses and apertures determines the quality of the beam.

The last part of the machine is made up of an electromagnetic lens and a deflection coil. The electromagnetic lens focusses the beam to a spot of specific sizes; instead, the deflection coil makes the beam to follow a specific direction, producing holes of various shapes. Besides, there are lighting system and telescope to align the electron beam with the object [16].

A high vacuum environment (10^{-4} – 10^{-5} mbar) is generated within the working chamber, avoiding or limiting scattering phenomena between electrons emitted from the gun and entrapped air molecules, that lead to considerable kinetic energy decrease of the electrons themselves. Therefore, it is possible to work with metallic materials, particularly interacting with oxygen and nitrogen, such as titanium or aluminium alloys. Anyway, a small partial pressure of helium (10^{-3} mbar) is introduced to diminish electrostatic charging and "smoke" effects that, otherwise, will lead to powder dispersion and sudden interruption of the process.

Considering that the voltage applied to speed up electrons approaches 60 keV and that the resulting current ranges between 1 and 50 mA, a maximum of 3 kW could be obtained. Such power is sufficient to melt powder metals. In case of tungsten cathodes, powers of about 1 kW generate electron beam diameter of about 350 μm, in opposition to the more stable electron beams arising from LaB_6 cathodes. On the other side, the latter ones are very susceptible to "smoke" events.

The steps for the generation of each layer are represented in figure 2.26. A pair of powder tanks supply the material related to the layer in production, flattened by a "rake". Before melting occurs, EBM system proceeds with a pre-heating either to keep the chamber to sufficiently high temperature and to obtain a light sintering. After melting, the platform is brought down for the next supply of material and the cycle is repeated.

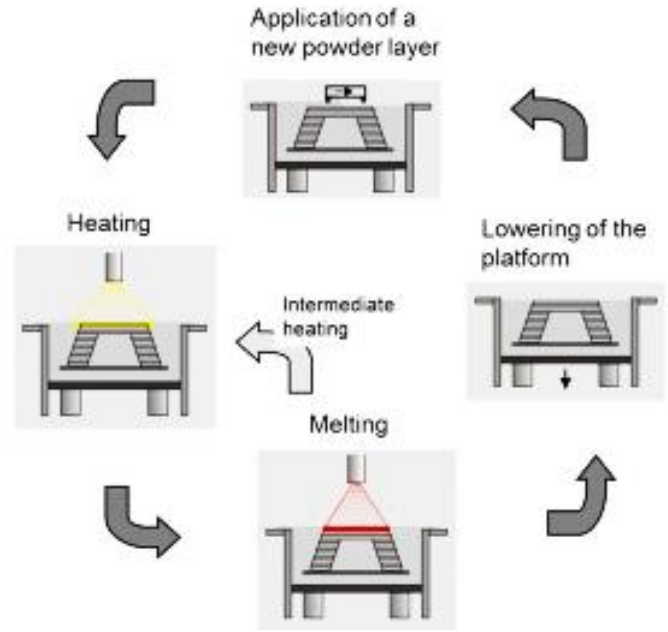

Figure 2.26: Cycle of operations characterizing the EBM process [15].

The amount of material dropped from the tanks must correspond to the layer thickness established by the CAD system. Exactly the first layer is deposited on a pre-heated steel platform (at a little higher temperature with respect to the chamber one). For better quality, it is strongly suggested to use platforms of similar materials. Besides, it's necessary to pay attention to the flow properties of the powder. These are strongly influenced by apparent density, i.e. the ratio between the dried mass of material and the total volume of the system, voids included. Thus, the optimal particle sizes range between 40 and 150 μm. Larger particles could be accepted, while smaller ones represent the cause of process instabilities and reduce drastically flow rate.

As written before, the topmost powder layer is subjected to several pre-heating scanning processes (figure 2.27-a), resulting in a light sintering of material. This procedure is carried out to rise electrical conductivity of particles and hinder reciprocal electrostatic repulsion,

which determines “smoke” events and eventually interruption of the process. With the presence of small particles, due to the possibility of “smoke” events, it would be better to control the pre-heating stage.

Chamber temperature assumes considerable importance as it affects both microstructure and residual stress onset. In particular, residual stresses are remarkably reduced, especially if compared with the SLM technique, which is usually carried out at lower temperatures.

The proper melting process occurs at lower scan rates (around 4 m/s) and just in selected points. The electron beam usually follows a path by parallel lines, jumping from one to the other through perpendicular ways, as represented schematically in figure 2.27-b. For surface roughness improvements, another melting stage takes place in “quasi-multi-beam” way (figure 2.27-c): this means that different beams “move” along the contours, by jumps of approximately 100 points [15].

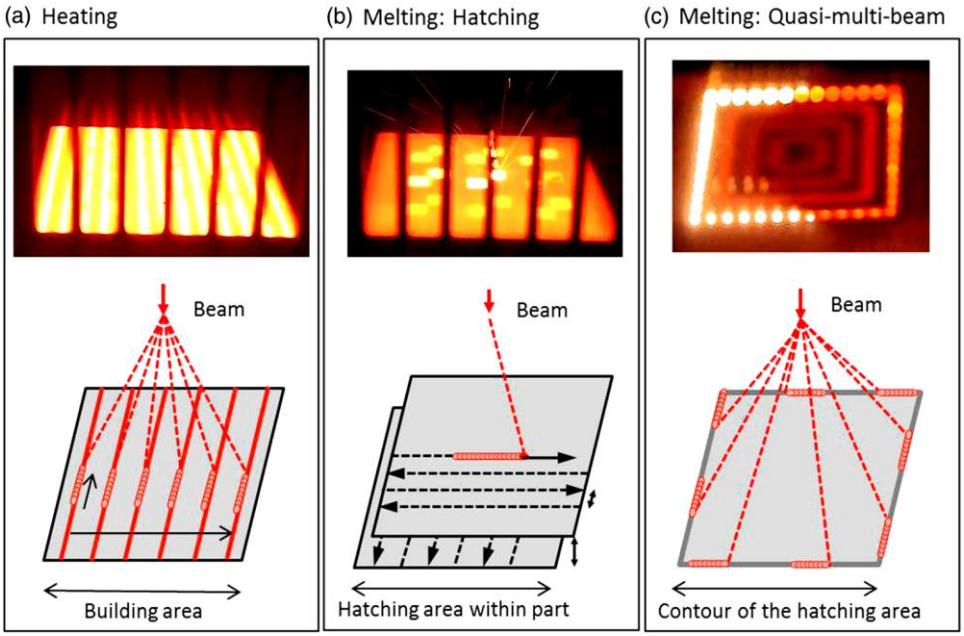

Figure 2.27: Thermal processes occurring during EBM operations and description of electron beam movements performed in each stage. In order: (a) heating by multi-beam scanning with a defocused beam, (b) melting by hatching, (c) quasi-multi-beam contour melting [15].

The following parameters affect the characteristics of the object to be produced:

- accelerating voltage;
- beam current;
- pulse duration;
- energy per pulse;
- power per pulse;
- lens current;

- spot size;
- power density.

Accelerating voltages and beam currents are fundamental parameters providing powers generated by an electron gun and transmitted to the workpiece. Considering that electron gun functions in a pulsed way, the pulse duration is controlled by input provided to the bias grid placed just after the cathode. Pulse time ranges from 50 μs to 15 ms. High pulse duration determines high energy per pulse. Instead, spot sizes are controlled by electromagnetic lenses. Larger spots correspond to both higher energy and power densities, which cause deeper material melting with smaller diameters [16].

Energy density is an important parameter affecting the microstructure of EBM-produced parts. Its relationship with other variables is written below:

$$E = \frac{P}{v \cdot h \cdot t} \tag{2.23}$$

where E represents the energy density of the electron beam, i.e. the energy per volume unit of the material, P the power generated by the electron gun, v the scanning speed, h the hatch width and t thickness of the layer [17].

2.9.2 Application of EBM

Although its versatility is among advantages of this technique, EBM-designed parts are typically used for automotive, aerospace and biomedical applications because of remarkable reduction of lead-time and scraps, unattainable with traditional manufacturing methods. EBM suitability comprises easy reproduction of very complex shapes and geometries as well. Some examples of these are irregular lattice or framework structures (leading to the realization of "meta-materials"), conformal cooling channels and interior cavities for optimal weight distribution. For high-performance fulfilments, racing car components may be rapidly prototyped. This technique is of choice in surgical applications for hip and knee implants and manufacturing of bone fracture-repairing plates, thanks to the possibility of working with both commercially pure and alloyed titanium; especially the first material is highly preferred due to its osteoconductive properties. In this case, advantages of EBM can be further perceived by the fact that implants customization is made possible by computer tomography (CT); in this way images arising from CT are translated in CAD model that is submitted to EBM machine [18].

2.9.3 Advantages and disadvantages of the technique

Similarly to other AM processes, EBM versatility constitutes the main advantage: there are no limits of shapes. It's possible to produce hollow parts without the usage of implements, cylindrical and spherical objects with a high degree of perfection and also highly detailed porous "geometries" of very different complexity. Indeed, as stated before, this technique is particularly needed in aerospace and biomedical application fields. Besides, EBM belongs to the category of near-net-shape manufacturing methods, producing the final part directly with no waste of material and obtaining high buy-to-fly ratios. Also, the high level of vacuum required for this technique represents an advantage because it makes it possible to work with

materials particularly sensitive to reactive environments. This fact determines the versatility of materials choice as well. Higher scan rates are easily obtained as the electron beam is electro-magnetically deflected, in contrast with SLM where the laser beam is directed mechanically to desired points. Nevertheless, EBM presents some disadvantages: high-vacuum conditions required for this technique lead to process instability by the creation of electrostatic charges and reciprocal repulsion of metal particles. Besides, EBM can be used in case of electrically conductive materials. As a last consideration, it should be mentioned that it's necessary to control some defects that may be present (residual porosity, un-melted particles, etc.) [2][3].

3. Experimental activity: materials, equipment and methods

3.1 Definition of samples

The methods that have been utilized are divided into two parts:

1. The first part considers the comparison of chemical composition, porosity, microstructure, contamination, oxidation, crystal size, particle size distribution, flowability, the number of satellites of the virgin Ti-6Al-4V powder, all related to the several recovery cycles in the PRS (powder recovery system) involving the powder.
2. The second part includes microstructure, porosity and diffusion in the Ti-6Al-4V bars produced by EBM.

3.2 Materials

In this work, Ti-6Al-4V powders prepared by Arcam AB corporation and with a nominal particle size distribution of 45 - 105 μm was used. This limitation on particle size distribution causes safe handling of the powders [4]. The gas-atomized Titanium Ti-6Al-4V powder was produced with particle sizes distribution between 45 and 100 μm. The same powder was also employed for the production of as-built bars. Figure 3.1 shows a SEM image of Ti-6Al-4V powders with the nominal particle size distribution of 45 - 105 μm [19].

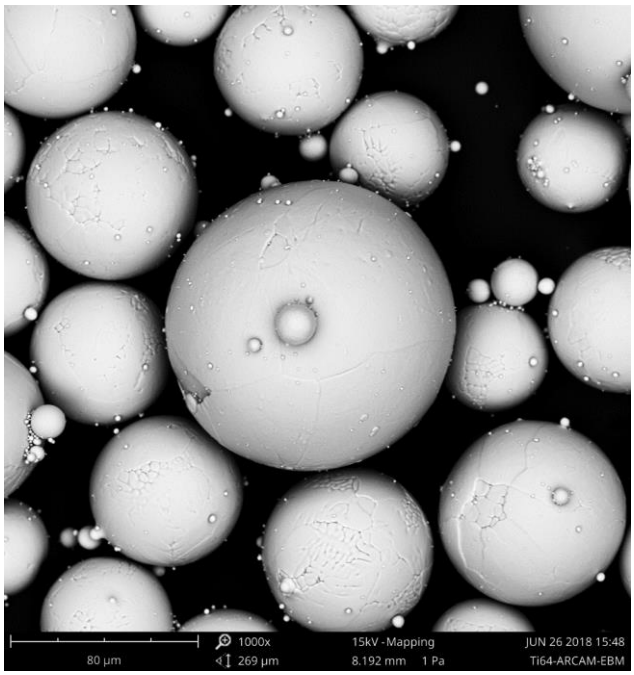

Figure 3.1: SEM micrograph of Ti-6Al-4V powders with nominal particle size distribution ranging between 45 and 105 μm.

The chemical composition of the Ti-6Al-4V alloy (supplied by Arcam AB corporation) is expressed in weight percentages and is shown in table 3.1.

Table 3.1. The chemical composition of Ti-6Al-4V alloy according to its datasheet.

	ArcamTi6Al4V, Typical	**Ti6Al4V, Required standard***	**Ti6Al4V, Required standard****
Aluminium,Al	6%	5.5-6.75%	5.5-6.75%
Vanadium,V	4%	3.5-4.5%	3.5-4.5%
Carbon,C	0.03%	<0.1%	<0.08%
Iron,Fe	0.1%	<0.3%	<0.3%
Oxygen,O	0.15%	<0.2%	<0.2%
Nitrogen,N	0.01%	<0.05%	<0.05%
Hydrogen,H	0.003%	<0.015%	<0.015%
Titanium,Ti	Balance	Balance	Balance

*ASTMF1108 (cast material) **ASTMF1472 (wrought material)

3.3 EBM system

3.3.1 Software

The prepared CAD model, initially saved as stl. Format and imported to a Materialise Magics ® software, is converted to the abp. file to be loaded in the machine. This software has the ability to divide the shape of the components into sliced parts in prediction of each layer thicknesses and this preparation is saved as abp. file; after that, it is imported to the EBM system. This file reports the geometric characteristics of each two-dimensional cross section of the designed shape, so that it could define different demanded manufacturing conditions, at the same time, for each layer. After introducing the abp files to the EBM control software, the process parameters subsequently are determined according to the theme that is assigned during the configuration of job by the Materialise Magics ® software for the fabrication of the final parts. The most important process parameters during the production of components by EBM include electron beam current, speed function and the line offset (a distance between individual scan line) [14]. The Arcam A2X EBM system which is used in this thesis is shown in figure 3.2 [20].

Figure 3.2: Arcam A2X EBM system used in this work.

3.3.2 Hardware

Mechanical parts of the EBM machine are places inside the build chamber and are divided in: raking system, build tank and hoppers. The building process is carried out in a vacuum chamber with steel walls; the view-port is made up with leaded glass. Because the interaction of the electron beam and the powder causes x-rays emission, the build chamber is designed to prevent x-rays emission outwards; in addition, it must bear high processes temperatures (up to 1100°C). The build chamber contains a build tank placed under the build platform. As each object layer has been produced, this platform moves down inside the build tank following the vertical axis (the z-axis). The vertical movement of the platform depends obviously by the height of the manufacturing part. The Arcam A2X system employed for this work has a build tank volume of 200 mm x 200 mm x 380 mm; thus, objects exceeding these sizes cannot be manufactured by this machine. The control unit is located at the left part of the machine and comprehends a computer, a signal amplifier, a programmable logic controller and a set of DC power supplies. A power unit is located under the control unit; it is used to regulate the heating of the filament and to produce the acceleration voltage of the electrons reaching the surface of the material to be processed. Two backing pumps are used to obtain vacuum level needed for the EBM process.

Two hoppers at both sides on the top of the build chamber contain the powders that are thrown onto the platform as the apertures are opened. A raking system spreads a calibrated amount of powders onto the platform, in order to have layers with nearly uniform thicknesses.

The high energy electrons interacting with the build part are produced inside the electron beam column, that comprehends in order a cathode and anode system, focus coils, deflection coils and astigmatism coils. When the filament (cathode) reaches a specific temperature, it starts to emit electrons that are directed towards the anode because of the application of a voltage. The electrons that don't interact with the anode are guided towards the powders

through the focus, deflection and astigmatism coils [14]. Table 3.2 reports some characteristics related to the Arcam A2X machine [20].

Table 3.2. Technical data of the Arcam A2X system used in this work.

Max. build size	200 x 200 x 180 mm (W x D x H)
Max. Bam power	3000 W
Cathode type	Single crystalline
Min. Beam diameter	140 μm
Max. EB translation speed	8000 m/s
Active cooling	Water-cooled heat sink
Vacuum base pressure	5 x 10-4 mbar (chamber pressure before start of process)
Build atmosphere	4x10-3 mbar(partial pressure of He)
He consumption , build process	1 litre/hour
He consumption, build cool down	50-75 litres/build
Power supply	3 x 400 V,32 A,7 kW
Size	2060 x 1066 x 2608 mm (WxDxH)
Weight	1681 kg
CAD interface	Standard: STL

3.3.3 Powder recovery system (PRS)

In the EBM process, almost all quantity of used materials can be recycled and they may be applied in subsequent steps of production; this leads to significant reduction of waste material. For this aim, the Arcam Corporation provides a powder recovery system (PRS) (figure 3.3) to recycle the powders and restore them to the normal cycle of production. The produced component having around semi-sintered block of caked powder is removed from the machine and a blast of sealed pressurized air is applied to separate the Ti-6Al-4V semi sintered block of cake and to recover the un-melted cake obtained during the production process.

Afterwards, treated powder by PRS system is the same as build powder which is collected and mixed with the recycled powders obtained from the semi sintered block of cake. After that, the collected powders are sieved and return to the EBM machine for the next process production without any contamination and additive materials [21]. Arcam group also proposed a powder handling trolley with the capacity to lift and carry the used powders from hoppers and batch containers to recycling parts.

Figure 3.3: Illustration of different equipment used in EBM process for powder recycling: (1) blast chamber (PRS), (2) vacuum cleaner, (3) sieving chamber used in this thesis.

3.4 Characterization methods

3.4.1 Powder characterization

3.4.1.1 Hall flowmeter (Flowability measurement)

For the characterization of the behaviour of new and recycled powders, the Hall flow tests were done to evaluate the flowability and angle of repose of applied powders (figure 3.4). These tests are carried out according to the ASTM B21317 standard, by weighting the 50 g of powder that must flow through a Hall funnel and by measuring the outflow time. The process of measurement includes evacuation of weighted powders from the orifice, which is initially blocked with the dry finger. When the test starts, the finger is removed from the orifice at the bottom part of the funnel; the measurement is repeated three times and their average times of measurement is considered as the flowing time of the powder. This test was carried out to understand the ability of powders to flow on the top of each layer of the EBM manufactured parts.

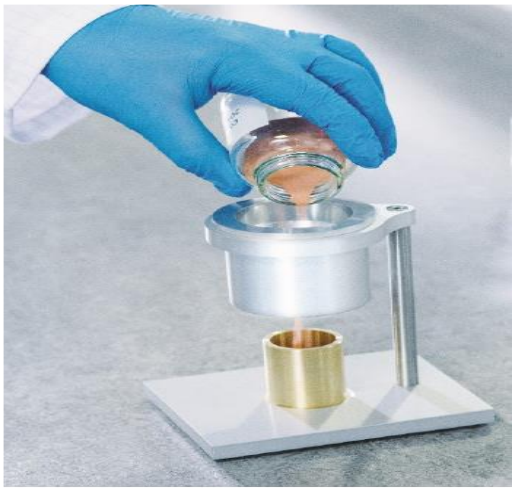

Figure 3.4: Flowability evaluation of Ti-6Al-4V powder using the Hall flowmeter.

3.4.1.2. Particle size distribution (PSD) by the sieve analysis (ASTM B214-07)

The measurement of the particle size distribution (PSD) was carried out according to ASTM B214-07 standard. Its low cost, high accuracy, repeatability features make this method interesting to evaluate the PSD of the powders. During this process, the shaker machine shakes the sieves that include the powders and then during the vibration, the powders are sorted in different sieves according to their sizes. An example of a sieve shaker is represented in figure 3.5.

In this work, a set of sieves with different sizes, such as 32 μm, 45 μm, 53 μm, 63 μm, 75 μm, 106 μm, 125 μm and 150 μm, was used to measure the particle size distribution of Ti-6Al-4V powders.

In this case, four types of Ti-6Al-4V powders were taken as samples coming from the different phases of production processes, which include virgin powders, the powders removed from first, second and n-cycles of production (from sintered cake and after PRS).

Initially, each sieve without samples was weighted, and it was taken note of the results; afterwards, 100 g from each sample were taken and separately the same weight was poured in the set of sieves; after closing the top set of sieves, the process of shaking begun. The time of shaking has been considered usually 20 min as it is recommended by ASTM; after that, each sieve, with collected powders according to the size, was weighted and the results were recorded. The difference between the first weight and the second weight and the average of these results provide the average particle size distribution of the samples [22].

Figure 3.5: Sieve shaker for sieve analysis [22].

3.4.1.3 Morphology and Elemental analysis

The Optical Microscope (OM) and the Scanning Electron Microscope (SEM) are two powerful instruments to study the microstructural morphology of the Ti-6Al-4V powders. Some of these powders were etched with Kroll's 1-3 ml HF, 2-6 ml HNO_3, H_2O up to 1000 ml OM was used both to observe the morphological aspect of the present phases (for the

etched powders) and to search for some internal porosity occurring within powders (that haven't been etched). Instead, the SEM was employed to both analyse the microstructure more in detail along with the presence of oxide layers on etched particles. Furthermore, not-polished powders were analysed via SEM to evaluate the morphology of the particles and estimate the satellite content of the powder. By using the potentiality of the SEM-EDS technique (Energy Dispersive X-ray Spectrometry), single point, linear and region chemical composition analyses were performed in different places on both etched and not-etched powders. In this way the chemical composition of each phase and impurities, those distributed especially on surface layers are revealed.

3.4.1.4 Cross-Section

Some of the analysed powders are taken at virgin state; other ones are collected both on and beneath the steel base plate and other ones are obtained after different passages through the powder recovery system. In order to investigate their microstructural morphology, the powders have been observed both at the OM/LEICA DM ILM (figure 3.6) and at a SEM/PHENOM XL (figure 3.7). Before microscopy investigations, the powder samples were preliminarily mounted in an electrically conductive thermoplastic resin Technovit 5000 containing mostly methyl methacrylate and dendritic copper particles, because it is possible to take advantage of its electrical properties for subsequent SEM observations (SEM samples must be conductive because of electrostatic charges accumulation on the surface of the samples would disturb the signal revealed). The mounting operation is carried out to make the sample easy to handle. The mix of the solid and the liquid resin (the latter acting as hardener) is poured in silicone rubber moulds where the samples (the Ti-6Al-4V powders in this case) were previously introduced. After the resin cured, the mounted samples were easily removed from the rubber moulds. This resin cures within 30 min. As the surfaces of mounted powders are not perfectly planar, the samples must be mirror polished in order to clearly investigate their microstructure. Figure 3.8 represents the result of the thermoplastic mount hardening with Ti-6Al-4V powders embedded.

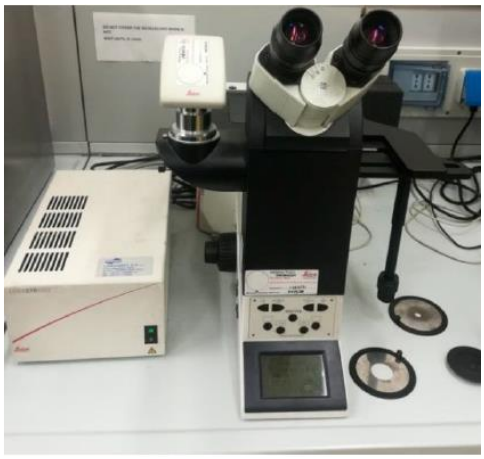

Figure 3.6: Optical microscope LEICA DM ILM.

Figure 3.7: Scanning electron microscope PHENOM XL[5].

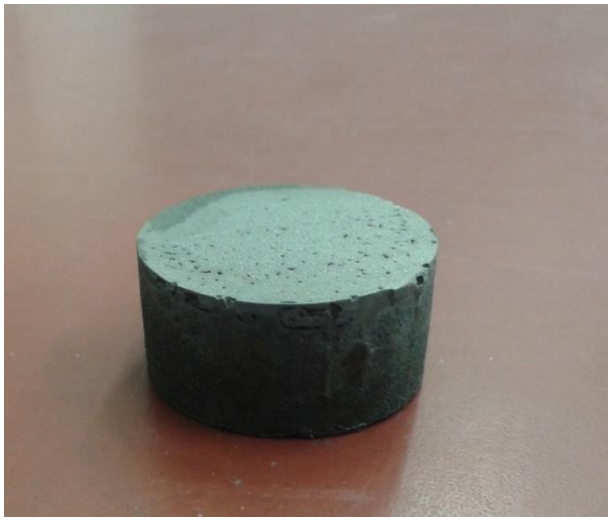

Figure 3.8: Powder mounted sample of Ti-6Al-4V.

As the surfaces of mounted powders are not perfectly planar, the samples must be mirror polished in order to clearly investigate their microstructure. Grinding and polishing is a procedure with material removal until roughness is remarkably reduced and samples show reflecting light brightness. The surface to be polished is placed onto abrasive papers rotating on a circular base driven by the motor of the grinder. Roughness is gradually reduced using silicon carbide papers of increasing fineness from 400μm to 2500μm, wet with water in order to avoid thermal deformations arising from friction. This series of passages is also called

grinding. Instead, mirror polishing is achieved by using the diamond pastes with different granulometry and with same roughness number of their rotating velvet cloth with 3 μm first and 1 μm for the last passages. Polishing passages are similar to those performed during grinding, except that the diamond paste was rubbed onto a velvet cloth rotating on the motor-driven base and a particular lubricant is added dropwise to avoid that the diamond paste dries. Mirror polished samples were cleaned with water and a common detergent and, afterwards, it was dried with a hair dryer. In this case, the Ti-6Al-4V powders were polished with a Mecapol P320 machine (figure 3.9) which was set up according to different revolution per minute (rpm). At the beginning, it was needed the high removal quantity of surface; so, the polishing procedure began with 300 rpm velocity. Subsequently, with gradually increasing the number of polishing papers, the machine was set up with 200 rpm, 180 rpm (in case of the velvet with 3 μm granulometry) and finally at 150 rpm (for the pad of 1μm) [6].

Figure 3.9: Illustration of Mecapol P320 polishing machine [23].

Porosities were measured with the method shown in figure 3.10, i.e. by using software integrated with the optical microscope. Such method discriminates the dense regions with pores and defects. The dense regions are coloured with red; instead, pores and defects are coloured with green. The software computes the area fraction of green area (corresponding to pores). Two different types of pores generally observed at the microscope are indicated by arrows: porosity from gas entrapment and pores induced by production process.

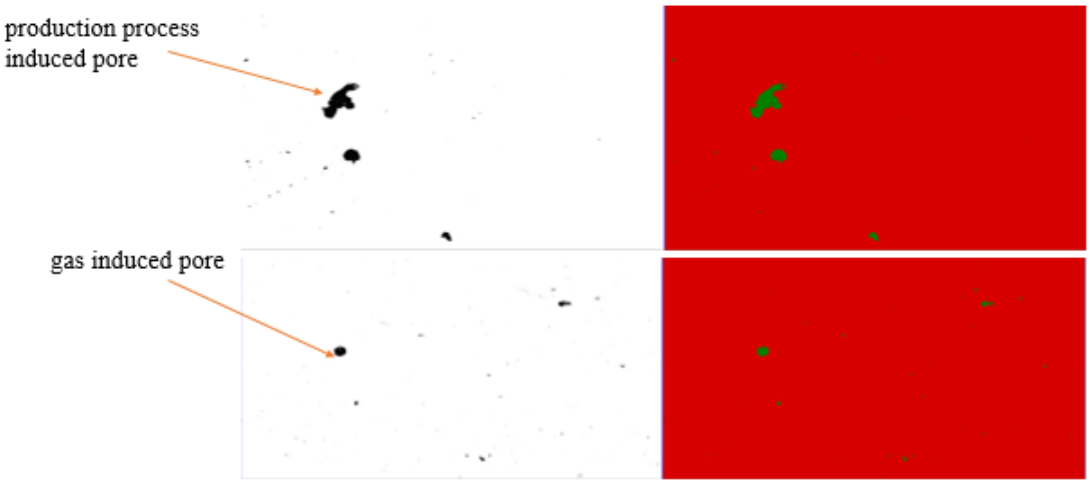

Figure 3.10: Illustration of the method used to calculate the fraction of the pore area.

The metallographic etching is a practical process to reveal the microstructural details of the considered samples that are not distinguishable in other levels of the polishing process such as grinding. In this work, the used etchant solution was Kroll's reagent, which is a dilute aqueous solution, with composition: 1-3 ml HF, 2-6 ml HNO_3, H_2O up to 1000 ml. 5 s time immersion for powder samples across a nipple in a special beaker were considered [24].

3.4.2 Bulk characterization

3.4.2.1 Metallography

To analyze the microstructure, porosity and elemental analysis of bulk samples, a standard metallography procedure for Ti-6Al-4V is used. Thus, different samples have been cut either longitudinally or transversally depending on the aim of the analysis:

1) four cylinders of same diameters (10 mm) and heights (15 mm) have been cut longitudinally for the evaluation of their porosities, obtaining also information about the diffusion depth of iron, nickel and chromium (arising from the steel plate of the EBM machine) inside them and information about their microstructure;

2) from a 60 mm tall cylinder with a diameter of 20 mm two cross sections have been cut at distances of 20 mm and 45 mm from the topmost surface; subsequently, the top remaining part has been cut longitudinally. In this way it is possible to observe the microstructure and the grains characteristics from different point of view. Also in this case the porosities in different positions of the sample have been evaluated;

3) a long and a short bar have been cut longitudinally in order to take microstructural and porosity information at different heights and positions. The cutting machine used to obtain bulk Ti-6Al-4V samples was a Remet TR 100S. The samples are clamped and an electrical motor transmits motion to a diamond blade to cut the specimen.

Thereafter, in order to handle the sample easier during the grinding and polishing they are mounted in a resin. So, for this reason, the bulk samples were cut along the XY plane in 10 and 30 mm diameter and are mounted in a thermosetting resin Technovit 4000 based on

methyl methacrylate with some addition of styrene that hardens within 30 minutes. Figure 3.11 shows the result of the thermosetting mount hardening. Previously prepared resins were poured in silicone rubber moulds where the materials to be examined were placed before. When hardening time ended, the mounted samples were easily removed from their moulds. As the surfaces of mounted materials are not perfectly planar, they must be mirror polished in order to clearly investigate their microstructure.

Figure 3.11: Bulk mounted sample of Ti-6Al-4V.

Polishing is carried out to remove cutting tool marks from the surface to be analysed and planarity defects arising from mounting.Grinding was performed by using silicon carbide papers of increasing fineness from 400μm to 2500μm, wet with water in order to avoid thermal deformations arising from friction. Instead, mirror polishing is achieved by using the diamond pastes with different granulometry and with same roughness number of their rotating velvet cloth with 3 μm first and 1 μm for the last passages. Also in this case a particular lubricant is added dropwise to avoid that the diamond paste dries. Mirror polished samples were cleaned with water and a common detergent and, afterwards, it was dried with a hair dryer. In this case, the Ti-6Al-4V bulk samples were polished with a Mecapol P320 machine, which was set up according to different rpm. At the beginning, it was needed the high removal quantity of surface; so, the polishing procedure began with 300 rpm velocity. Subsequently, with gradually increasing the number of polishing papers, the machine was set up with 200 rpm, 180 rpm (in case of the velvet with 3 μm granulometry) and finally at 150 rpm (for the pad of 1μm).

3.4.2.2 Microscopy analysis of samples

3.4.2.2.1 Optical microscopy

The metallographic etching is a practical process to reveal the microstructural details of the considered samples that are not distinguishable in other levels of the polishing process such as grinding. In this work, the used etchant solution was Kroll's reagent, which is a dilute aqueous solution, with composition: 1-3 ml HF, 2-6 ml HNO_3, H_2O up to 1000 ml. 10 s time immersion for powder samples across a nipple in a special beaker were considered [24]. This

procedure is used for reveal the microstructure of the samples; instead, when their porosities have to be evaluated, the etching procedure is not required.

As the polishing process of samples, they are ready to be analysed morphologically or microstructurally by optical microscopy. Of course, an optical microscope is included among the most important instruments to investigate the microstructure of metallic materials. In this thesis, a LEICA DM ILM (figure 3.6) was used to observe Ti-6Al-4V bulk samples.

3.4.2.2.1 Scanning Electron Microscopy (SEM)

The metallographic etching is suitable to reveal the microstructural details of the considered samples that are not distinguishable in other levels of the polishing process such as grinding. Etching is not always needed for revealing some visible features, such as porosity, cracks and inclusions [7]**.** In this work, the used etchant solution was Kroll's reagent, which is a dilute aqueous solution, with composition: 1-3 ml HF, 2-6 ml HNO_3, H_2O up to 1000 ml. So, 10 s time immersion for bulk samples across a nipple in a special beaker were considered [24][8].

To complete the process of analyzing the structure of metals, it was needed to know the microstructure and the chemical composition of the materials. For this aim, a scanning electron microscope (SEM) was applied**.** A scanning electron microscope examines the secondary electron beam produced on a surface to create an image analysis of the structure of the materials. The beam that has interacted with the surface includes electrons that are produced from different types of signals that provides information about surface topology and composition.

In this work, a scanning electron microscope PHENOM XL (figure 3.7) was used to analyse the samples; this microscope was equipped with a four-segment Backscatter detector (BSD), which gives the images with high resolution and information about chemical composition. The Phenom XL is fitted out with two different systems of detectors. The first one is the EDS system for elemental analysis, and the second one is the secondary electron detector (SED) to provide precise images from the surface. Also, to control the EDS system, EID software is used to know all existing materials in the samples according to the periodic table.

In this case, to analyse the powder and bulk samples, Elemental Mapping & Line Scan has been used. The elemental mapping, according to different selected elements, can show the distribution of elements throughout the sample; instead, the line scan identifies the quantity and the distribution of elements along a line drawn on the picture of the structure [25].

3.5 X-ray diffractometer

X-ray diffraction (XRD) is one of the best ways that is used to define and quantify the crystalline phases present in a material. In this work, the PANalytical Xpert3 X-ray diffractometer (figure 3.12) was used in Bragg-Brentano configuration with 40 kV and 40 mA (between 20° and 100°) to analyse raw and used powders in different levels of the process production. Sending an accelerated electron beam with a suitable tension on an aim material, the special characteristic x-rays produced by the aim material are emitted, collimated and sent on the specimen to be analysed. The interaction of x-rays with the material produces constructive interference which can satisfy Bragg's law. The x-rays

diffracted and emitted by the material are collimated towards a detector and they can produce a diffraction spectrum that allows to know the crystalline phases present in the material.

Figure 3.12: The PANalytical Xpert3 X-ray diffractometer [26].

4. Results and discussion

In this work, the following materials were studied:

- the virgin powder samples;
- top and bottom sintered powders, namely coming from the top part and bottom part of the start plate holding the samples built in EBM machine;
- Powders produced after powder recovery system after one, two and n-cycles of EBM process. Furthermore, the effect of times of reuse or recycling of Ti-6Al-4V powders on reliability and affordability of additive manufactured built parts were observed.

For this aim, Ti-6Al-4V powders have been characterised in terms of flowability, particle size distribution (PSD), cross-section microscopy observations, SEM analysis (including morphology, contamination/oxidation and chemical composition studies) and, in the end, XRD analysis for phase composition and crystal size examination.

4.1 Powder monitoring

4.1.1 First cycle of the production process

The flowability measurement of the reused Ti-6Al-4V powders was recorded according to the ASTM standard per 50 gr of powder. Indeed, the flowability of powder constitutes an important factor that influences the continuity and uniformity of each layer of the building product. In the first cycle of production, because of the elimination of fine particles and reduction of the satellite content , it was observed a clear increase in flowability and particle size distribution of Ti-6Al-4V powders. Figure 4.1 shows a comparison between flowability and particle size distribution of the virgin sample and PRS powders after the cycle of PRS performed after the first cycle of EBM job.

Cycle 1

	Virgin	After PRS
Flowability (s/50g)	23.77 ± 0.28	21.47 ± 0.35
PSD	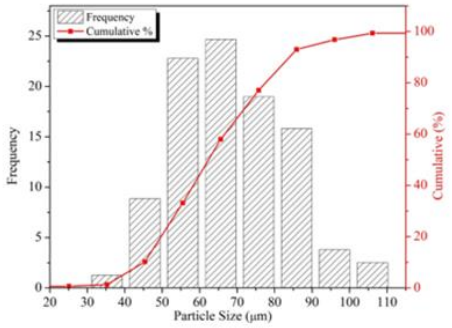	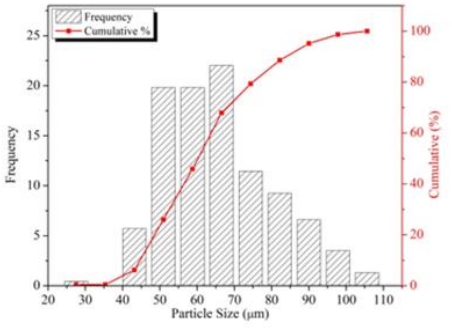

(a) (b)

Figure 4.1: Comparison of the flowability between (a) virgin sample (b) after one stage of PRS performed after the first cycle of EBM job.

As it is observable in figure 4.2-a, Ti-6Al-4V particles are surrounded by many satellites which is the typical feature of gas-atomized powders. At the first cycle it was observed that, in comparison with the virgin particles, characterized by the high quantity of satellites and smooth spherical forms without impurity, the powders after the first recycling undertook a little irregular form and some contaminations on the surface of the particles arisen from Fe. Besides, sieving brings about a reduction of percentage of satellites because it removes agglomerated particles or partially sintered particles.

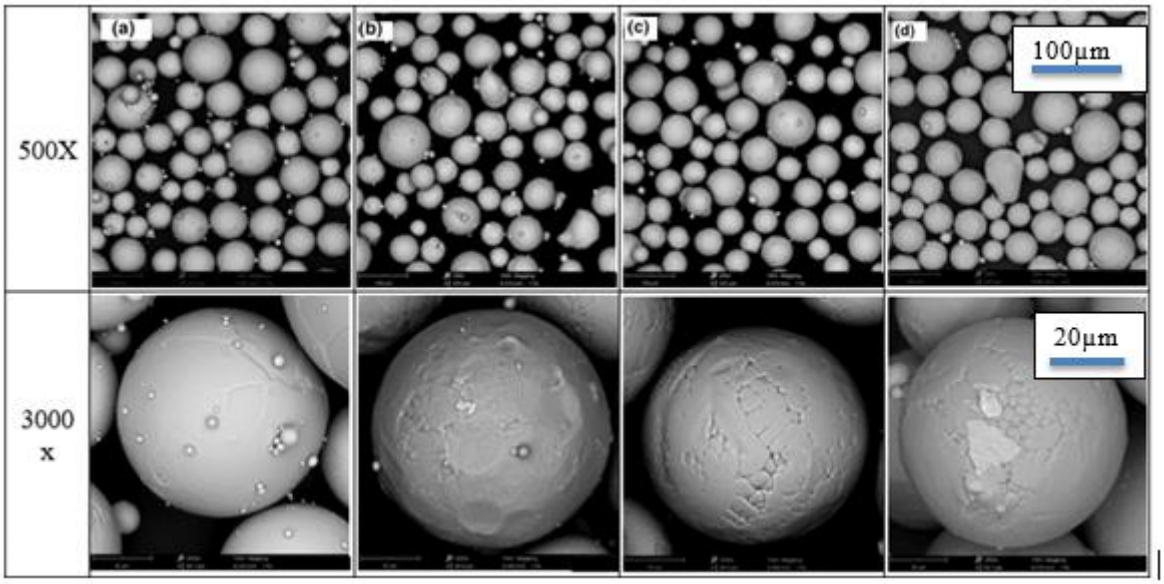

Figure 4.2: Morphological illustration of (a) virgin powder samples, (b) top and (c) bottom sintered powders and (d) after PRS performed after the first cycle of EBM job with magnifications of 500 x and 3000 x.

Figure 4.3 reports optical microscopy images of virgin, top and bottom sintered Ti-6Al-4V particles and powders after one stage of PRS performed after the first cycle of EBM job. The upper images are related to not-etched powders and reveal the presence of both irregular shapes (not perfectly spherical) and pore inside some particles. In particular, these internal pores derive from gas bubbles entrapped in molten metal during production processes of the same particles (gas atomization). If a bulk sample contains such gas pores, these derive from particles with gas pores inside. Instead, the bottom images in figure 4.3 represent the powder material etched with Kroll's solution. The microstructure change of Ti-6Al-4V powders is related to the number of reused times. As shown in figure 4.3, the cross-section of the particles differs for each type of powders. For the virgin particles, the dominant phase is α or martensitic α' and, after the first cycle of production, it would seem that the β phase appears in the structure of the particles; also, all cross-section images reveal that the particles have a thick lamellar structure.

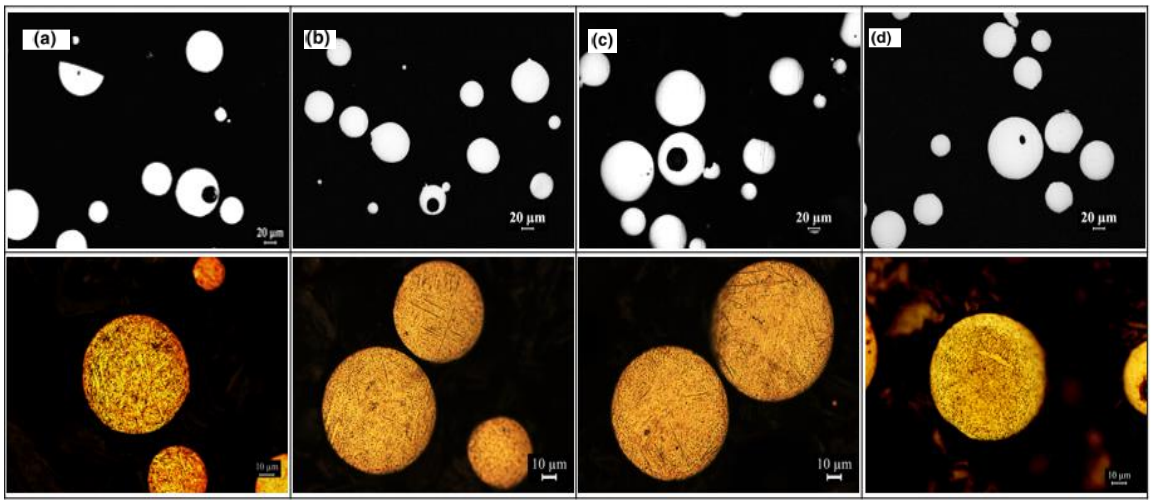

Figure 4.3: Optical images of (a) virgin powder samples, (b) top, (c) bottom sintered powders and (d) after PRS during the first cycle of production in the states of un-etched (above) and etched samples (down) with magnifications of 100x and 200x, respectively.

Figure 4.4 illustrates the microstructure and oxidation conditions of virgin, top and bottom sintered powders and powders obtained after the recycling performed after the first cycle of EBM job. The microstructure before and after the first cycle of production changes; yet a basketweave and intergranular structures are observed. The thickness of lamellae in virgin powders (0.75 ± 0.32 µm) shows a slight increase compared with that obtained after the first recycling (0.86 ± 0.27 µm); instead, semi-sintered top and bottom powders reveal thicker lamellae than previous cases. After EBM process an opaque grey layer appears at the surface of the particles and in figure 4.4 is marked with a red arrow; this layer corresponds to oxide, which is formed after the building when the powders were still rather hot and the chamber is opened to extract the building.It should be remembered that oxygen enhances the fragility of the material and reduce flowability. The oxidized layer thickness is approximately the same both in top and bottom sintered powders.

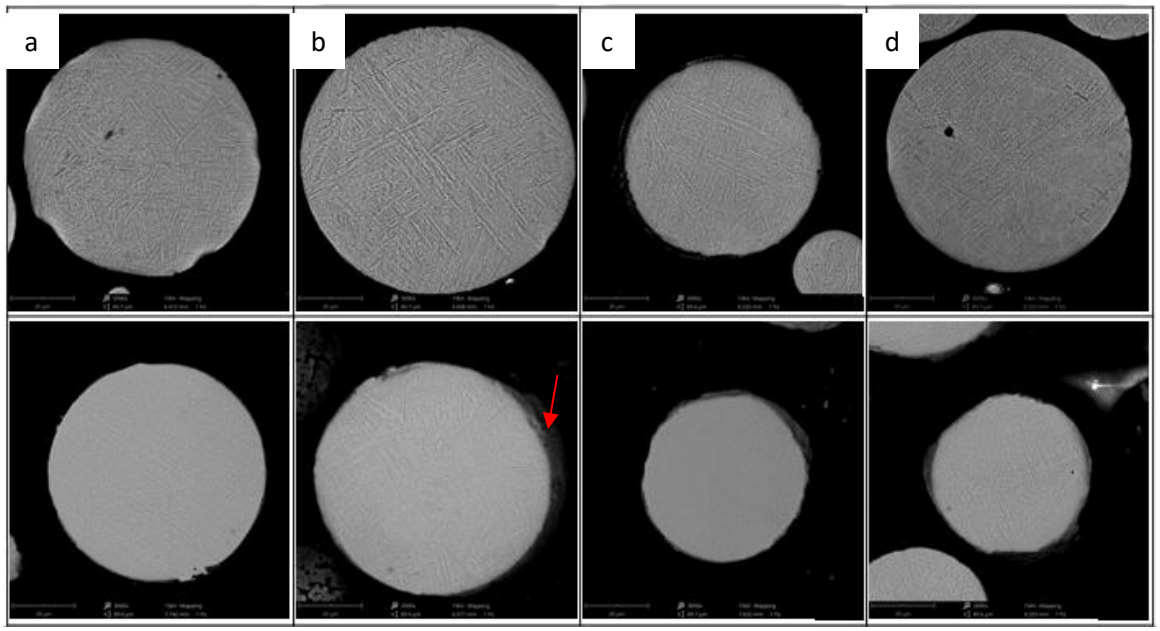

Figure 4.4: SEM images of microstructure and oxidized layers in (a) virgin, (b) top and (c) bottom sintered Ti-6Al-4V powders and (d) in powders after one cycle of PRS performed after the first cycle of EBM job.

In figure 4.5 magnified images of a particle after the recycling performed after the first cycle of EBM job is shown. In figure 4.5-b and c, the reference line where the chemical composition analysis was carried out is indicated. It results that the α' phase is rich in aluminium; indeed, Al belongs to the category of α-phase stabilizing elements, i.e. it moves the β-transus temperature up. Aluminium determined the nucleation and growth of those long and thick lamellae clearly observable in figure 4.5-b and c.

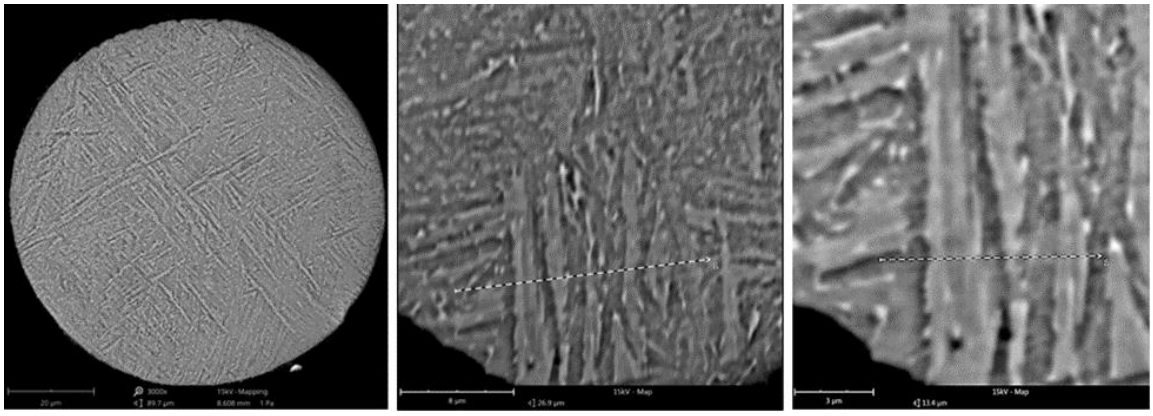

Figure 4.5: SEM images at different magnifications of a particle after the cycle of PRS performed after the first cycle of EBM job. The reference line for chemical composition analysis is also indicated.

Figure 4.6 represents a magnified image of the microstructure of another powder obtained after the cycle of PRS. Also, the area where the chemical composition analysis was carried out is shown. As can be seen in this Figure, the white-coloured phase characterized by an irregular shape is rich in vanadium which is a β-phase stabilizing element. This finding clearly proofs that the powder is subjected to a thermal treatment that results in a partial phase transition.

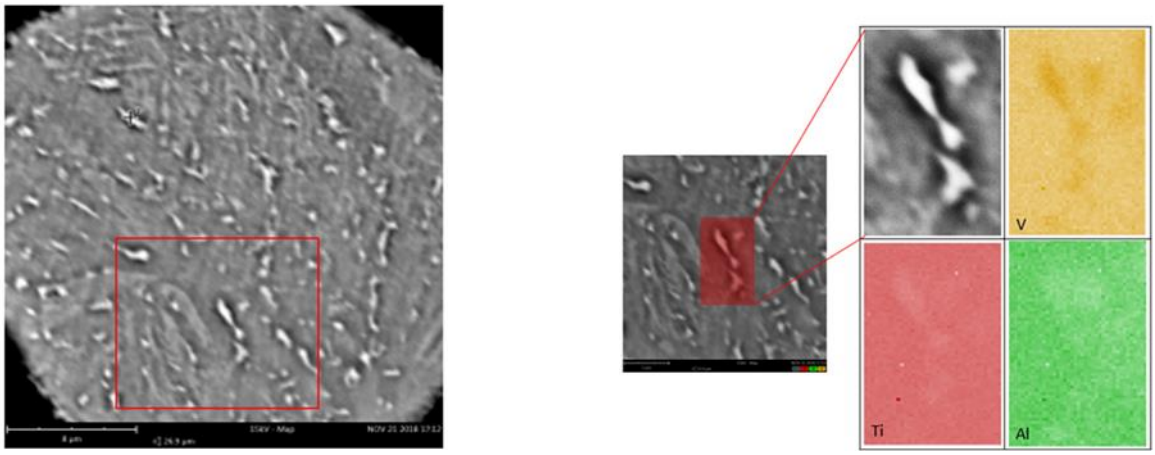

Figure 4.6: SEM-EDS analysis of a particle after the first recycling step (after PRS).

Figure 4.7 represents the SEM images of some Ti-6Al-4V particles obtained after the first recycling step (after PRS). Thereafter, the cross-section of powder was analysed via SEM to investigate the surface oxidation of the particles. As it is clearly observed in figure 4.7-b, the oxide thickness is not uniform and the mean value of this oxide layer is 3.02 ± 1.39 μm. The chemical composition of the oxide and surface layer of the particle was measured with SEM-EDS analysis and taken from the line drawn in figure 4.7-c. The results are shown in figure 4.7-d. As expected, the oxygen amount increases towards the topmost region of the oxide layer. Instead, titanium and vanadium profiles exhibit negligible variations of composition along the depth direction. Interestingly, the aluminium quantity decreases towards the oxide layer and, in correspondence of it, the quantity of aluminium itself doesn't vary anymore.

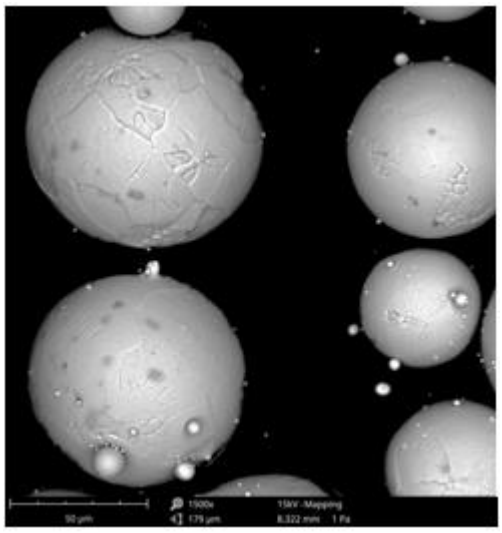

(a)

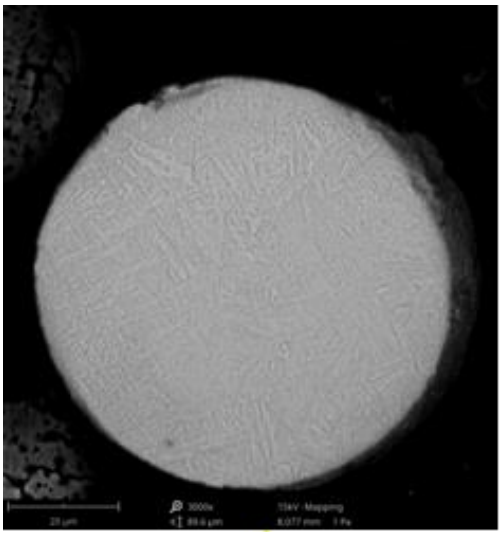

(b)

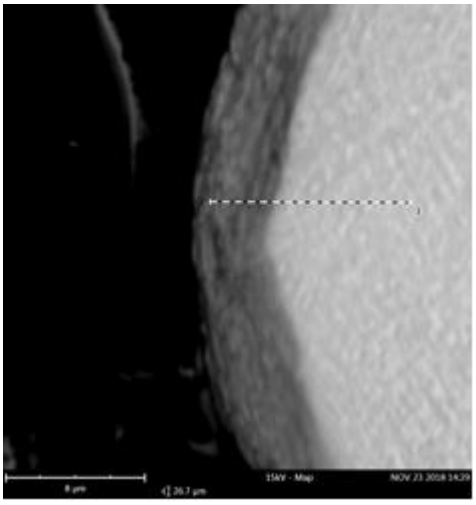

(c)

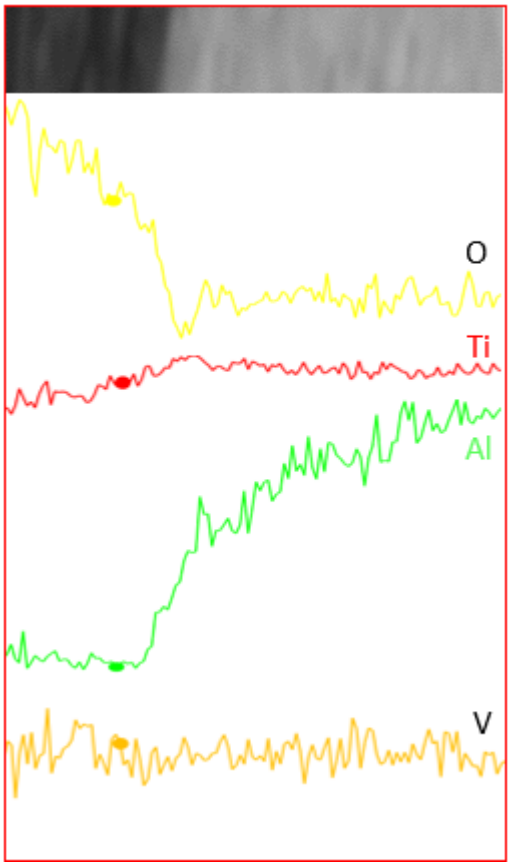

(d)

Figure 4.7: (a) SEM image of Ti-6Al-4V particles after one stage of PRS. (b) SEM image of a Ti-6Al-4V particle and its oxide layer developed after the first cycle of PRS, with (c) indication of the reference line for the EDS chemical composition analysis. (d) Chemical composition trends of the elements oxygen, titanium, aluminium and vanadium along the radial direction of the same particle.

The SEM-EDS examination of Ti-6Al-4V powders produced by gas atomization process and recovered by the PRS system doesn't reveal just the presence of titanium, aluminium and vanadium. Indeed, in correspondence of irregularities, visible on the surface of some particles, relevant presence of iron was detected (figure 4.8). This element represents clearly a contaminant and normally its amount is limited at a maximum of 0.3%. The effect of iron in titanium alloys is to stabilize β phase with the appearance of a eutectoid reaction in proximity of thermodynamic equilibrium conditions. It moves the $\beta \rightarrow \alpha$ transformation temperature down and may change the probability to find a specific microstructure in determined conditions of cooling. A secondary effect of iron on titanium alloys is to enhance the coagulation rate of intermetallic compound, that decreases the strength and increases the ductility of the material [27]. The probable sources of iron contamination could be from the "metallization" particles that probably fall down inside the building envelope and contaminated the powders. Contamination of iron could represent a serious problem in case of application of materials in biomedical fields because this element is not fully biocompatible.

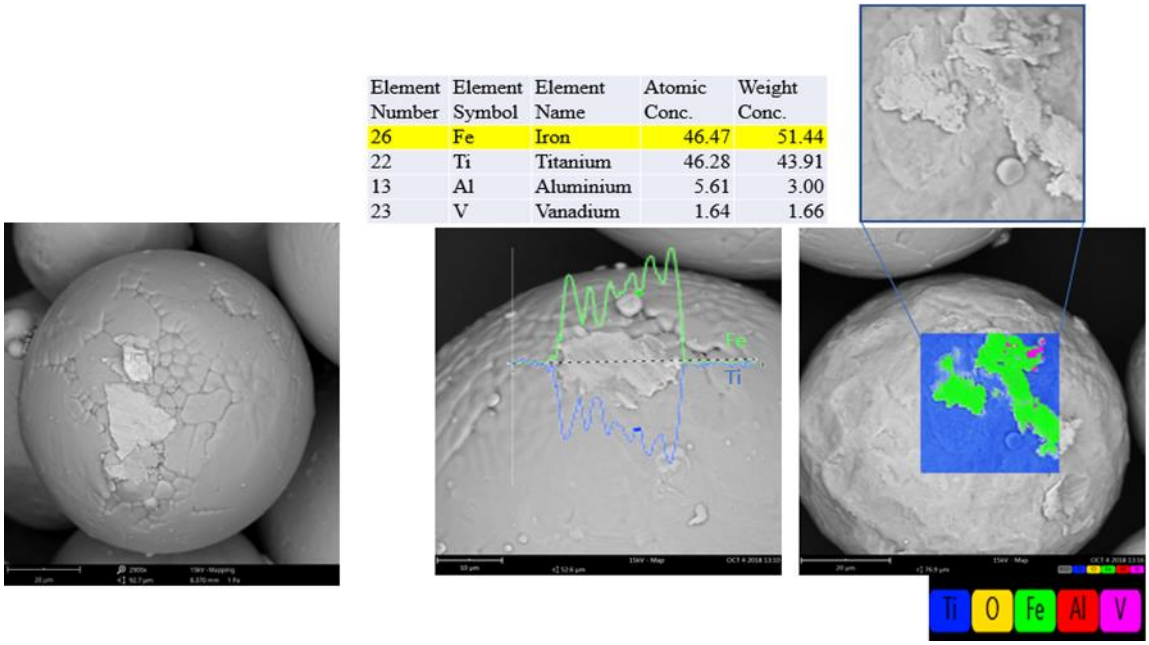

Figure 4.8: SEM images of Ti-6Al-4V particles after the first PRS cycle, containing some iron contaminants on their surface. The way EDS chemical composition analysis has been performed and their results are also reported.

Figure 4.9 reports in a histogram the EDS results relative to weight concentrations of titanium, aluminium and vanadium obtained in virgin, top and bottom sintered Ti-6Al-4V powders and obtained in the same material after one cycle of PRS. The weight concentration of oxygen has been analysed, but just in top and bottom sintered powders and powders after one cycle of PRS. The pick-up of oxygen gradually increases by the end of the recycling steps.

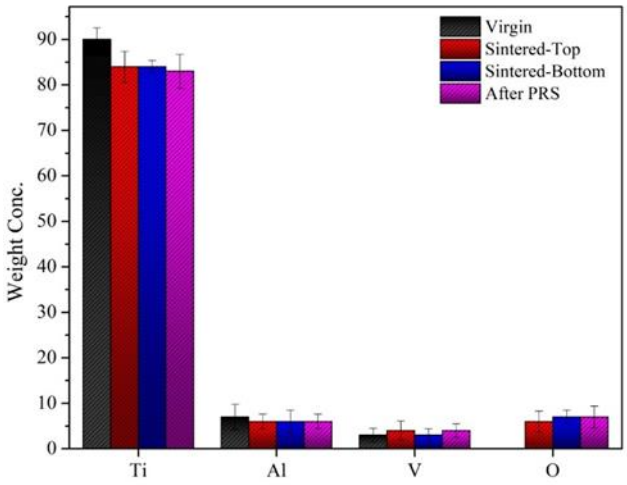

Figure 4.9: Chemical composition changes of Ti-6Al-4V powders during different stages of process (virgin state, sinter top, sinter bottom and after the first cycle of PRS).

Figure 4.10 reports the results of XRD analysis, both in diffractogram and in chart form, of the virgin and sintered powders of Ti-6Al-4V and the same alloy after one cycle of PRS. All peaks are related to the α phase (HCP); the most important one corresponds to an angle $2\theta \approx 40°$ and it has been used to calculate the average crystal size with Scherrer's formula:

$$\tau = \frac{K\lambda}{\beta \cos\theta} \tag{4.1}$$

where τ corresponds to the average size of grains, K is a shape factor near unity (the most used value is 0.9), λ is the x-ray wavelength incident on the sample, β is the full width at half maximum (FWHM), θ is Bragg's angle. The peak after the EBM process has become taller and narrower than the one related to virgin material. The results demonstrate a crystal coarsening after EBM process. A slight decrease of crystallinity is verified in powders subjected to one cycle of PRS with respect to those taken just after EBM process.

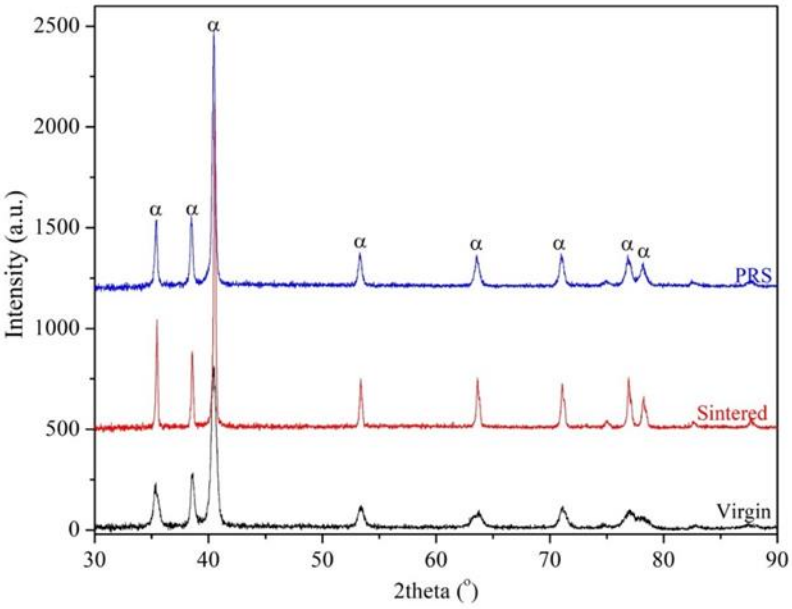

(a)

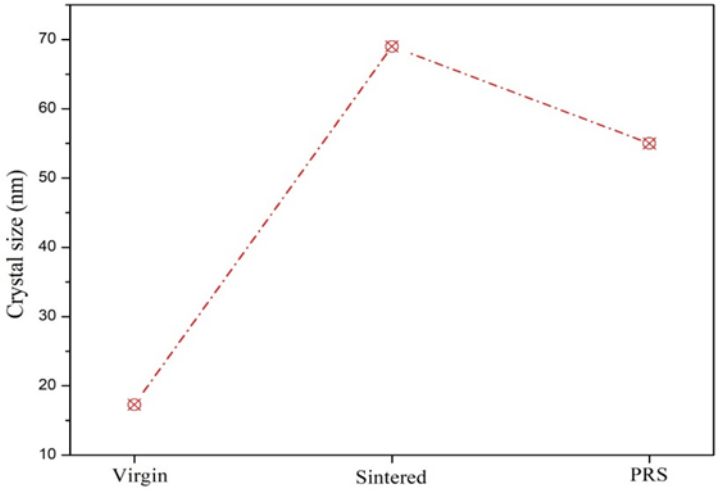

(b)

Figure 4.10: (a) XRD resulting from virgin, sintered and after PRS Ti-6Al-4V powders and the consequent average crystal size plot (b).

4.1.2 Second cycle of production process

Figure 4.11 illustrates the particle size distribution (PSD) of both the Ti-6Al-4V powders recovered after the cycle of PRS performed after the first cycle of EBM job (designated here as "hopper") and recovered after the second EBM job. The PSD has been reported in the form of histogram. Besides, for each kind of powders, respective flowability measurements have been reported. From PSD results it is possible to observe that quite no change of median size

occurred (≈ 60 µm); however, the fraction of particles smaller than this median size diminishes in powders obtained after the cycle of PRS performed after the second cycle of EBM job and, oppositely, the fraction of particles bigger than the median size increases because sintering phenomena taking place during the second cycle of EBM process eliminated most of the small particles. Besides, the number of satellites diminishes during the time between the first cycle of EBM and the stage of PRS performed after the second cycle of EBM job. However, as it is mentioned it is found that the quantity of the larger particle increases that is as a consequence of the presence of partially melted particles or joining the particle to each other via splashing the melt drops from the melt pool and accordingly leads to the decreasing of flowability.

Cycle2

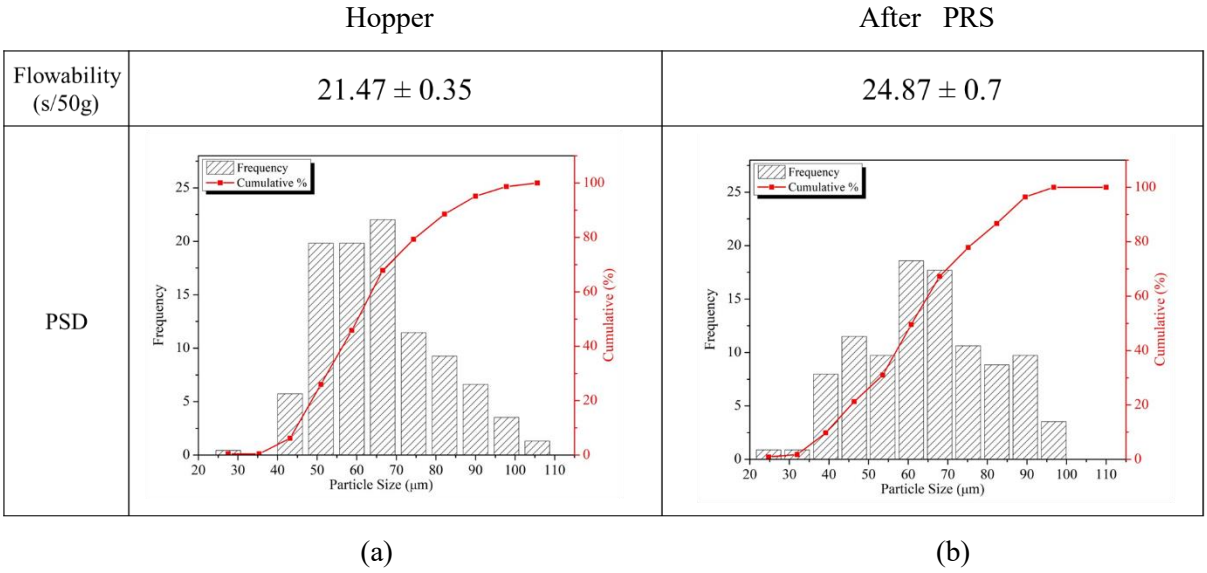

Figure 4.11: Comparison of the flowability between (a) "hopper" powders and (b) after the stage of PRS performed after the second cycle of EBM job.

Figure 4.12 reports SEM images (at 500x and 3000x magnifications) of Ti-6Al-4V powders obtained after one cycle of PRS ("hopper") performed after the first cycle of EBM job, top and bottom sintered powders after the second stage of EBM process and after the second cycle of PRS performed after the second cycle of EBM job. The number of satellites diminishes gradually with another cycle of EBM process and of PRS, in comparison with the case of powders after just one stage of PRS after the first cycle of EBM job. A decrease of flowability after the stage of PRS occurred. Indeed, the shape of powders after the second cycle of the EBM process and next than the stage of PRS performed after the second cycle of EBM job became less rounded. The small flat areas observed on the surface of particles represented in figure 4.12 could be the cross-section of necks that have formed during the preheating step (sintering necks). One of these areas is indicated in red in figure 4.12.

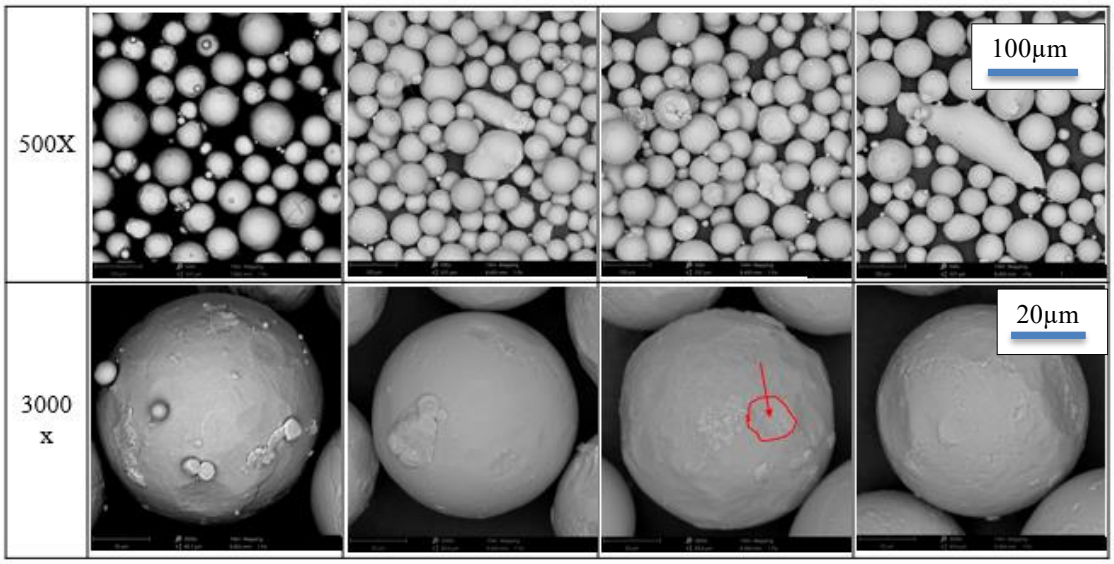

(a) (b) (c) (d)

Figure 4.12: Morphological illustration of (a) "hopper" powder samples, (b) top and (c) bottom sintered powders and (d) after PRS during second cycle of production with magnifications of 500x and 3000x.

Figure 4.13 reports optical microscopy images of Ti-6Al-4V powders after the stage of PRS performed after the first cycle of EBM job ("hopper"), top and bottom sintered obtained after the second cycle of the EBM process and after the PRS performed after the second cycle of EBM job. The upper micrographs are related to not-etched powders and still reveal the presence of porosity within some particles. Unfortunately these pores, arising from the production of Ti-6Al-4V powders by gas atomization processes. Instead, the bottom micrographs were taken from powders etched with Kroll's solution, in order to reveal their microstructure. No relevant changes of structure are observed; all the materials contain the α phase embedded in β phase. Anyway, the microstructure of powders after the second cycle of EBM process and after the stage of PRS after the second cycle of EBM job is coarser than powders after just one stage of PRS after the first cycle of EBM job; this may be explained by the fact that the heating during the EBM process that leads to the microstructure coarsening.

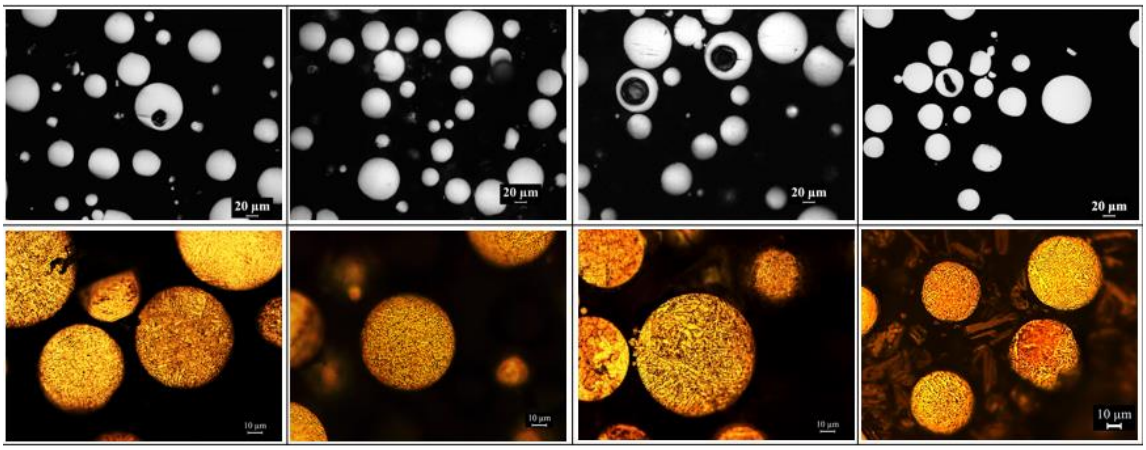

(a) (b) (c) (d)

Figure 4.13: Optical images of (a) "hopper" powder samples, (b) top, (c) bottom sintered powders and (d) after PRS during the second cycle of production in the states of un-etched (above) and etched samples (down) with magnifications of 100x and 200x, respectively.

Figure 4.14 reports SEM images of powders after one stage of PRS performed after the first cycle of EBM job ("hopper"), after two cycles of EBM processes and after the stage of PRS performed after the second cycle of EBM job. All micrographs have been taken at magnification 3000x, but upper ones are related to particles not covered by the oxide layer, while bottom ones are partially covered by oxide layer. Also microstructure is visible and, after the stage of PRS after the second cycle of EBM job, allotriomorphic α phase appeared in few particles. The α lath spacing within grains after the stage of PRS after the second cycle of EBM job (0.97 ± 0.21 µm) increased with respect to what can be observed after the stage of PRS performed after the first cycle of EBM job. The oxide layer in all materials is not uniform, similarly to what happened until the cycle of PRS performed after the first cycle of EBM job. Anyway, the surface zones covered by oxide layer increased gradually after two cycles of EBM processes and after the stage of PRS after the second cycle of EBM job; besides, the oxide thickness became more uniform than what is observed after just one stage of PRS.

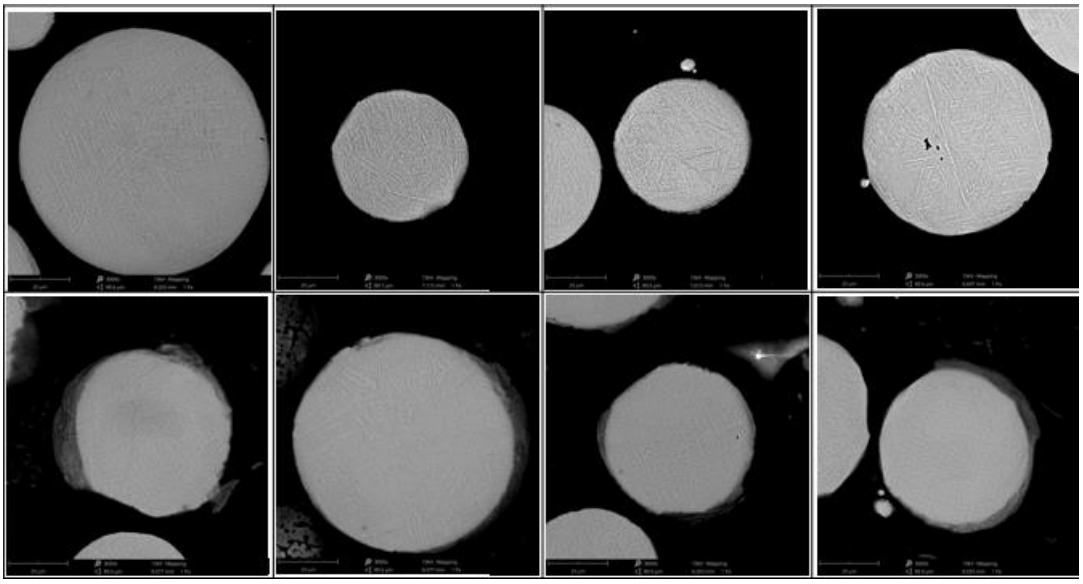

(a) (b) (c) (d)

Figure 4.14: SEM images of microstructure and oxidized layers in (a) “hopper”, (b) top and (c) bottom sintered Ti-6Al-4V powders and (d) in powders after the cycle of PRS performed after the second cycle of EBM job.

Figure 4.15-a shows an SEM image of another particle subjected to the stage of PRS performed after the second cycle of EBM job and the line (figure 4.15-b) where the chemical composition has been evaluated by SEM-EDS technique. The relative amount profiles of the elements titanium, aluminium and vanadium have been reported in figure 4.15-c in correspondence of each point of the reference line. The EDS-line analysis confirms that the needles are rich in Al.

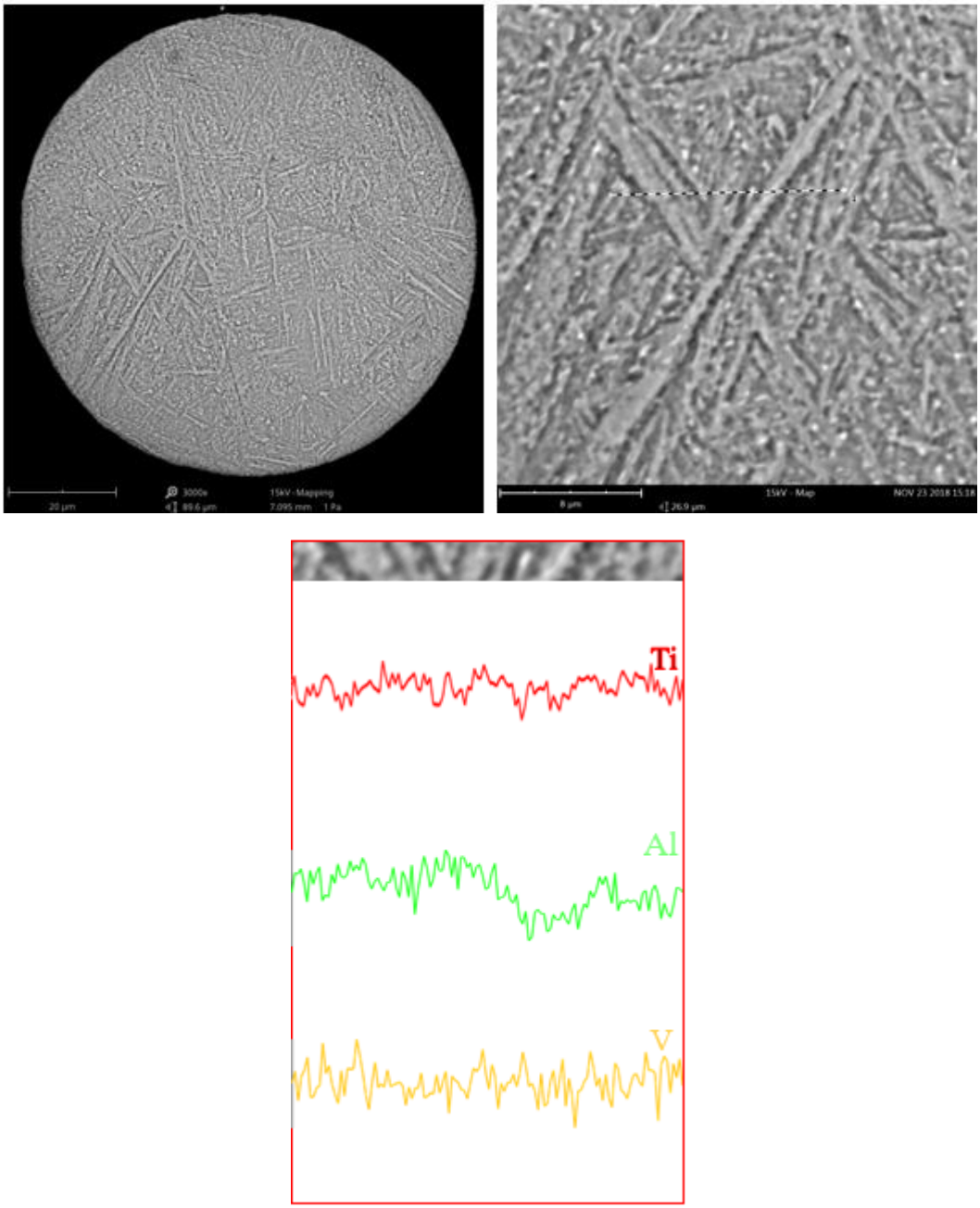

Figure 4.15: SEM-EDS linear analysis within a particle after the cycle of PRS performed after the second cycle of EBM job.

Figure 4.16-a reports an SEM image reproducing a particle among powders subjected to the stage of PRS performed after the second cycle of EBM job where β phase is particularly evident, with indicated the area where the map composition has been performed. Indeed, as represented in figure 4.16-b, the white phases correspond to largest contrast of yellow (composition map relative to vanadium). Furthermore, a gas pore is evident within the same particle.

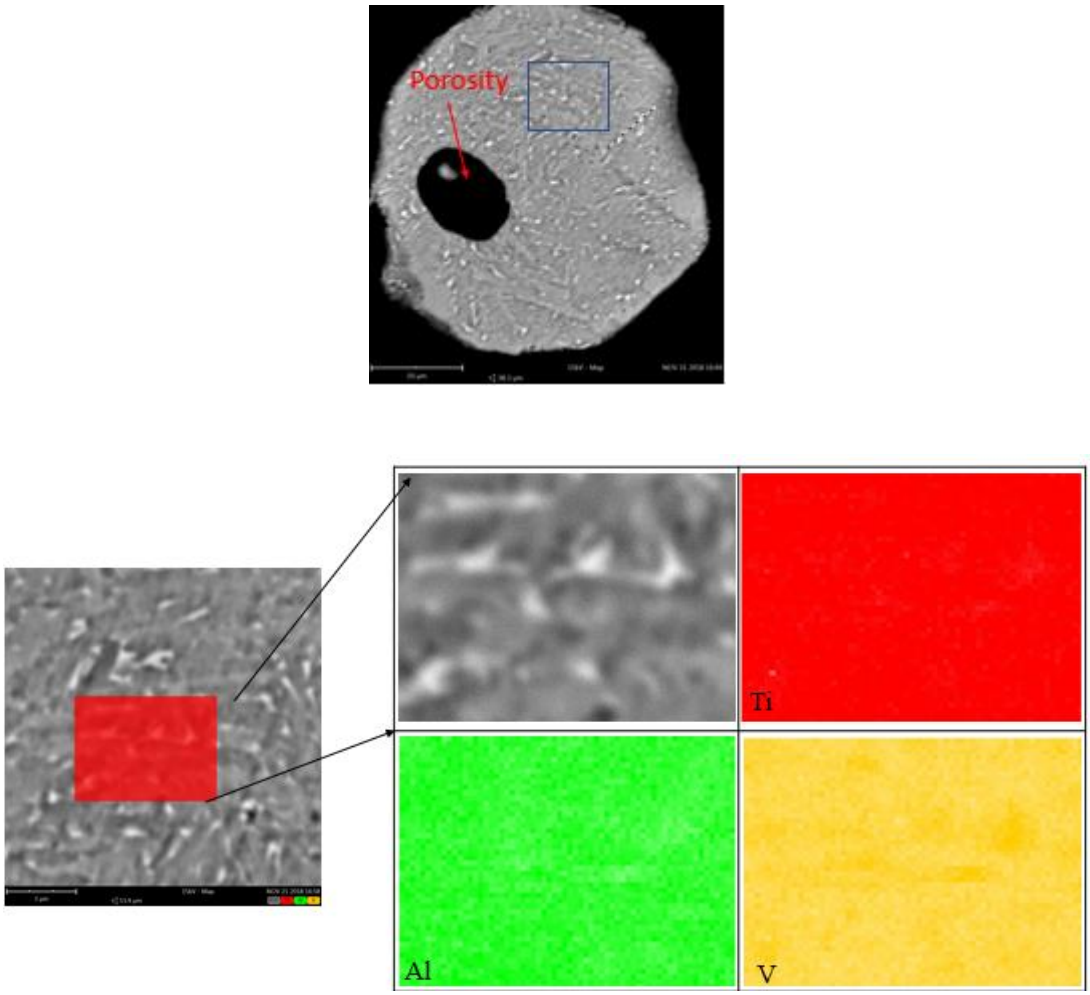

Figure 4.16: SEM-EDS analysis of a particle after the cycle of PRS performed after the second cycle of EBM job, where β phase is revealed.

Figure 4.17 represents SEM images of the powders after the stage of PRS performed after the second cycle of EBM job that show the presence of non-uniform oxide layers. The mean oxide layer thickness is 3.48 ± 0.95 μm, quite similar to that measured after the stage of PRS after the first cycle of EBM job. In the proximity of the surface of one particle, that corresponds to the interface between particle and oxide layer, has been drawn a line where the chemical composition has been evaluated. The relative amounts of the elements oxygen, titanium, aluminium and vanadium were reported for each point of the reference line. No change of titanium and vanadium are detected, while an increase of oxygen obviously occurs beyond the interface and within the oxide layer. The trend exhibited by aluminium profile is noteworthy. It is possible to observe a slight decrease in its amount in correspondence of the interface.

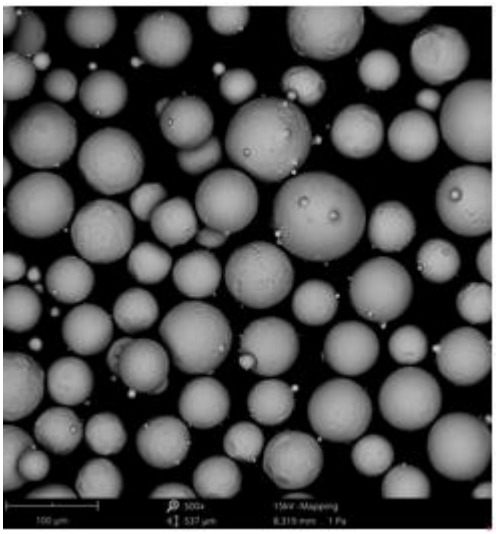

(a)

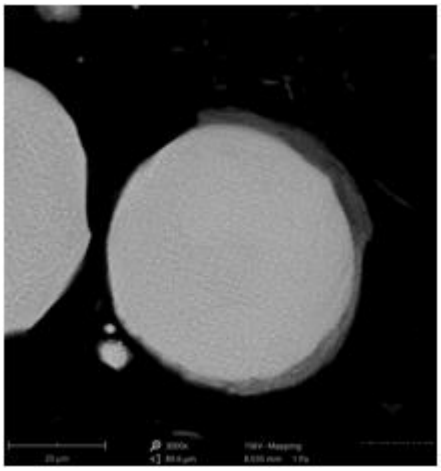

(b)

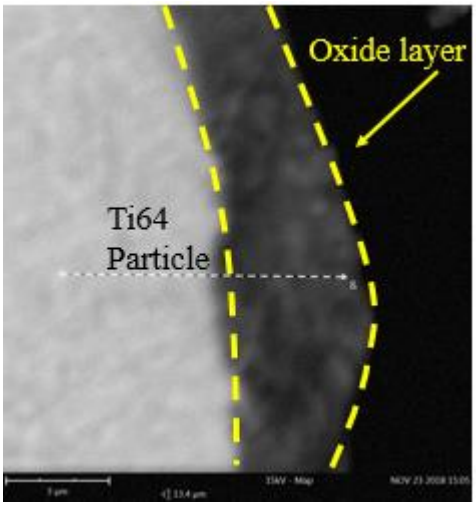

(c)

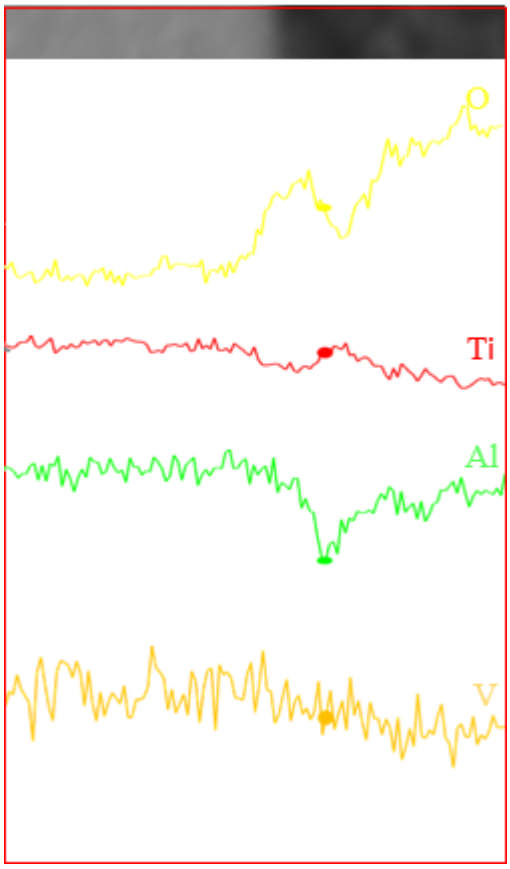

(d)

Figure 4.17: (a) SEM image of Ti-6Al-4V particles after the stage of PRS performed after the second cycle of EBM job. (b) SEM image of a Ti-6Al-4V particle and its oxide layer after the cycle of PRS after the second cycle of EBM job, with (c) indication of the reference line for the EDS chemical composition analysis. (d) Chemical composition trends of the elements oxygen, titanium, aluminium and vanadium along the radial direction of the same particle.

Figure 4.18 represents SEM images of a particle after the stage of PRS performed after the second cycle of EBM job containing some contamination (of iron) on its surface. To investigate the chemical composition of this zone, a line composition analysis has been performed. The composition profiles have been obtained, and the overall atomic and weight concentrations were reported on table. Indeed, as revealed by the colour mapping, just few green-coloured regions, corresponding to iron, are surrounded by the blue ones, corresponding to titanium. In correspondence of some "steps", the aluminium content alternatively increases and diminishes; by keeping in mind that superficial aluminium is associated with oxygen, part of contamination is related to oxide layers viewed from another point of observation.

Element Number	Element Symbol	Element Name	Atomic Conc.	Weight Conc.
22	Ti	Titanium	86.09	87.67
26	Fe	Iron	3.85	4.57
23	V	Vanadium	3.89	4.21
13	Al	Aluminium	6.17	3.54

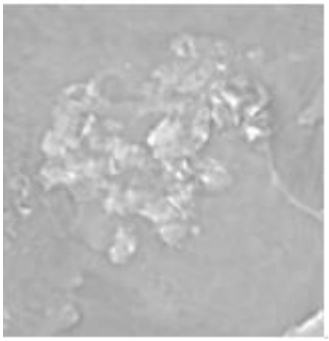

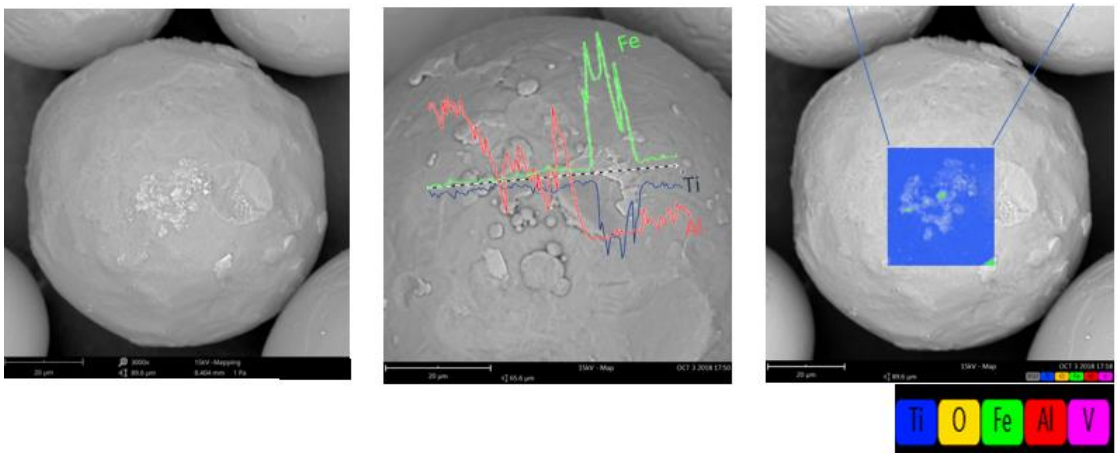

Figure 4.18: SEM images of Ti-6Al-4V particles after the PRS cycle performed after the second cycle of EBM job, containing some iron contaminants on their surface. The way EDS chemical composition analysis has been performed, and their results are also reported.

4.1.3 n cycle of the production process

Similarly to the comparison of powders taken after the cycles of PRS performed after the first and the second cycle of EBM job, the flowability of Ti-6Al-4V powders after the stage of PRS performed after the n^{th} cycle of EBM job (flowing time = 25.78 ± 1.23) decreased with respect to those after the cycle of PRS after the second cycle of EBM job (flowing time =

23.87 ± 0.7), in this case designated as “hopper”, may be due to further increase of the fraction of bigger particles to the detriment of the fraction of smaller ones (figure 4.19). Although the shape of particles became gradually more irregular, the oxide layer covered most of surface regions, and its uniformity enhances, thus leading to a reduction of flowability.

Cycle n

	Hopper	After PRS
Flowability (s/50g)	25.68 ± 0.5	25.78 ± 1.23
PSD	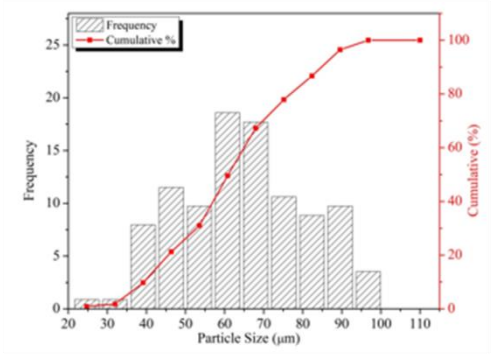	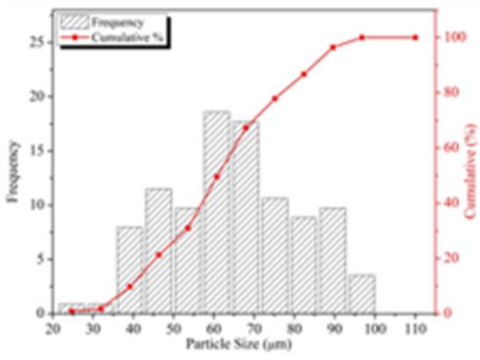

(a) (b)

Figure 4.19: Comparison of the flowability between (a) “hopper” powders and (b) after the stage of PRS performed after the n^{th} cycle of EBM job.

A confirmation of these results arises from the observation of SEM images at 500x and 3000x magnification (figure 4.20), representing Ti-6Al-4V powders after the stage of PRS performed after the second cycle of EBM job (“hopper”), after the n^{th} cycle of EBM processes and after the stage of PRS after the n^{th} cycle of EBM job. Along with the reduction of the number of satellites, all powders observed at higher magnification contain some iron contaminants on their surface. It is quite difficult to understand which cycle of EBM or PRS stage has introduced such contamination.

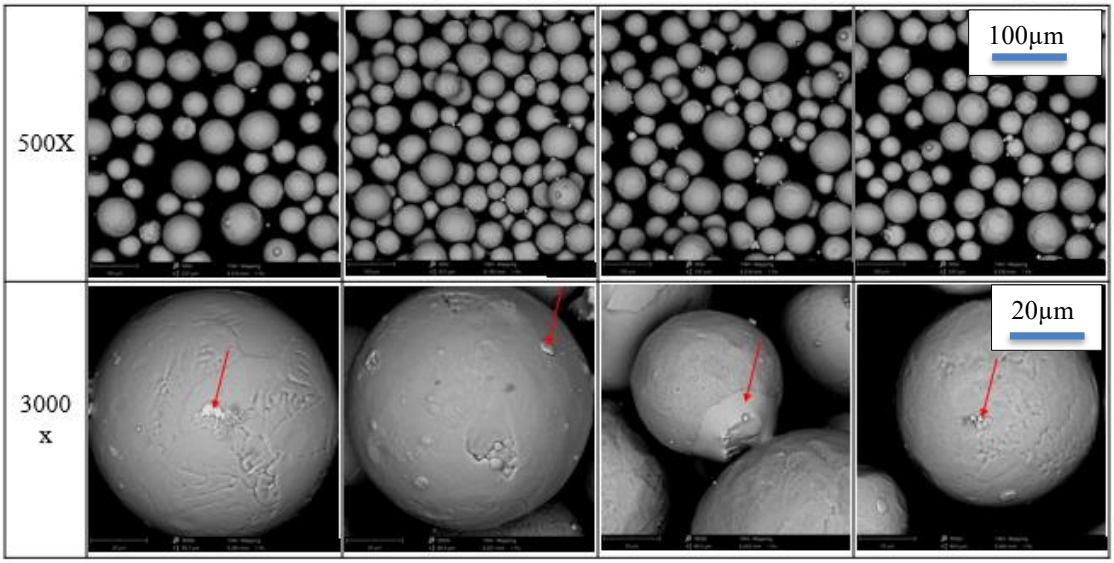

(a) (b) (c) (d)

Figure 4.20: Morphological illustration of (a) "hopper" powder samples, (b) top and (c) bottom sintered powders and (d) after PRS during the n^{th} cycle of production with magnifications of 500 x and 3000 x.

Figure 4.21 reports optical microscopy images representing the shape and the microstructure of Ti-6Al-4V powders after the stage of PRS performed after the n^{th} cycle of EBM job ("hopper"). The above images are related to not-etched particles; gas pores arising from powder manufacturing processes are still visible in few particles. The bottom images, instead, are related to particles etched with Kroll's solution, in order to reveal their microstructure. From the stage of PRS after the second cycle of EBM job to the stage of PRS after the n^{th} cycle of EBM job, passing through the n^{th} cycle of the EBM process, the microstructure became gradually coarser.

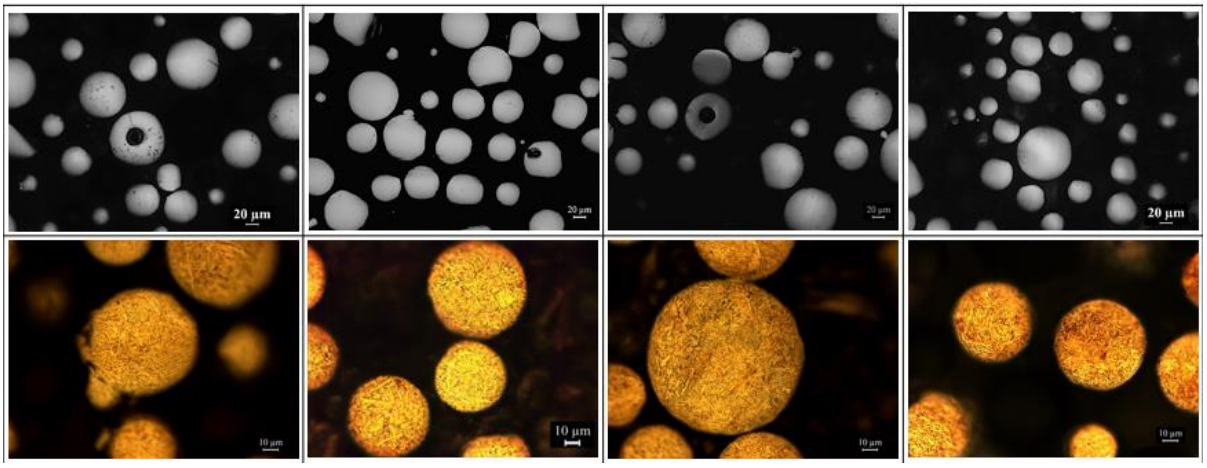

(a) (b) (c) (d)

Figure 4.21: Optical images of (a) "hopper" powder samples, (b) top, (c) bottom sintered powders and (d) after PRS during the n^{th} cycle of production in the states of un-etched (above) and etched samples (down) with magnifications of 100x and 200x, respectively.

Figure 4.22 shows SEM micrographs of Ti-6Al-4V powders after the stage of PRS performed after the second cycle of EBM job ("hopper"), after the n^{th} cycle of the EBM process and after the stage of PRS performed after the n^{th} cycle of EBM job. In this last case, some protruding structures that grew essentially along one direction are clearly visible. These may correspond to the α phase laths; their average spacing is 1.21 ± 0.18 µm. The oxide layers, after the stage of PRS after the n^{th} cycle of EBM job, became more uniform and covered quite all the surface regions of the particles.

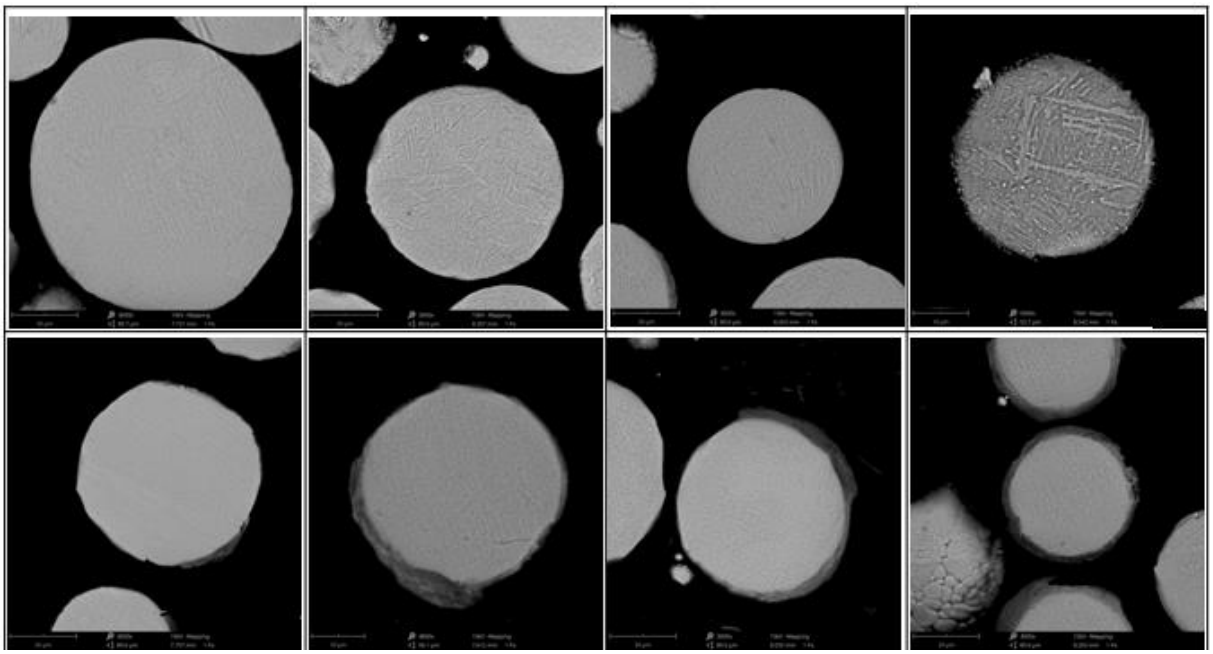

(a) (b) (c) (d)

Figure 4.22: SEM images of microstructure and oxidized layers in (a) “hopper”, (b) top and (c) bottom sintered Ti-6Al-4V powders and (d) in powders after the cycle of PRS performed after the n^{th} cycle of EBM job.

Figure 4.23-a shows an SEM image of a Ti-6Al-4V particle after the stage of PRS performed after the n^{th} cycle of EBM job, where a chemical composition analysis has been performed along the line drawn in figure 4.23-b. As demonstrated by the relative amount profile of the elements titanium, aluminium and vanadium, there’s a slight increase of aluminium content in correspondence of the lath structure. This means that, probably, the lath structure corresponds to an α phase region.

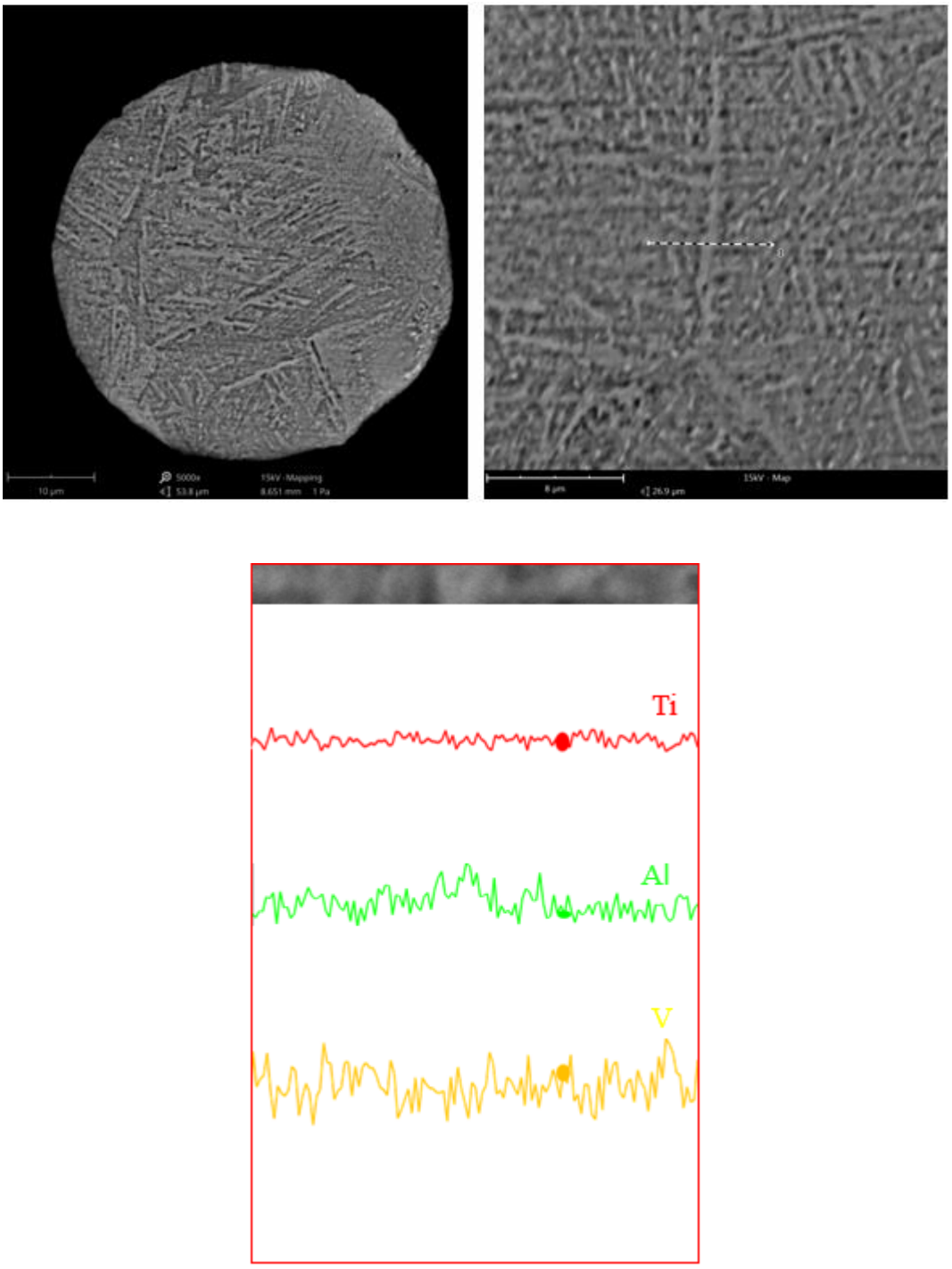

Figure 4.23: SEM-EDS linear analysis within a particle after the cycle of PRS performed after the n^{th} cycle of EBM job.

A confirmation of the previous result is shown in figure 4.24, which represents an SEM image of another Ti-6Al-4V particle after the stage of PRS performed after the n^{th} cycle of EBM job. As demonstrated by the map composition of titanium, aluminium and vanadium, is

visible a bigger contrast of green colour (corresponding to the aluminium) in proximity of the protruding structure.

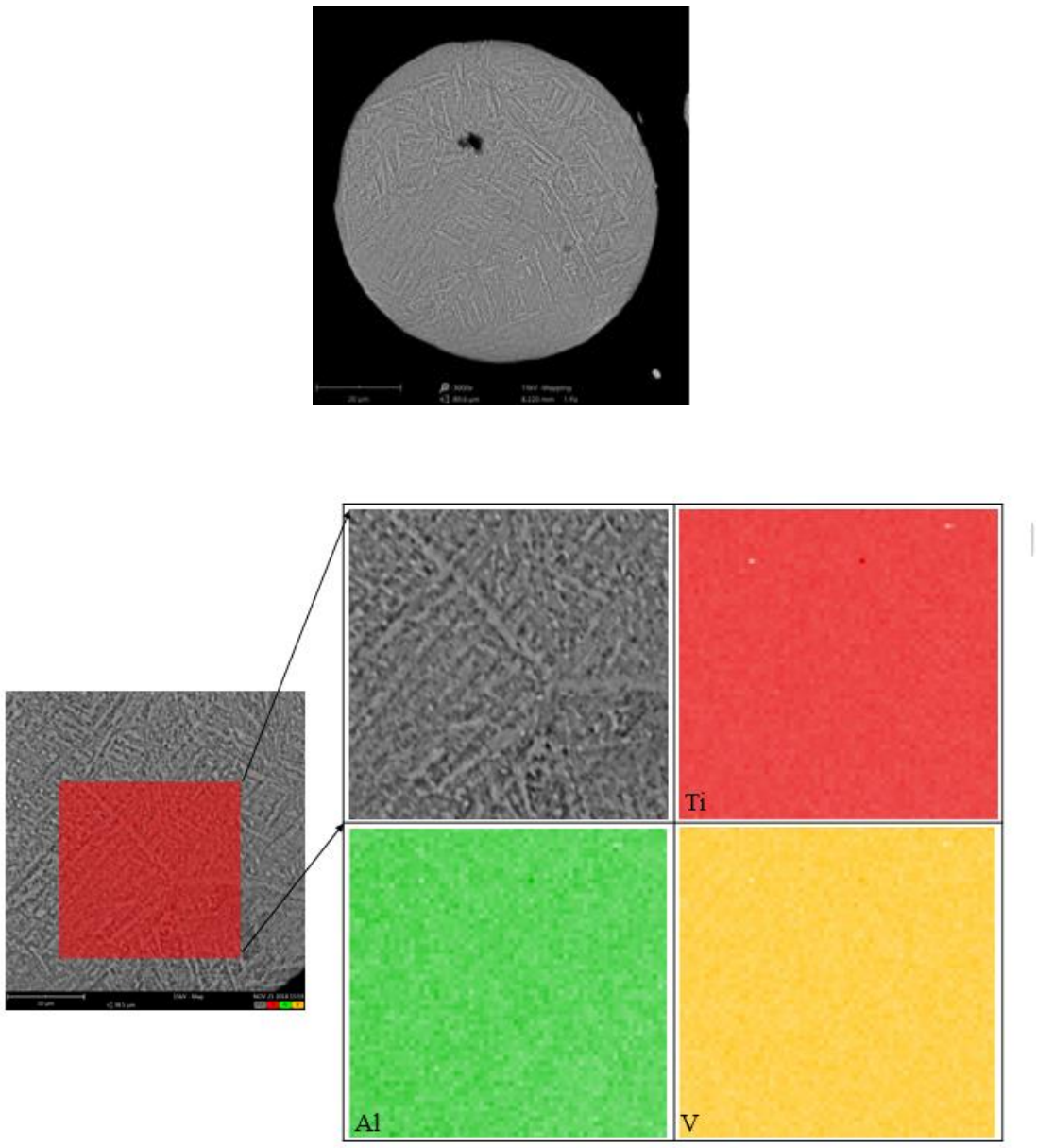

Figure 4.24: SEM-EDS analysis of a particle after the cycle of PRS performed after the n^{th} cycle of EBM job.

Figure 4.25 represents the SEM images of Ti-6Al-4V powders after the stage of PRS performed after the n^{th} cycle of EBM job and the line drawn for the chemical composition analysis in the surface region and the oxide layer in a selected particle. The oxide layer covers most of the particles and these layers correspond to the titanium oxide and its thickness is quite the same as that measured in previous cycles (3.18 ± 0.45 μm).

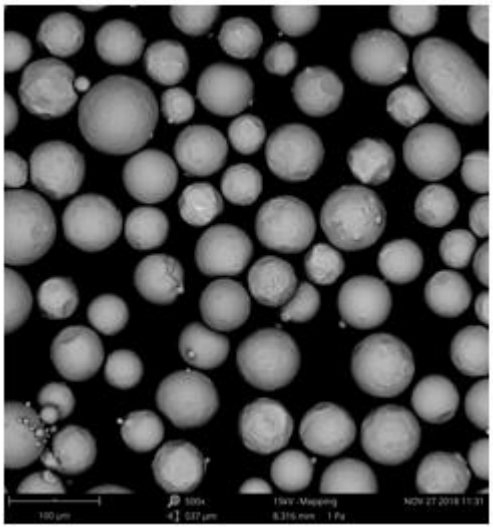

(a)

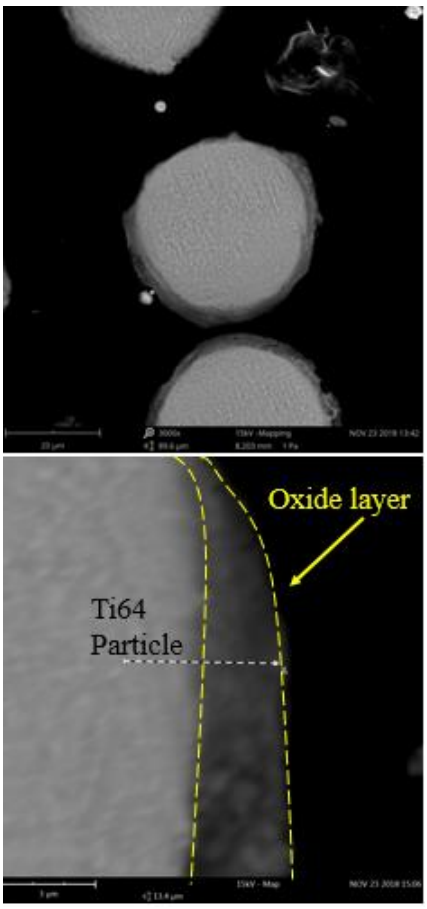

(b)

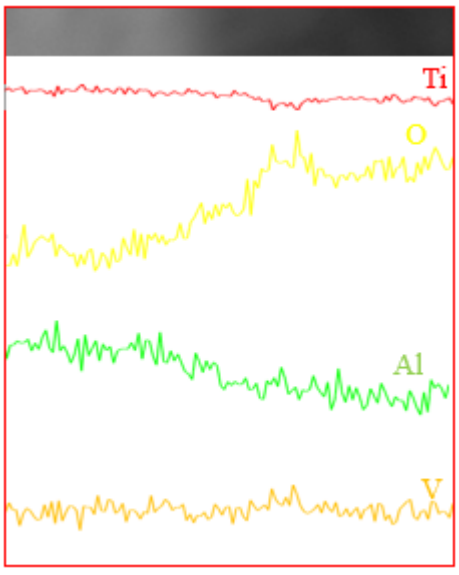

(c)

Figure 4.25: (a) SEM image of Ti-6Al-4V particles after the stage of PRS performed after the n^{th} cycle of EBM job. (b) SEM image of a Ti-6Al-4V particle and its oxide layer after the cycle of PRS

performed after the n^{th} cycle of EBM job, with (c) indication of the reference line for the EDS chemical composition analysis. (d) Chemical composition trends of the elements oxygen, titanium, aluminium and vanadium along the radial direction of the same particle.

Figure 4.26 represents the SEM images of a sintering neck occurred between Ti-6Al-4V during the EBM process. Directly on the neck and in the nearest zones chemical composition analysis has been performed. The contamination zone isn't just restricted on the particle surface, but also along the junction zones between two particles. Here, for example, the neck represented in figure 4.26 is rich in iron and oxygen while, locally, the concentration of titanium and vanadium diminishes. This neck formation is the result of iron contamination that was present during the melting process and melted and joined two particles.

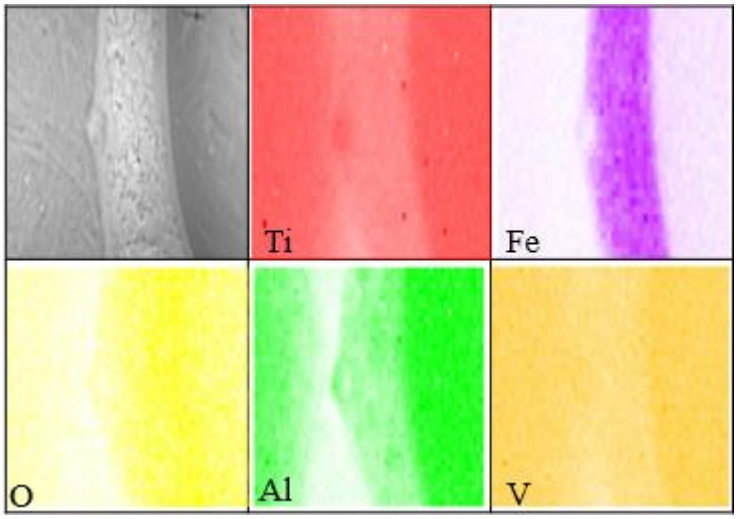

(a)

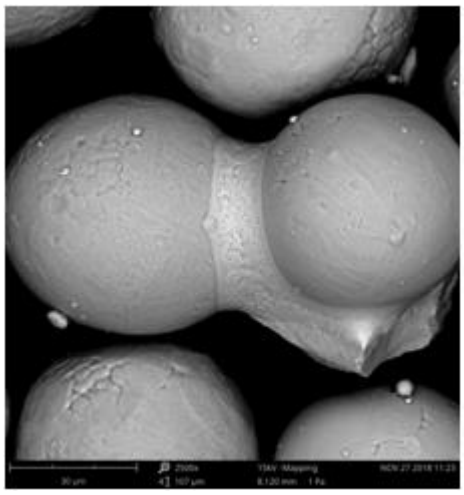

(b)

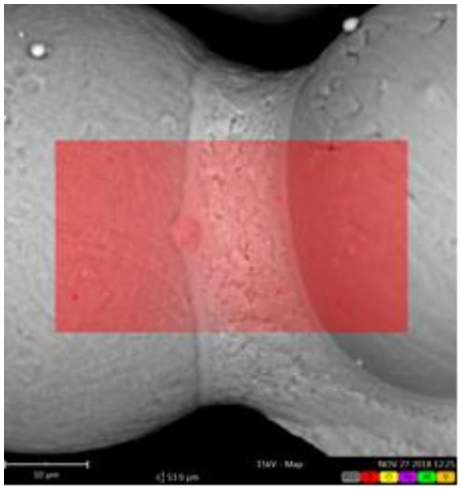

(c)

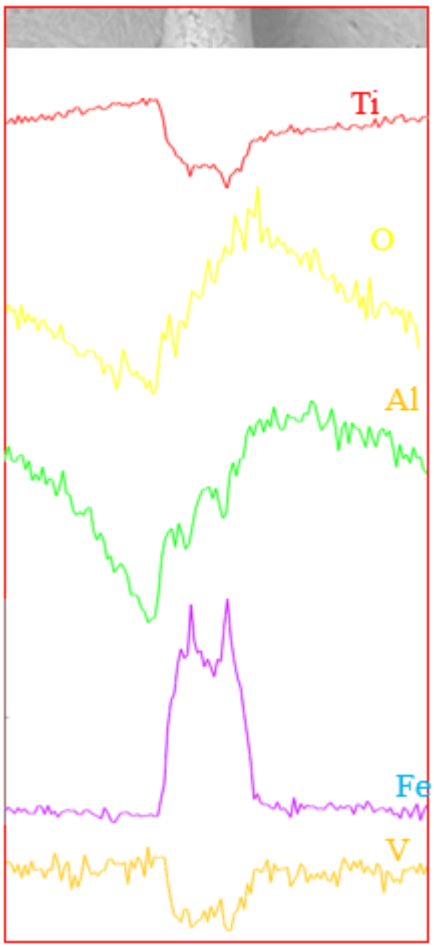

(d)

Figure 4.26: (a) SEM-EDS analysis of a sintering neck between two Ti-6Al-4V particles after the stage of PRS performed after the n^{th} cycle of EBM job. (b) SEM image of Ti-6Al-4V particles connected by a sintering neck and the formed oxide layer after the cycle of PRS performed after the n^{th} cycle of EBM job, with (c) indication of the reference area for the EDS chemical composition analysis. (d) Chemical composition trends of the elements oxygen, titanium, aluminium, iron and vanadium along the radial direction of the same particle.

4.2 Microstructural analysis of Ti-6Al-4V bars produced by EBM

Four bar-shaped samples, with their sizes indicated in figure 4.28, have been produced within the EBM machine in four different positions on the base plate, according to figure 4.27-c. Production of all the massive samples described in this section was carried out with the standard parameters that were provided by Arcam. Subsequently, they have been sectioned longitudinally. Figure 4.27-a shows optical microscopy images of pore distributions of the four Ti-6Al-4V bars. The average values are reported in chart in figure 4.27-b. From optical images it is possible to observe the presence of gas porosity in some parts of all EBM-built bars; also, some smaller pores are distributed all over the entire sections. The porosity evaluation of bulk samples produced at different positions on the start plate showed that the porosity content of these samples are equal and independent from the position of sample.

The overall porosities are also reported on histograms: sample 3 is characterized by the maximum level of porosity, followed by sample 1, 2 and 4. Indeed, sample 3 contains pores with very small sizes, but homogeneously distributed all over the built part.

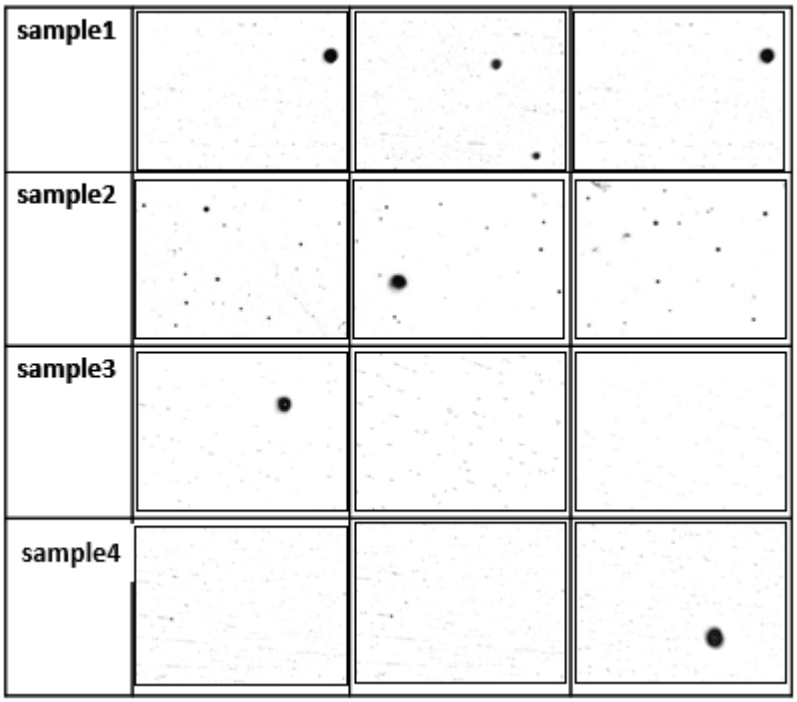

(a)

	Average porosity ± standard deviation (%)
Sample 1	0.55 ± 0.46
Sample 2	0.51 ± 0.57
Sample 3	0.74 ± 0.3
Sample 4	0.44 ± 0.23
Overall	0.56 ± 0.13

(b)

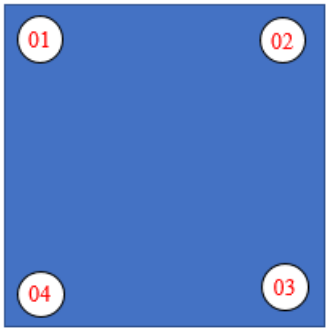

(c)

Figure 4.27: (a) Optical microscopy images of pore distributions in four Ti-6Al-4V EBM-produced bars. (b) Results of porosity measurement. (c) Arrangement of the four samples.

The EBM-built Ti-6Al-4V bars sectioned longitudinally were mirror polished to study the microstructure at the optical microscope. As pointed out in figure 4.28, some zones contain colony α structures and other ones are characterized by the presence of Widmanstätten basketweave α structure. Besides, the microstructure at the topmost regions are finer than central ones.

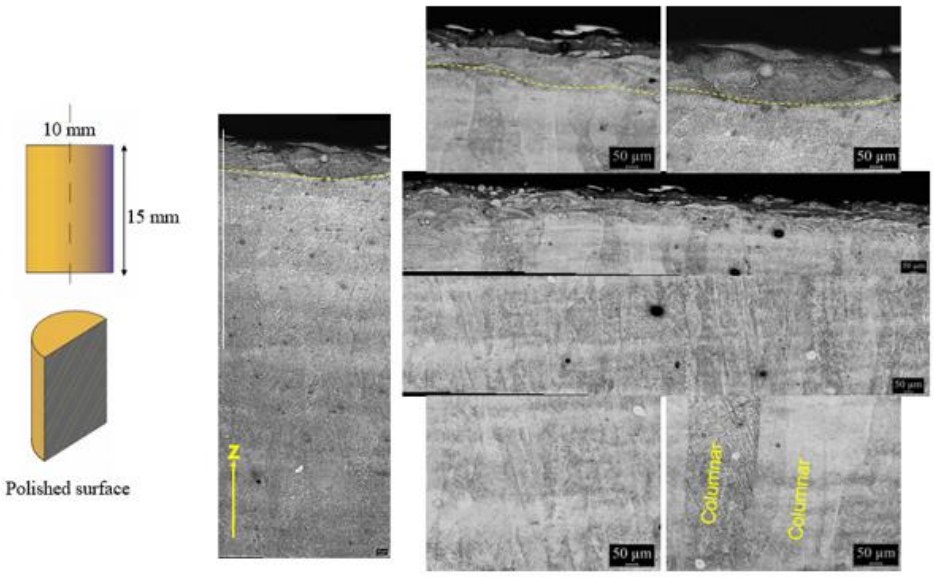

(a) (b)

Figure 4.28: (a) Sizes of the four EBM produced bars with an indication of the section plane. (b) Optical microscopy images of parts of one of the EBM produced bars.

Figure 4.29-a represents the chemical composition map obtained at the interface between the base plate and the component to be produced. The relative amount of iron, nickel and chromium are related to different tonalities of red, purple and green, respectively. Instead, figure 4.29-b represents a line elemental composition executed in the same region. The relative amount of iron, nickel, chromium and vanadium are associated with different colours. Through the information obtained from both figure 4.29-a and b, it is possible to state that diffusion of iron, nickel and chromium from the start plate to the Ti64 sample reaches a depth of less than 200 µm.

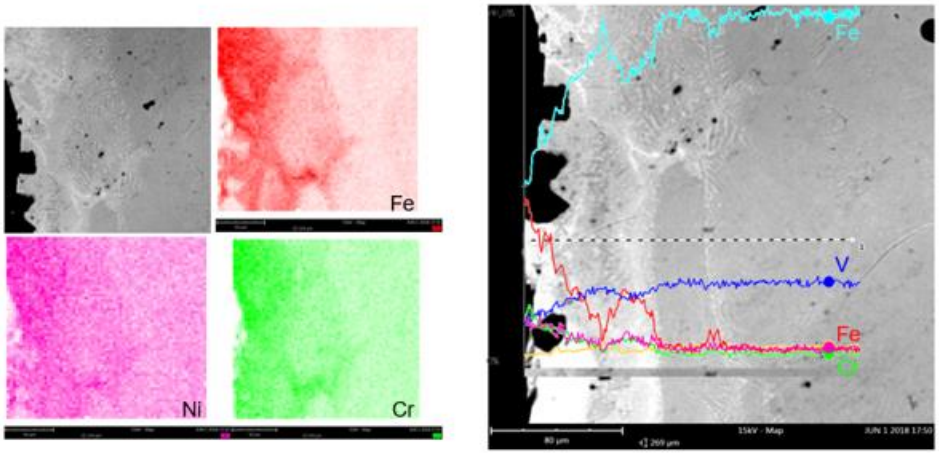

(a) (b)

Figure 4.29: (a) SEM-EDS chemical composition map in correspondence of surface component. (b) SEM-EDS chemical composition analysis performed on the drawn line.

In order to investigate either the variations of microstructure and the porosity distribution in different parts of the EBM manufactured bar, some sections have been taken according to the ways represented in figure 4.30; here are reported also the sizes of both the entire produced bar and of the sectioned samples. The microstructure of these samples was investigated by observing them either at the optical and the scanning electron microscope. The three different sections are called “top”, “middle” and “near bottom”.

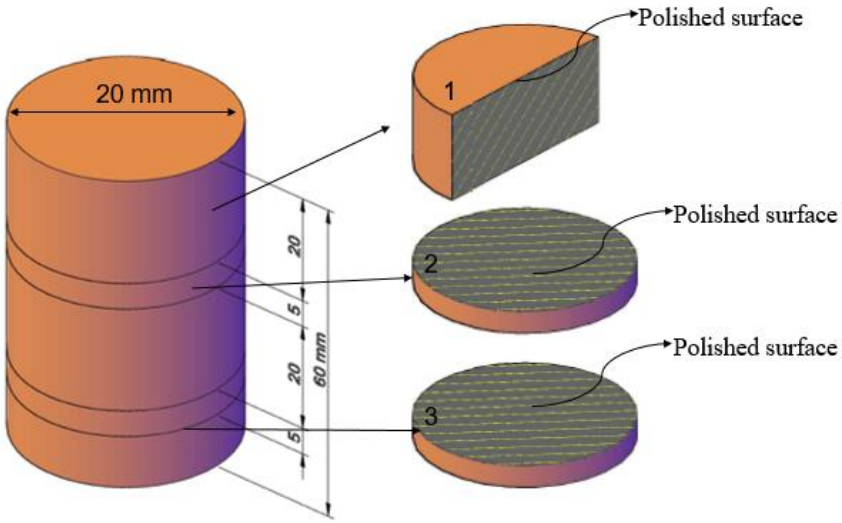

Figure 4.30: Sizes of both entire and sectioned samples for microscopy observations, with indication of section planes.

Figure 4.31-a represents optical image taken from different parts of the top, middle and near-bottom region. It wasn't necessary to etch the sample, because these images have been employed to evaluate porosity in different parts of the bar to be examined. Going from the topmost region of the sample towards the bottom region, the number of smaller pores decreases and that of bigger pores increases. Besides, just gas pores are observed in the topmost region, while some pores arisen from lack of adherence between un-melted zones can be seen in the middle and near-bottom region. Figure 4.31-b, instead, reports on chart the results of porosities of top, middle and near-bottom regions. The topmost region exhibits the maximum porosity (0.68%) and the largest standard deviation. Instead, the other two regions (middle and near-bottom) have got similar characteristics (0.27% of porosity).

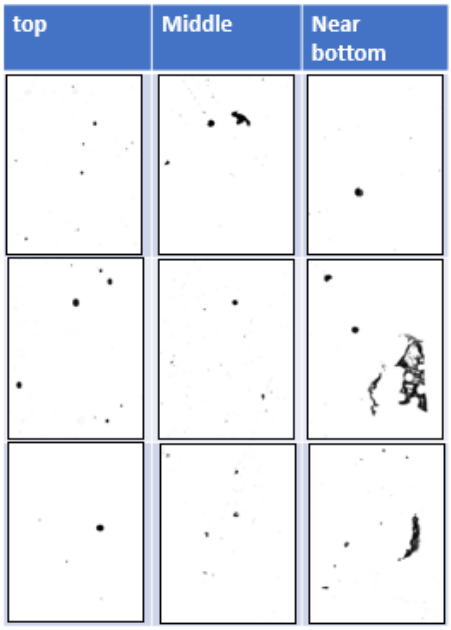

(a)

	Average porosity ± standard deviation (%)
Near Bottom	0.68 ± 0.42
Middle	0.27 ± 0.17
Top	0.27 ± 0.18
Overall	0.41 ± 0.24

(b)

Figure 4.31: (a) Optical microscopy images of top, middle and near-bottom parts of the Ti-6Al-4V EBM produced bars for porosity evaluation. (b) Results of the mean porosities obtained in the three regions.

In consequence of different cooling rate the bcc β phase converts partially to the various α morphologies: α' or α'' martensitic structure with packet or lath morphology according to the diffusionless transformations, α_m (massive) or α' arising from competitive diffusionless and

diffusional transformations, coexistence of allotriomorphic α phase that originates at the previous β grain boundaries with either colony α and/or Widmanstätten α structure at gradually increasing cooling rate, anyway involving diffusion-controlled transformations in both situations.

Considering that EBM is characterized by low cooling rates as the building envelope is normally kept at 650-700ºC, the microstructure obtained in Ti-6Al-4V derives from diffusion-controlled transformations. Thus, in figure 4.32 colony or basketweave Widmanstätten α embedded in prior β grains is observed. α'cannot be reveled in the same microscope images because during the pre-heating and melting occurring after the selective melting of each layer this martensitic structure transforms into α. Just α and β phase sizes at the top position differ with respect to those at middle and near bottom heights: the topmost layers structures presents finer grains because they aren't subjected anymore to further heating cycle that lead to grain growth.

Irrespective of the position, a colony or Widmanstätten basketweave microstructure are clearly observed (figure 4.32). The whitest area corresponds to α phase lamellae, while dark phase corresponds to the rest of primary β grains.

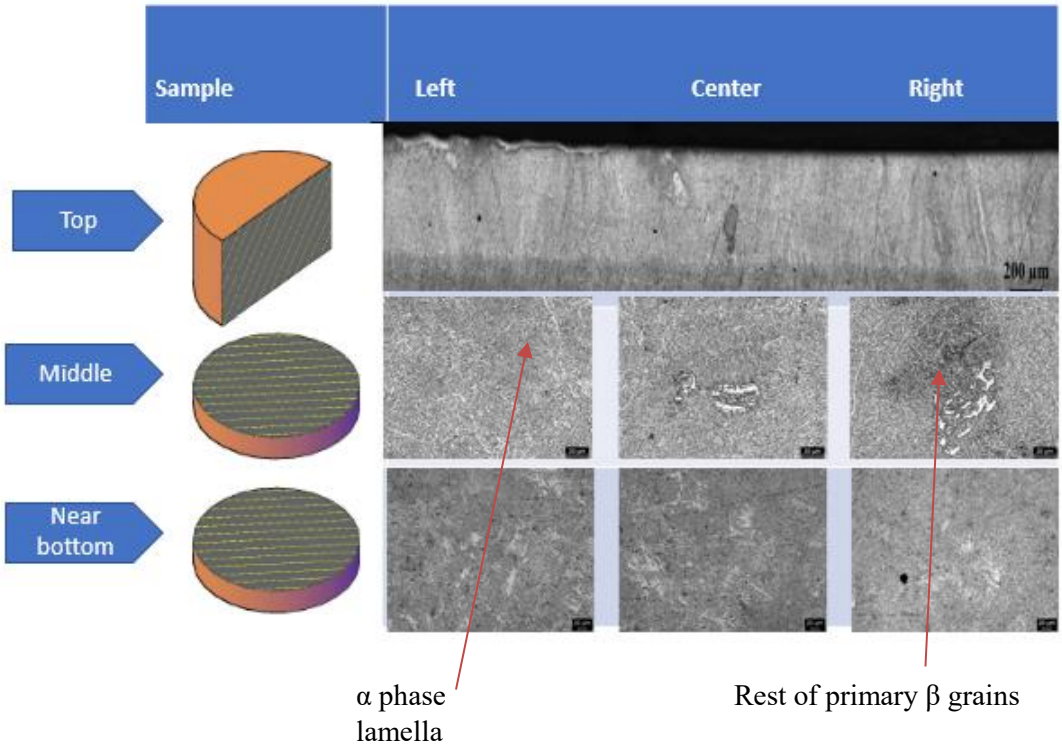

Figure 4.32: Optical microscopy images were taken at three different heights of a Ti-6Al-4V EBM produced bar.

The micrographs reported in figure 4.33 show all images taken from longitudinal sections at different heights of the Ti-6Al-4V bar. The α and β microstructure at the topmost layers is finer than the microstructure observed at the other layers. Also, a finer microstructure is

found at left and right parts, oppositely to the central parts. So, the microstructure observed in this figure reveals the same behaviour of what is seen in figure 4.32.

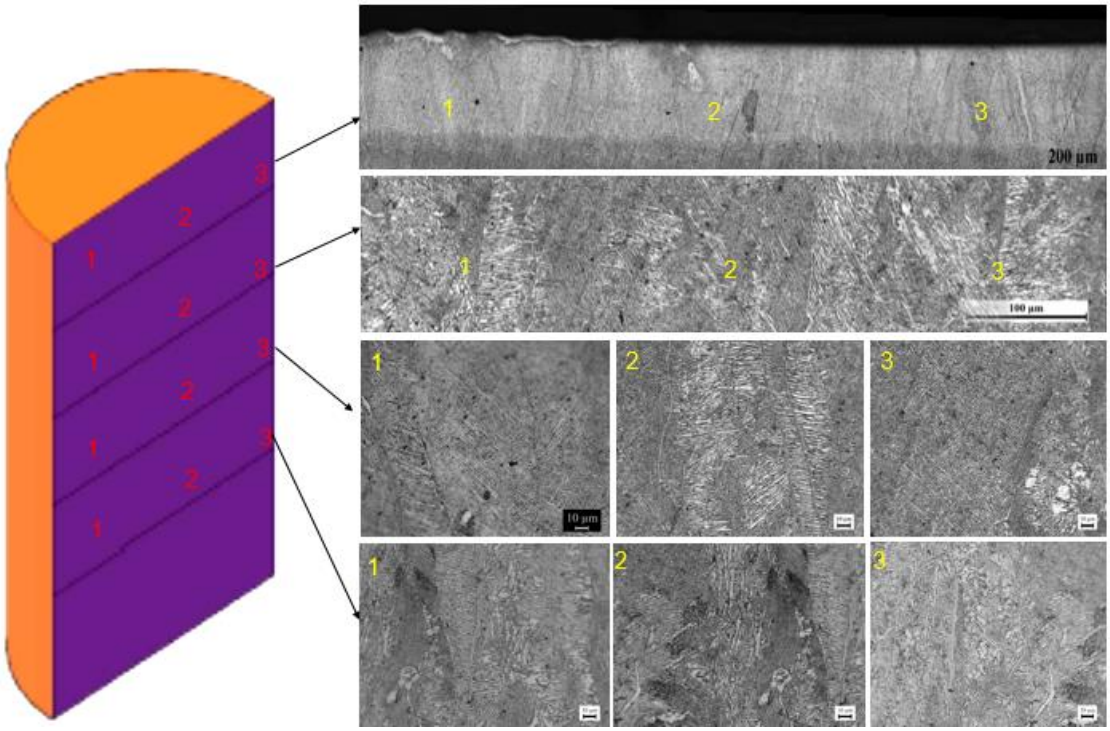

Figure 4.33: Optical microscopy images were taken at four different heights of the top region of a Ti-6Al-4V EBM produced bar.

Figure 4.34 reports optical microscopy images of left, central and right parts related to three different positions of the middle region of the sample. The microstructure exhibits a α laths thickness in at the central parts higher than that revealed at the left and right sides, probably because of the influence of the sample border which cools down quicker than the center.

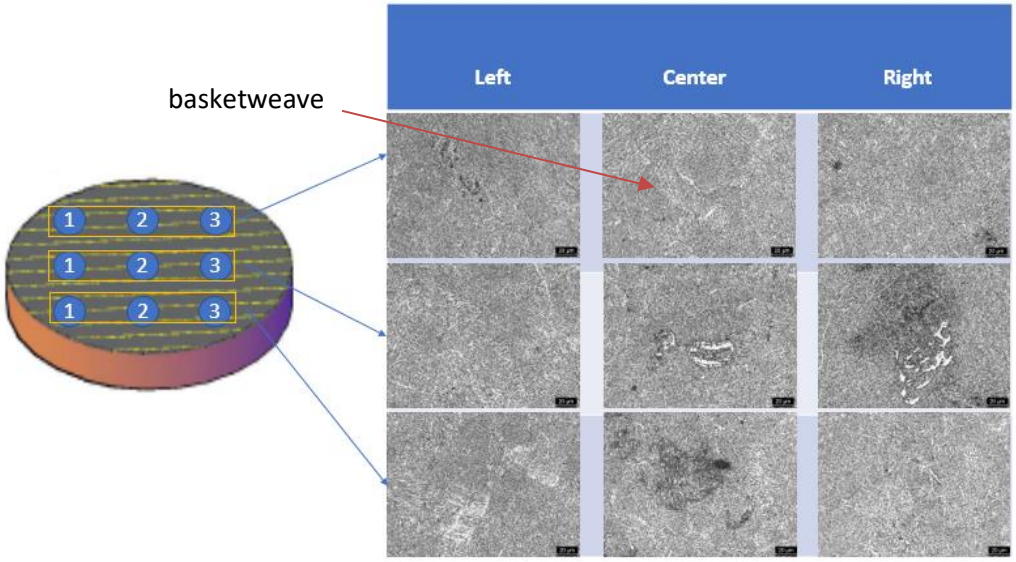

Figure 4.34: Optical microscopy images were taken at three different positions of left, center and right parts of the middle region of a Ti-6Al-4V EBM produced bar.

Figure 4.35 reports some optical microscopy images of left, central and right parts related to three different positions of the near-bottom part of the sample. The microstructure observed in central parts is coarser than those observed at the left and right sides, because at the center the cooling rate is lower than boundary parts. Besides, the density of gas pores increased with respect to top and middle sections.

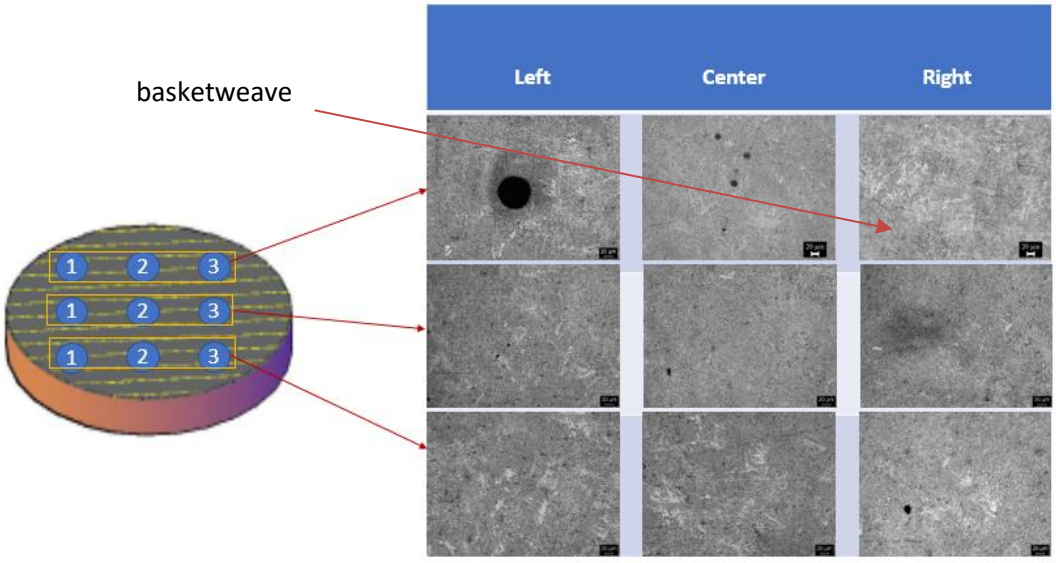

Figure 4.35: Optical microscopy images taken at three different positions of left, center and right parts of the near-bottom region of a Ti-6Al-4V EBM produced bar.

Figure 4.36-a reports the results of a line compositional analysis performed across some elongated features within the α + β microstructure. These ones turned out to be rich in aluminium; so, they may represent two α phase lamellae. Instead, figure 4.36-b reports the results of a line compositional analysis carried out across one of the irregular zones. Its chemical composition doesn't change with respect to the general composition of the alloy (i.e. 6 wt% aluminium and 4 wt% vanadium). This may confirm the fact that those particles belong to non-melted zones.

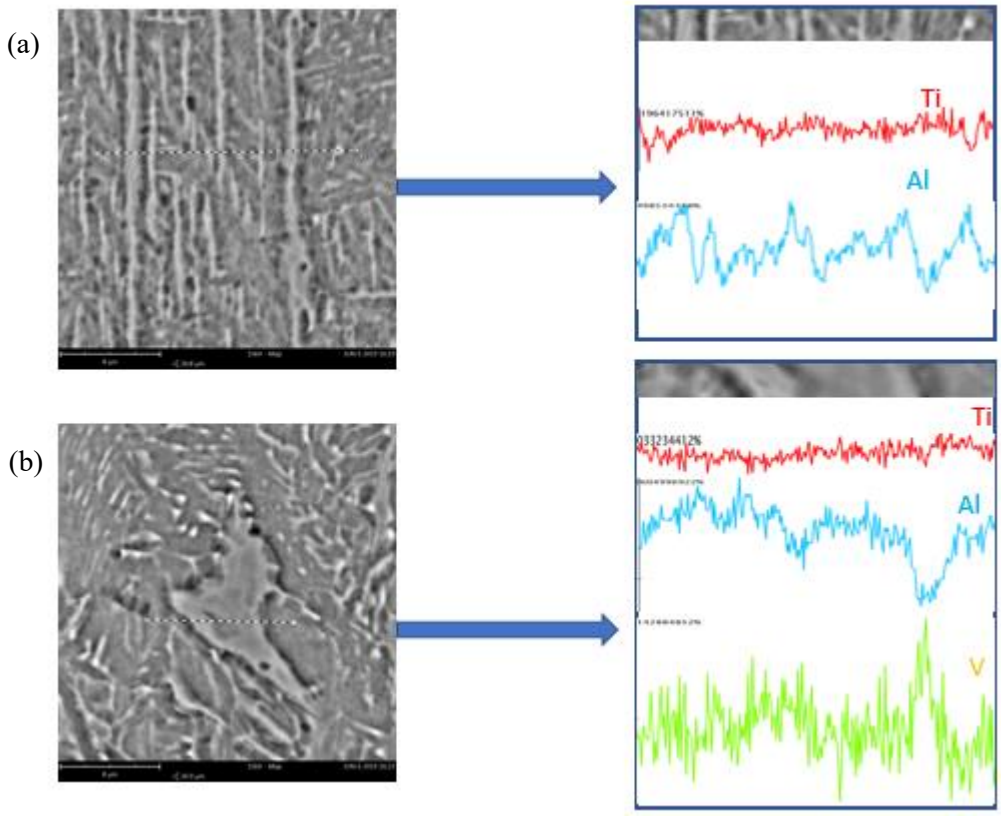

Figure 4.36: (a) SEM-EDS line compositional analysis performed across some elongated features within the α + β microstructure. (b) SEM-EDS line compositional analysis performed across one of the irregular zones.

Figure 4.37 reports the results of chemical composition analyses performed on three different points. At the first point a slight increase in vanadium content (4.25 wt%) and a slight decrease in aluminium concentration (5.87 wt%) is verified; thus, it belongs to a β phase zone. Instead, the second point is particularly rich in aluminium (7.21 wt%) and, thus, belongs to an α phase zone. Finally, the third point is particularly rich in vanadium (10.01 wt%); so, it corresponds to a β phase particle.

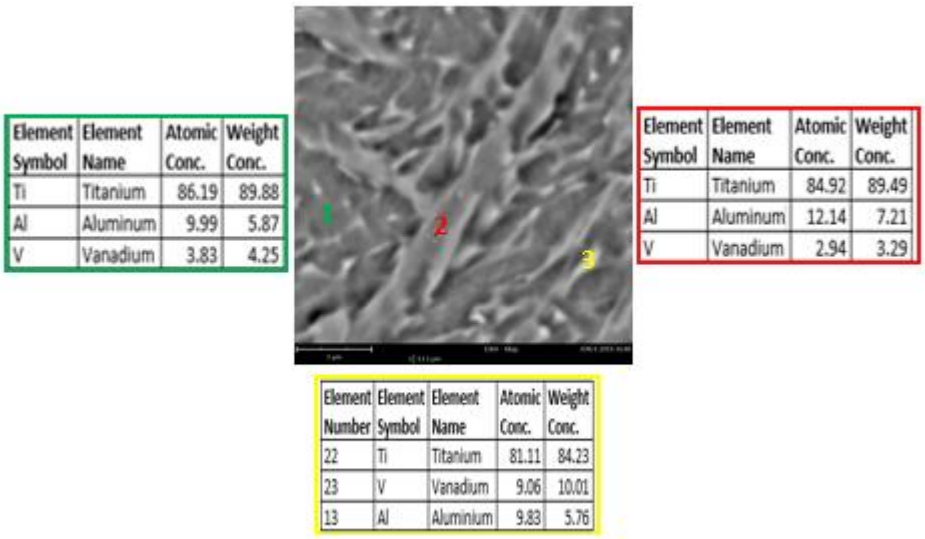

Element Symbol	Element Name	Atomic Conc.	Weight Conc.
Ti	Titanium	86.19	89.88
Al	Aluminum	9.99	5.87
V	Vanadium	3.83	4.25

Element Symbol	Element Name	Atomic Conc.	Weight Conc.
Ti	Titanium	84.92	89.49
Al	Aluminum	12.14	7.21
V	Vanadium	2.94	3.29

Element Number	Element Symbol	Element Name	Atomic Conc.	Weight Conc.
22	Ti	Titanium	81.11	84.23
23	V	Vanadium	9.06	10.01
13	Al	Aluminium	9.83	5.76

Figure 4.37: SEM-EDS chemical composition analyses performed at three different points of a Ti-6Al-4V EBM produced bar.

Figure 4.38 indicates the long and short bars surfaces polished for subsequent observations at the optical microscope and scanning electron microscope. It should be mentioned that long and short bar was taken from a sample produced in the central part of the base plate.

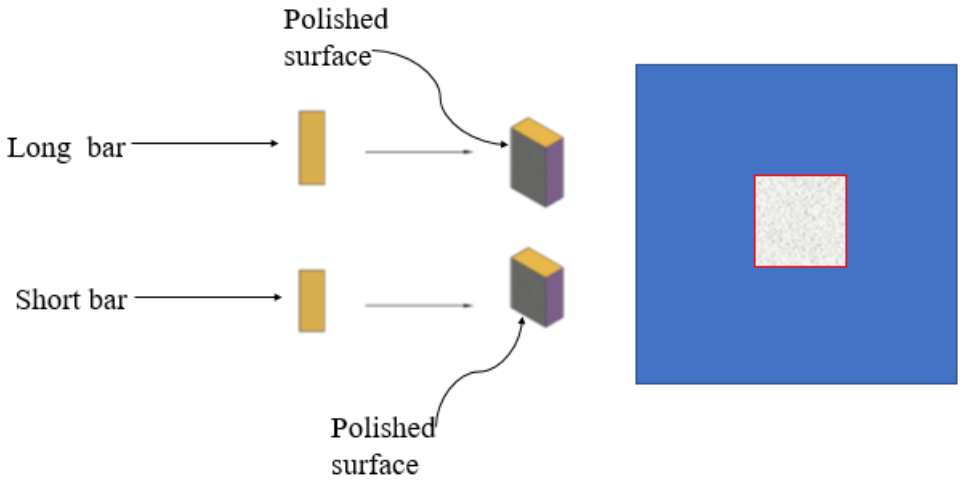

(a) (b)

Figure 4.38: Illustration of section planes on long and short bars (a) and the part of the sample where these bars in reference to the position on the base plate.

Figure 4.39 reports optical microscopy images that have been elaborated by the software in order to evaluate the porosity at three different zones of five different heights of the long bar and at three different zones of three different heights of the short bar. The results are reported also in chart form. The porosity is remarkably reduced from the first to the second column (from 0.79% to 0.15%), indicating a high presence of defects on the topmost region of the long bar. Then, the porosity keeps decreasing until the last column (the bottom region). Instead, for what concerns the short bar, the porosity is gradually reduced going from the topmost region to the bottom one.

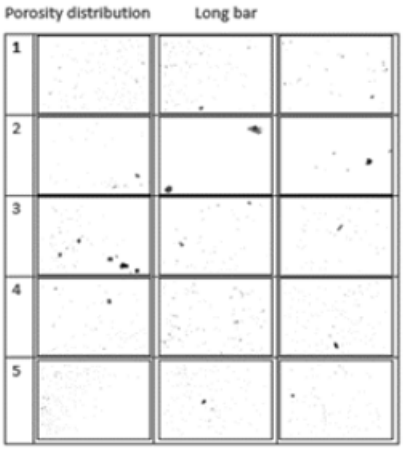

	Average porosity ± standard deviation (%)
Row 1	0.18 ± 0.50
Row 2	0.14 ± 0.17
Row 3	0.10 ± 0.30
Row 4	0.10 ± 0.09
Row 5	0.02 ± 0.03
Overall	0.11 ± 0.06

(a)

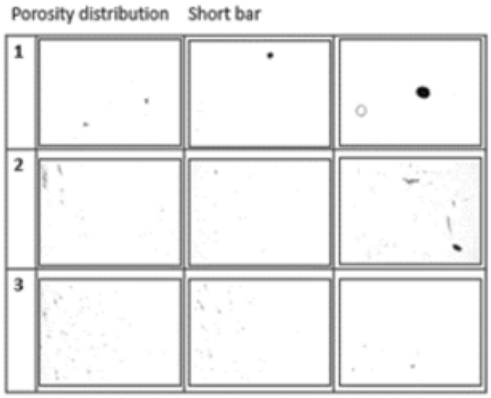

	Average porosity ± standard deviation (%)
Row 1	0.14 ± 0.31
Row 2	0.045 ± 0.10
Row 3	0.004 ± 0.00
Overall	0.06 ± 0.07

(b)

Figure 4.39: (a) Optical microscopy images of three different zones in five different heights of the long bar for the porosity evaluation and relative results on chart. (b) Optical microscopy images of three different zones in three different heights of the short bar for the porosity evaluation and relative results on chart.

Figure 4.40 shows optical microscopy images taken from four zones at three different heights of the short bar. It is possible to observe a colony or Widmanstätten basketweave structure. Besides, grains observed in each zone are columnar along the build direction. The topmost and the bottom region seem to exhibit finer lath microstructure than the middle one. The same occurs at side parts of all the three levels, i.e. the left and right side exhibit a finer microstructure than it is observed at central parts.

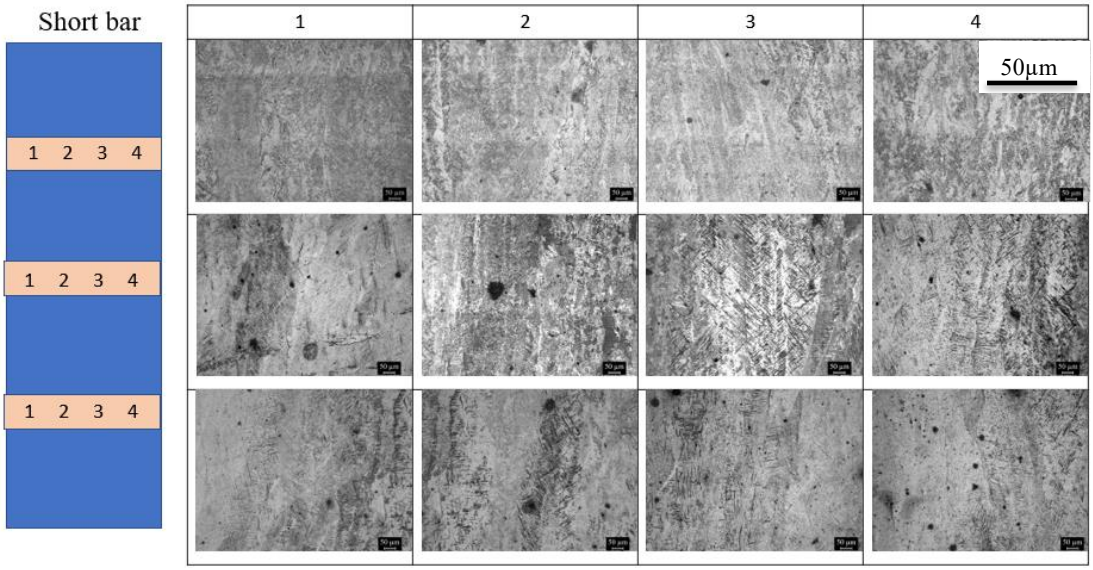

Figure 4.40: Optical microscopy images were taken at three different heights of the short bar.

Figure 4.41 reports SEM images (at 2000x magnification) of the left, middle and right sides of the short bar at three different heights. Also, SEM images reveal the colony and the Widmanstätten structure with columnar grains. The projecting elements visible in these SEM images refer to α phase that is interwoven with "hollow" regions, corresponding to β phase

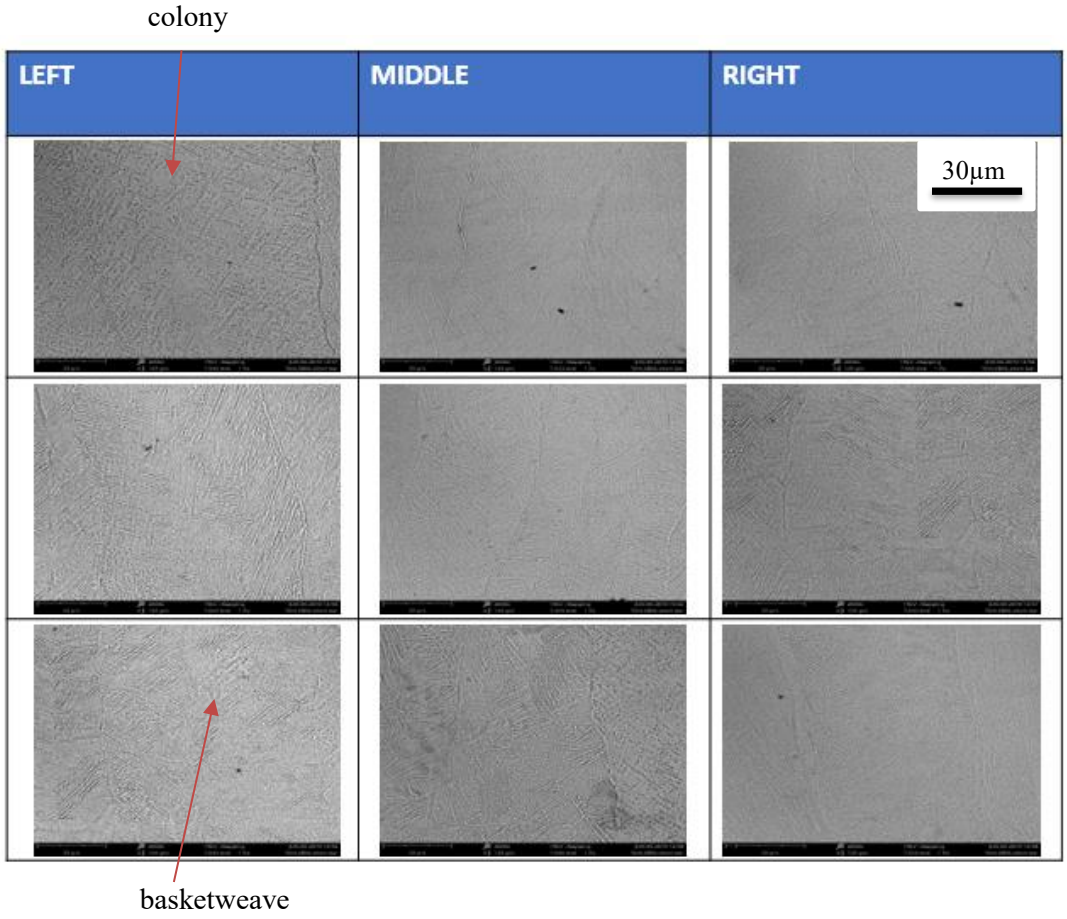

Figure 4.41: SEM images were taken at three different positions of left, centre and right parts of the short bar (2000x magnification).

Figure 4.42 reports SEM images (at 3000x magnification) of the left, middle and right sides of the short bar at three different heights. As it is observed in images both at 2000 and 3000x magnification and from the optical microscope, the topmost and bottom regions are characterized by finer microstructure than middle region one.

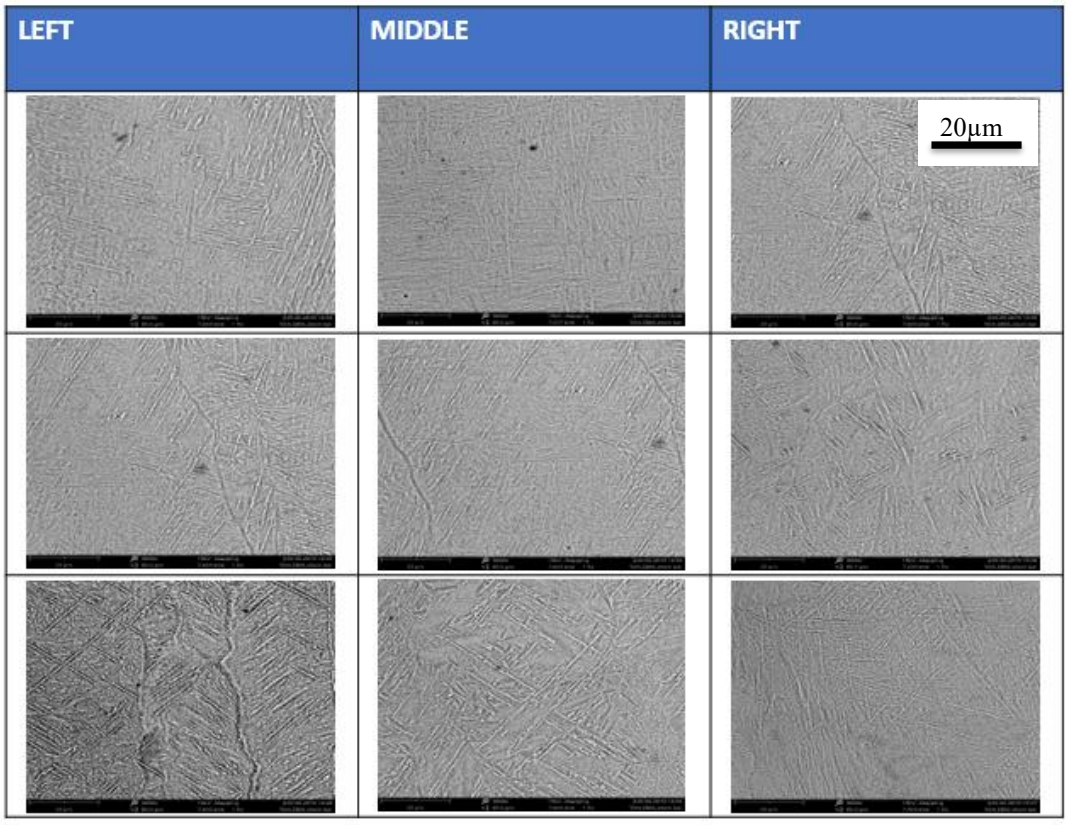

Figure 4.42: SEM images were taken at three different positions of left, centre and right parts of the short bar (2000x magnification).

Figure 4.43 reports optical microscopy images of the long bar at four different positions and five different heights. The microstructure seems to become finer when moving from the topmost layer to the bottom one.

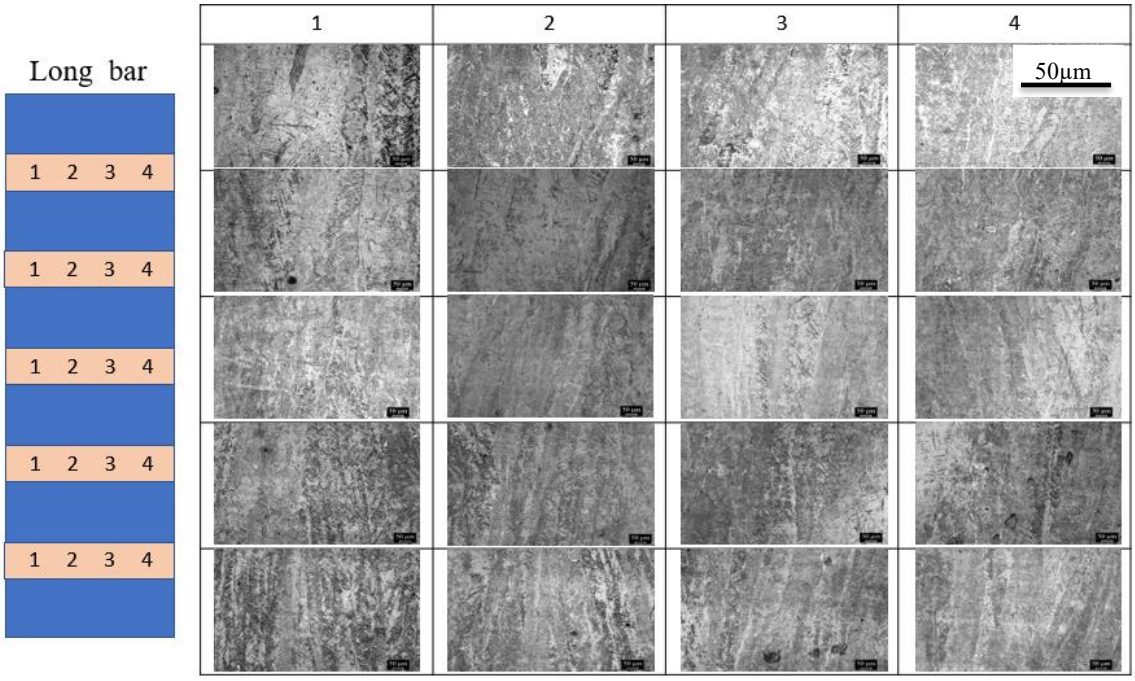

Figure 4.43: Optical microscopy images were taken at five different heights of the long bar.

Figure 4.44 reports SEM images (at 3000x magnification) taken from left, middle and right sides at three different heights of the long bar. All regions are characterized by a Widmanstätten basketweave microstructure, where α phase "laths" are surrounded by punctiform β phase elements. Some irregularly shaped features can be observed in the topmost region of the bar.

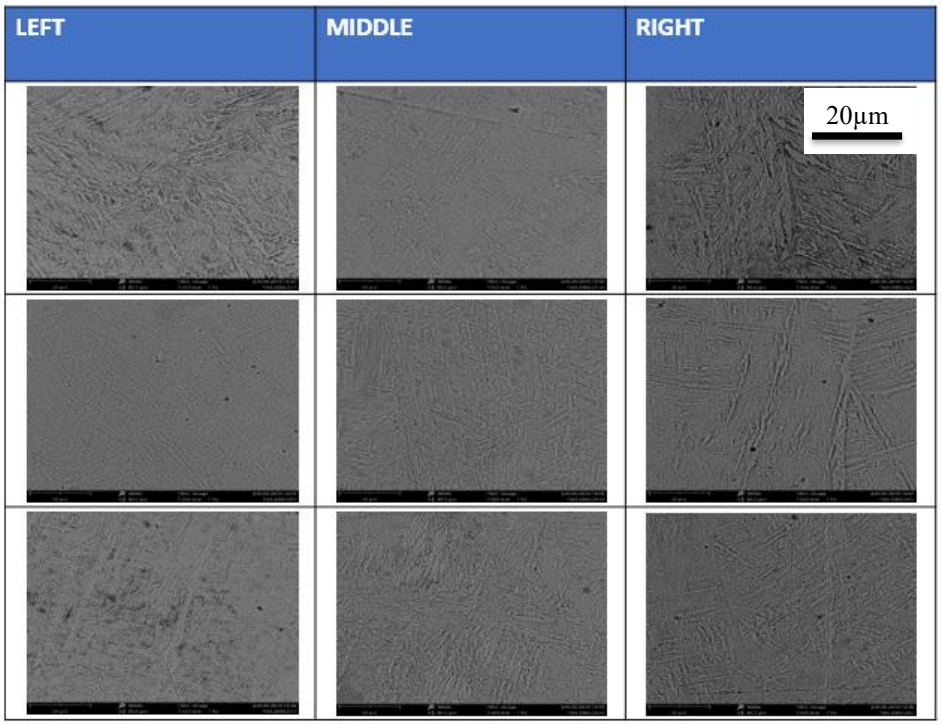

Figure 4.44: SEM images were taken at three different positions of left, centre and right parts of the long bar (3000x magnification).

Figure 4.45 reports SEM images (at 5000x magnification) taken from left, middle and right sides at three different heights of the long bar. As it is observed in images at 3000x magnification, the microstructure is essentially characterized by a set of α phase laths interwoven with β phase elements. The microstructure at left and right sides seems to be coarser than central regions.

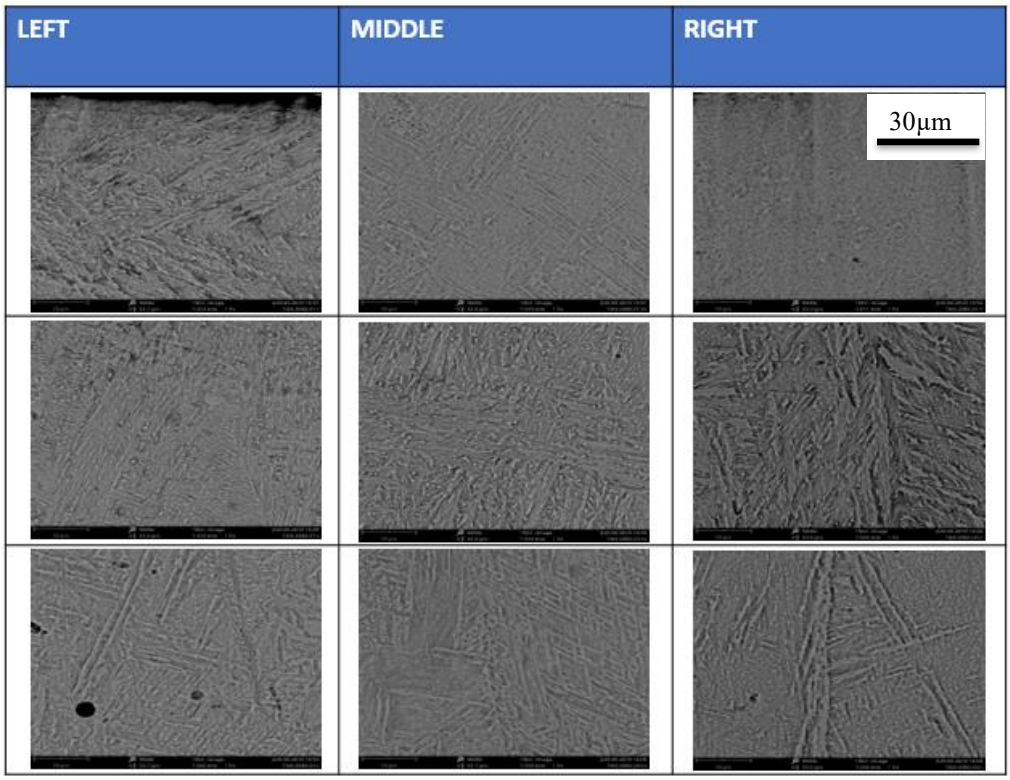

Figure 4.45: SEM images were taken at three different positions of left, centre and right parts of the long bar.

In consequence of different cooling rate the bcc β phase converts partially to the various α morphologies: α' or α'' martensitic structure with packet or lath morphology according to the diffusionless transformations, α_m (massive) or α' arising from competitive diffusionless and diffusional transformations, coexistence of allotriomorphic α phase that originates at the previous β grain boundaries with either colony α and/or Widmanstätten α structure at gradually increasing cooling rate, anyway involving diffusion-controlled transformations in both situations.

Considering that EBM is characterized by low cooling rates as the chamber is normally kept at 650-700ºC, the microstructure obtained in Ti-6Al-4V derives from diffusion-controlled transformations. Thus, in figure 4.32 colony or basketweave Widmanstätten α embedded in prior β grains is observed. α'cannot be reveled in the same microscope images because during the pre-heating and melting occurring after the selective melting of each layer this martensitic structure is decomposed into α + β. Just α and β phase sizes at the top position differ with respect to those at middle and near bottom heights: the topmost layers structures presents finer grains because they aren't subjected anymore to further heating cycle that lead to grain growth. Thus, the microstructure after EBM is very different from that revealed after SLM (Selective Laser Melting), because in this latter case the fast cooling rates determined the formation of α' martensite, obtained with diffusionless transformations starting from previous β grains.

5. Conclusions

In this work, which aimed at the monitoring of Ti-6Al-4V powders taken from various EBM production cycles, four different kinds of powders were analysed

- Powder from hoppers,
- Top sintered powders, namely coming from above of the start plate,
- Bottom sintered powders, namely coming from the bottom of the start plate,
- Recycled Powders after PRS.

This powder monitoring was carried after three different EBM job; starting from the virgin powder, after the first, second and n-cycles of EBM processes. Besides, the microstructure evolution of Ti-6Al-4V EBM-manufactured bars in both building direction and XY direction was observed at different positions and heights within the samples.

According to the finding of this thesis, the main conclusions can be drawn as follow:

- After the first EBM job, the flowability of the powders increased with respect to the virgin powder, mainly owing to the reduction of satellite content, and then decreased starting from the second cycle of EBM production, as the powders became less rounded;
- Increasing the number of EBM jobs, the average particle sizes varied from 62 μm in the case of virgin powders to 70 μm in the case of recycled powders after the n^{th} EBM processing cycle. In fact, coarse particles tend to increase and the volume of fine particles decreases mainly due to both the sintering phenomena that occur in the preheating stage during the EBM process and in the recovery stage;
- The internal porosity analysis of the Ti-6Al-4V particles subjected to the EBM process production showed that porosity of powder during this process didn't change and such pores are obtained from the production of Ti-6Al-4V powders by gas atomization process;
- It is also found that, after the first cycle of EBM process, a thick and non-uniform oxide layer formed and then by increasing the EBM jobs it became gradually thicker and more uniform that covers the entire surface of the particles;
- The microstructure of powders were characterized mostly by a colony or Widmanstätten basket-weave microstructure. The starting microstructure of powder were characterised by α' martensite which was formed during their gas atomization process that is a rapid solidification process. Whereas, even after the first EBM cycle, the microstructure of powders started to transform to the more stable α+β microstructure and thereafter by increasing the number of EBM jobs, the α phase became gradually thicker;
- The peaks revealed by XRD all relate to the α phase and the average crystal sizes of that phase increased with sintering process, but slightly decreased after the PRS stage, not lower than the starting value in the fresh powder. The β phase wasn't detected by the instrument although its presence is proved by SEM-EDS analyses;

- Iron contamination was revealed on some particles, probably due to falling of some metallizations into the building envelope during the build process;
- Two kinds of pores are found in EBM-manufactured bars: gas induced porosity and process induced porosity. The last one is visible as a lack of fusion in some points. The average porosity was about 0.29%, anyway a very low value;
- The porosity evaluation of bulk samples produced at different positions on the start plate showed that the porosity content of these samples are equal and independent from the position of sample.
- SEM-EDS analysis showed that the diffusion depth of alloying elements from the start plate which is a stainless steel plate inside the EBM-produced bars was less than 200 μm. It means that the main alloying elements that are Fe, Cr, Ni were diffused into the Ti-6Al-4V samples and the depth of diffusion is less than 200 μm.
- The materials in bulk form were characterized mostly by a colony or Widmanstätten basket-weave microstructure and, by SEM technique, is possible to distinguish the α phase, rich in aluminium, from the β phase, rich in vanadium. β grains near the start plate nucleate and grow in a near-equiaxed manner. In the upper layers, instead, the grains grow in columnar way, following the thermal gradient developed along the longitudinal direction of the samples. α allotriomorphic grains nucleate preferentially at the grain boundaries of the previously formed β phase and, subsequently, the α phase nucleates and grows also within β grains either with a colony or Widmanstätten basket-weave microstructure, according to the cooling rates.
- It is also found that since the EBM process is characterized by low cooling rates as the building envelope is normally kept at 650-700°C, the microstructure obtained in Ti-6Al-4V derives from diffusion-controlled transformations. Consequently, α' couldn't be revealed because during the pre-heating and melting occurring after the selective melting of each layer this martensitic structure is transformed into α + β.
- In the bulk samples, the positions near to the external side are generally characterized by lower widths of α and β grains than the inner positions as locally the cooling rates increased;

6. References

[1] C. Leyens and M. Peters, Titanium and Titanium Alloys: Fundamentals and Applications, Weinheim: Wiley-VCH, 2003.

[2] A. A. Antonysamy and P. Prangnell, *"Microstructure, Texture and Mechanical Property Evolution during Additive Manufacturing of Ti6Al4V Alloy for Aerospace Applications.",* Manchester: The University of Manchester, 2012.

[3] M. T. Whittaker, "Titanium Alloys," *Metals,* vol. 5, no. 3, pp. 1437-1439, 2015.

[4] C. Veiga, J. P. Devim and A. J. R. Loureiro, ""PROPERTIES AND APPLICATIONS OF TITANIUM ALLOYS: A BRIEF REVIEW."," *Reviews On Advanced Materials Science,* vol. 32, no. 2, pp. 133-148, 2012.

[5] "Arcam EBM system," 2014. [Online]. Available: http://www.arcam.com/wp-content/uploads/Arcam-Ti6Al4V-Titanium-Alloy.pdf.

[6] B. G. Yuan, C. F. Li, H. P. Yu and D. L. Sun, "Influence of Hydrogen Content on Tensile and Compressive Properties of Ti–6Al–4V Alloy at Room Temperature," *Materials Science & Engineering A,* vol. 527, no. 16-17, pp. 4185-4190, 2010.

[7] S. D. Henry, G. M. Davidson, S. R. Lampman, F. Reidenbach, R. L. Boring and W. W. Scott Jr., "Ti-6Al-4V," in *Fatigue Data Book - Light Structural Alloys*, ASM International, 1995.

[8] R. Pederson, *Microstructure and phase transformation of Ti-6Al-4V,* Luleå tekniska universitet, 2002.

[9] D. A. Porter, K. E. Easterling and M. Y. Sherif, Phase Transformations in Metals and Alloys, 3rd ed., Boca Raton: CRC, 2009.

[10] S. Kou, Welding Metallurgy, A John Wiley & Sons. INC, 2003.

[11] F. Tamburrino, V. Perrotta, R. Aversa and A. Apicella, "Additive technology and design process: an innovative tool to drive and assist product development," *XIII international forum Le Vie dei Mercanti,* pp. 1742-1747, 2015.

[12] S. Negi, S. Dhiman and R. K. Sharma, "Basics, applications and future of additive manufacturing technologies: A review," *Journal of Manufacturing Technology Research,* vol. 5, no. 1/2, p. 75, 2013.

[13] W. Frazier, “Metal Additive Manufacturing: A Review,” *Journal of Materials Engineering and Performance,* vol. 23, no. 6, pp. 1917-1928, 2014.

[14] A. Mohammadhosseini, *Properties and Performance of Titanium alloy Processed by Electron Beam Melting Additive Manufacturing,* Swinburne University of Technology, 2014.

[15] C. Körner, “Additive Manufacturing of Metallic Components by Selective Electron Beam Melting - a Review,” *International Materials Reviews,* vol. 61, no. 5, pp. 361-377, 2016.

[16] A. Moarrefzadeh, “Finite-Element simulation of electron beam machining (EBM) Process,” *International Journal of Multidisciplinary Sciences And Engineering,* vol. 2, 2011.

[17] H. Gong, K. Rafi, T. Starr and B. Stucker, “The Effects of Processing Parameters on Defect Regularity in Ti-6Al-4V Parts Fabricated By Selective Laser Melting and Electron Beam Melting,” in *24th Annual International Solid Freeform Fabrication Symposium—An Additive Manufacturing Conference*, Austin, TX, Aug. 2013.

[18] L. Morgan, U. Lindhe and O. Harrysson, “Rapid Manufacturing with Electron Beam Melting (EBM) – A manufacturing revolution ?,” *Solid Freeform Fabrication Proceedings,* pp. 433-438, 2003.

[19] Advanced Powders and Coatings Inc. ©, “advancedpowders.com,” 2014. [Online]. Available: advancedpowders.com/wp-content/uploads/Ti-6AI-4V_45-106m_APC.pdf.

[20] Arcam EBM, “www.arcam.com,” [Online]. Available: http://www.arcam.com/wp-content/uploads/arcamebm-corp-brochure-fnlv3.pdf.

[21] V. Petrovic and R. Niñerola, “Powder Recyclability in Electron Beam Melting for Aeronautical Use,” *Aircraft Engineering and Aerospace Technology: An International Journal,* vol. 87, no. 2, pp. 147-155, 2015.

[22] Retsch, “www.retsch.com,” [Online]. Available: https://www.retsch.com/applications/knowledge-base/sieve-analysis.

[23] Spectrographic Limited, “spectrographic.co.uk,” [Online]. Available: https://spectrographic.co.uk/collections/refurbished/products/presi-mecapol-p320.

[24] A. Handbook, Metallography and Microstructures, vol. 9, ASM International, 2004.

[25] Phenom World, “www.phenom-world.com,” [Online]. Available: https://www.phenom-world.com/downloads/specification_sheets/SPEC_SHEET_PHENOM_XL_2015_LR_1.pdf.

[26] LAB expert, “www.labexpert.bg/gb,” [Online]. Available: https://www.labexpert.bg/gb/13322/index/categoryId/1881.

[27] H. K. D. H. Bhadeshia, “Titanium & its Alloys,” *Metals & Alloys (year 3),* vol. 42, 2011.

[28] nanoScience Instruments, “www.nanoscience.com,” 2018. [Online]. Available: https://www.nanoscience.com/techniques/scanning-electron-microscopy/.

Acknowledgements

At the conclusion of the work carried out I want to first thank to DISAT (Department of Applied Science and Technology) for allowing me access to the laboratories where the experiments and measurements were conducted.

I thank the relator, Professor Sara Biamino, because she gave me the chance to have direct experience on one of the most interesting additive manufacturing technique, in order to enlarge my previous Bachelor's degree knowledge on metallurgy.

I thank the co-relator, Dr. Abdollah Saboori, for being a fundamental guide both during the activities carried out in the laboratories and for the suggestions given to me during the thesis preparation.

I thank the company Arcam because it made available the Ti-6Al-4V powders that have been one of the most studied objects during this work.

I want to thank and dedicate this work to the most loved ones: to my family and my best friends that I've met during the studying years in Turin.